Probing the Environmental Response of Charged Aqueous Surfaces

by

Canyu Cai
B.Sc., Hong Kong Baptist University, 2017

A Dissertation Submitted in Partial Fulfillment of the
Requirements for the Degree of

DOCTOR OF PHILOSOPHY

in the Department of Chemistry

University of Victoria

Probing the Environmental Response of Charged Aqueous Surfaces

by

Canyu Cai
B.Sc., Hong Kong Baptist University, 2017

Supervisory committee

Dr. Dennis K. Hore, Supervisor
(Department of Chemistry)

Dr. Scott McIndoe, Departmental Member
(Department of Chemistry)

Dr. Rishi Gupta, Outside Member
(Department of Civil Engineering)

ABSTRACT

The molecular structure and charge on solid surfaces in aqueous environments is of fundamental importance to various scientific research and applications, yet remain not sufficiently understood. The research herein uses sum frequency generation spectroscopy to reveal the molecular structure of the mineral and polymer surfaces, and also probes the water molecules near the charged aqueous interfaces to get information about the surface charge. The application of visible-infrared sum-frequency generation spectroscopy to polymer thin-films requires a careful interpretation of the results, as the electric field magnitude and phase at each interface must be determined in a manner that takes thin film interference effects into account. A straightforward method that has a concise analytic solution in the case of a single thin film that exhibits interference effects was proposed. This method enabled selective probing of transparent thin-films using sum frequency generation spectroscopy, hence eliminated the ambiguity of the contribution of signal from two interfaces. The method was then extended to multiple polarization schemes, enabling easier and more comprehensive study of the molecular orientation on thin-films. Nonlinear vibrational spectroscopy has also been used to study the temperature-dependent surface structure of polydimethylsiloxane when exposed to water and a perfluorinated hydrophobic liquid. Quantitative analysis of the methyl plane orientation was performed using a combination of vibrational peak ratios and peak amplitudes that enable proposed structures to be identified. For both environments, the tilt and twist of the methyl plane was found to increase with temperature in a reversible manner. This has been attributed to be a consequence of the backbone reorganization due to temperature-dependent density changes.

At charged aqueous interfaces, the structure of water adjacent to solid interface is sensitive to the surface potential. As a result, close inspection of signals originating from these water molecules can be used to reveal the surface charge density. Nonlinear vibrational spectroscopy was used to monitor the water O–H stretching band over a temperature range of 10–75°C to account for the increase in surface potential from deprotonation. It has been demonstrated that the behavior at the silica surface is a balance between increasing surface charge, and a decreasing contribution of water molecules aligned by the surface charge. Together with a model that accounts for two different types of silanol sites, the change in enthalpy and entropy for deprotonation at each site were reported. The surface charge density of untreated polydimethylsiloxane surface in water with various ionic strengths was also determined. It was found that the surface charge could be explained with an ion adsorption model. A relationship between the surface potential and measured nonlinear optics response that is valid at high potentials and low ionic strength was proposed. Finally, a universal method was demonstrated to derive the surface potential with nonlinear optics by modulating the coherence length.

Contents

List of Tables

List of Figures

List of Abbreviations or Symbols and Definitions

Abbreviation or Symbol	**Definition**
AOI	angle of incidence
EDL	electrical double layer
IR	infrared
SFG	sum frequency generation
SHG	second harmonic generation
MBI	multiple beam interference
NR	nonresonant
ODF	orientation distribution function
OTS	n-octadecyltrichlorosilane
PDMS	polydimethylsiloxane
$\chi^{(2)}$	second order nonlinear susceptibility
$\chi^{(3)}$	third order nonlinear susceptibility
R	ratio of the magnitude of $\chi^{(2)}$ over $\chi^{(3)}$, $R = \lvert\chi^{(2)}\rvert/\lvert\chi^{(3)}\rvert$
α	linear polarizability
$\alpha^{(2)}$	hyperpolarizability
θ	Euler angle, for tilt or angle of incidence
ϕ	Euler angle, for azimuth
ψ	Euler angle, for twist
Φ	electric potential
Φ_0	surface potential

ACKNOWLEDGEMENTS

Throughout the journey, I have received a great deal of support and assistance from many people.

I would first like to express my deepest appreciation to my supervisor, Dennis Hore, whose enthusiasm for science deeply inspired me. Dennis has offered me guidance not only in research but so much else as well. I would not have started my Ph.D. without him.

I have to thank Md. Shafiul Azam for all the hard work he has done and all the contributions to the research. Working with Azam was a wonderful experience.

I would like to acknowledge my colleagues in the lab, Tasha Jarisz, Sean Yang, Margo Ramsay, Yalan Yu, Victor Sun, Celebi Wan. Thank you all for creating the best work environment and offering all the insightful comments and suggestions.

I am deeply grateful to ASAsoft (Canada) Inc. and Mr. Rajkumar Padmawar for the support and opportunities of collaboration.

Special thanks to my wife Tong Li, for always standing by my side and tolerating me.

Finally I would like to dedicate this thesis to my parents, Haobin Cai and Yalan Wang. Your endless patience and unconditional love have made me here today.

Chapter 1

Introduction

1.1 Motivation

Silicone is a family of polymer materials that are mainly made up of siloxane chains. Silicones are known to have several useful properties such as elasticity, thermal stability, and hydrophobicity. They have a wide range of applications in industrial use, consumer products, and scientific research, especially in the field of chemistry, chemical engineering, biology and medicine.[1–3] Many of the applications rely on the unique surface properties of silicone materials. For example, silicone cookware is easy to clean because of the temperature-resistant hydrophobicity of silicone surfaces; implants made of silicone materials are safe to humans because of the bio-compatibility of silicone surfaces; and testing devices such as microfluidic chips use silicone as the base material because the surface properties of silicone like hydrophobicity can be tuned with ease. One of the main motivations of this research is to investigate the surface stability of silicone rubber insulators for high voltage power lines. Compared to traditional ceramic insulators they are lighter and more cost-effective. However, these silicone insulators are prone to degrade: over time the surface would gradually lose their hydrophobicity.[4–6] Such degradation will affect the performance of the insulator and may even lead to flashover (arc flash) which is a fire hazard.[7] Therefore, the surface stability of the silicone rubbers in extreme conditions like high temperature, high concentration salt exposure, and UV irradiation etc. is critical for the application of silicone insulators.[8,9] Some also reported that silicone rubbers, not limited to those used on insulators, are able to "self-heal" and recover the hydrophobicity.[6,10,11] However, the mechanism of these behaviours on a molecular level are yet to be explored. Such knowledge could lead to innovation in the next generation of silicone rubber insulators with a longer life span, higher performance, and less environmental impact. Thus, it is important to study the microscopic or molecular structure behind the surface properties.

Most of the applications of silicone materials involve water environments. It has been reported that PDMS surfaces, without any modifications, inherently possess surface charge.[12] In the field of biomedicinal research and especially microfluidics, the surface charge of PDMS is critical since it affects protein adsorption, cell adhesion, and molecule separation etc.[12–14] Modifying PDMS to alter the surface potential using techniques like UV irradiation, plasma treatment, and chemical and physical deposition have been used in making microfluidic chips. Many attempts have been made to measure the surface charge of PDMS, including protein adhesion,[14,15] electro-osmotic mobility,[12] and direct measurement of current,[16] etc. Yet these methods lack versatility, require specific setup and/or not very accurate. Second order non-linear optics techniques like second harmonic generation spectroscopy and sum frequency generation spectroscopy will only give rise of signal when there exists break of centro-symmetry. Also since water molecules are polar molecules, when a surface is charged, the surrounding water molecules rotate and align according to the strength and polarity of the charge. Therefore, with these techniques, one will be able to deduce the surface charge by probing the alignment of the water molecules. Second order non-linear optics are ideal for studying surface potential at aqueous interfaces, however the interpretation of the experimental result is not straightforward, due to the complexity in disentangling the origin of the signals. In order to interpret the experimental results from charged aqueous interfaces correctly, a model describing the charge distribution, water molecule orientation and origin of the signal is essential.

Silicon is the second most abundant element on the planet, and it makes up about 26% of Earth's crust by weight. Silica is one of the most important silicon compounds. The surface structure of silica is of fundamental importance to many environmental and geophysical processes such as dissolution, rock weathering, erosion, and pollutant transport.[17–19] Moreover, a host of applications including silica-based catalysts,[20,21] chemical sensors,[22,23] DNA microarrays,[24,25] drug delivery platforms,[26] and microfluidics[27] depend extensively on the molecular interactions of guest molecules with silica at a pH above its point of zero charge. The silica surface charge in aqueous environment is an important factor influencing all of the above applications. Therefore, understanding the surface charge of the silica–aqueous interface is of great importance. Moreover, environmental factors like temperature, ionic strength, and ions presented in the solution will also affect the surface charge of the silica–aqueous interfaces. To investigate how these factors would affect the surface chemistry and hence the surface charge of the silica–aqueous interfaces, a non-intrusive and *in situ* mesurement of the surface charge would be ideal. Again, non-linear optics will be among the best candidates for the surface charge studies.

1.2 Probing the Molecular Structure of Interfaces

1.2.1 SFG Spectroscopy

Many techniques exist for probing surface and interface properties, such as attenuated total reflection IR (ATR-IR), glancing angle Raman spectroscopy, and second-harmonic generation spectroscopy, etc.[28] Sum frequency generation spectroscopy is the one most commonly used in this thesis. Sum frequency generation (SFG) is the process where two photons at frequencies of ω_1 and ω_2 annihilate and a new photon at a frequency of the sum $\omega_3 = \omega_1 + \omega_2$ is generated.[29,30] In SFG spectroscopy, two laser beams are overlapped spatially and temporally to generate SFG signal. As a second order nonlinear spectroscopy, SFG spectroscopy has some defining characteristics: (1) it is intrinsically interface sensitive and it follows the nonlinear optical selection rule. Which means that signal only arises from material interfaces where break of centrosymmetry exists (when the material is centrosymmetric the second order susceptibility must vanish); (2) the response contains information ib the molecular orientation. These characteristics make SFG spectroscopy a powerful tool for surface study and it has become routine for the study of the interfaces of solids, liquids, and polymers.[28,31]

When a material is exposed to a large electromagnetic field, nonlinear optical phenomena can be observed. The total induced molecular dipoles induced by the electromagnetic field is,

$$\mu = \mu_0 + \alpha^{(1)}\overrightarrow{E}^1 + \alpha^{(2)}\overrightarrow{E}^2 + \alpha^{(3)}\overrightarrow{E}^3 + \ldots + \alpha^{(n)}\overrightarrow{E}^n. \tag{1.1}$$

Here μ_0 is the permanent dipole and $\alpha^{(n)}$ are the molecular polarizabilities, and higher order polarizabilities are usually referred to as hyperpolarizabilities. In nonlinear optics, the total polarization of the material response to the external field is expressed by

$$\overrightarrow{P} = \varepsilon_0(\chi^{(1)}\overrightarrow{E}^1 + \chi^{(2)}\overrightarrow{E}^2 + \chi^{(3)}\overrightarrow{E}^3 + \ldots + \chi^{(n)}\overrightarrow{E}^n), \tag{1.2}$$

where $\chi^{(n)}$ is the nth order susceptibility. So for second order nonlinear optics

$$\overrightarrow{P}^{(2)} = \varepsilon_0\chi^{(2)}\overrightarrow{E}^2. \tag{1.3}$$

There is a visible laser at a fixed frequency and a tuneable infrared (IR) laser in the experimental set up used to collect the data presented in this thesis. The SFG signal is recorded against the wavenumber of the IR laser. The SFG intensity can be expressed as

$$I_{\mathrm{SFG}} \propto |LL L\chi^{(2)}|^2 I_{\mathrm{vis}} I_{\mathrm{IR}}. \tag{1.4}$$

When the IR frequency is in resonance with vibrational mode of the molecules being probed, $\chi^{(2)}$ will be enhanced. The resonant nature of $\chi^{(2)}$ can be written as

$$\chi^{(2)} = \chi^{(2)}_{\mathrm{R}} + \chi^{(2)}_{\mathrm{NR}} = \sum_q \frac{A_q}{\omega_q - \omega_{\mathrm{IR}} - i\Gamma_q} + \chi^{(2)}_{\mathrm{NR}}. \tag{1.5}$$

where $\chi^{(2)}_{\mathrm{NR}}$ is the nonresonant response, q is each individual vibrational modes of a particular functional group contributing to the total, A_q is the amplitude of the vibrational mode, ω_q is the vibrational resonance energy, Γ_q is the width of the mode, and $i = \sqrt{-1}$. The $\chi^{(2)}$ is a function of the ensemble average of the corresponding $\alpha^{(2)}$. It is also a third-rank tensor with 27 tensor elements, since it is related to the induced polarization along the given axes of the polarizations of the two incident lasers. With different combinations of polarization of the three beams different tensor elements are being probed. The $\alpha^{(2)}$ value of the functional groups can be obtained from electronic structure calculation, bond-additive models, or polarized Raman measurements. And the $\chi^{(2)}$ can be extracted from SFG spectra, using Equation 1.4 and 1.5. Using axes transformation and projection, information about the molecular orientation on the interfaces could be extracted.

1.2.2 Thin Film SFG Studies

When light travels from one medium to another, through an interface, part of the energy is reflected, and the remaining part would be either absorbed or transmitted (refracted) into the other media. Now consider a film sandwiched between two semi-infinite bulk media (Figure 1.1). When light goes through the first interface, part of it was refracted. This transmitted light would then encounter the second interface between the film and the second semi-infinite bulk medium, the same would happen again and the light would be split into reflected and transmitted portions. Therefore, eventually, except the portion absorbed by the media, the light would bounce between two interfaces, and eventually reflect or refract to the bulk media. For polarized light sources (as in the case of SFG spectroscopy), the set of beams reflected or transmitted would have constructive or destructive interference effect with each other, and consequently enhancing or diminishing the intensity of the beams. This effect cannot be ignored when the film has a thickness in the same magnitude of or smaller than the wavelength of the probing beams.[32] The interference effect depends on: the thickness of the film; the angle of incidence; and the refractive indices of each medium.

In most SFG studies of polymer interfaces, the polymers take the form of thin films. As discussed above, when the film has a certain thickness (in the magnitude of the wavelength

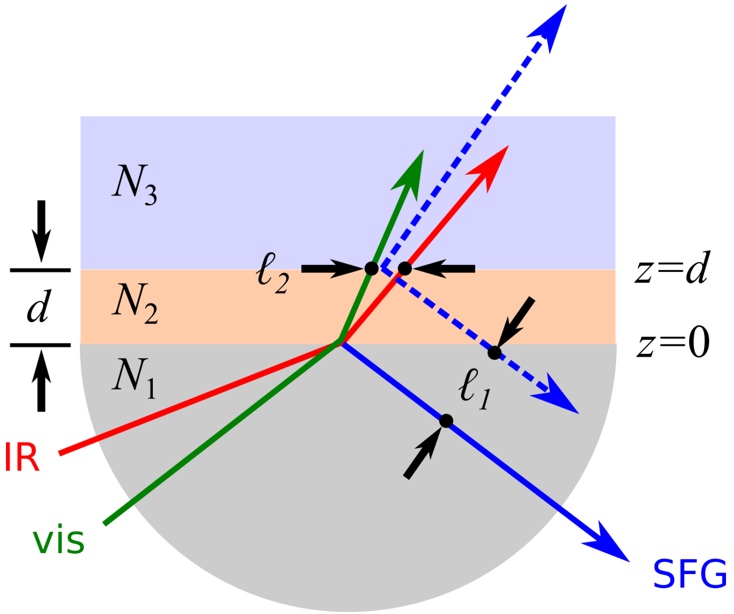

Figure 1.1: A film of refractive index N_2 and thickness d, situated between two semi-infinite media with indices N_1 and N_3. SFG reflected from the top surface is spatially separated from SFG reflected from the bottom surface by a distance ℓ_1. If incoming visible and infrared beams are spatially overlapped at the top surface, the center of the beams are separated by ℓ_2 at the bottom surface. Reprinted with permission from Ref. 33. Copyright 2019 American Chemical Society.

of probe beams), the multiple beam interference effect has to be taken into account. Then, the situation will be that, without further information, it is not possible to rule out *a priori* whether $\chi^{(2)} \neq 0$ at the substrate–film interface, the film–ambient/environmental interface, or both. Before getting into the multiple beam interference problem, it is useful to consider if there are any simple experimental situations where the measured signal can safely be assumed to originate from only one of two surfaces.

1.2.2.1 Thick Films

With reference to Figure 1.1, one phase is the substrate on which the film film is coated. The other can be either air, another polymer, aqueous solution or another liquid. The most straightforward case to consider is one where the incident medium (medium 1) is not absorbing for any of the frequencies of interest. Strictly speaking, medium 1 does not have to be perfectly transparent, but the analysis and the points will be ultimately made here are greatly simplified under this assumption. The first question is whether the film thickness d could be large enough so that beams may be selectively overlapped at one of the two interfaces. This is not possible as, for typical refractive indices and beam angles, if the visible and infrared with diameters of 200 μm each were 100% overlapped at the interface between media 1 and 2, simple trigonometric relationships indicate that 0% overlap ($\ell_2 >$ 200 μm in Figure 1.1) at the interface between media 2 and 3 would occur only for $d >$ 2 mm. Likewise, if the pulses had a duration of 20 ps, the temporal overlap would be lost only for $d >$ 4 mm. In other words, for films with $d <$ 1000 nm, the beams are essentially overlapped perfectly in space and time at both interfaces. Another possibility is to set up a pinhole so that dashed blue line in the reflected SFG in Figure 1.1 is blocked. But for ℓ_1 to be greater than the diameter of the beams, $d >$ 5 mm is required.

One then contemplates how thick the film would have to be so that one of the incident beams is sufficiently attenuated by absorption in passing through before reaching the second interface. It is often discussed that, in the C–H stretching region of the mid-infrared such a situation may be readily realized with spin-coated samples. The most intense band in this region for polydimethylsiloxane (PDMS), the 2910 cm^{-1} methyl symmetric stretch with imaginary part of the refractive index $\kappa = 0.05$ was considered. Even with such a large value of κ, this translates to 50% of the IR intensity still present after a path length of 4 μm. With an IR beam incident at 70°, this still requires $d >$ 1.5 μm. More concerning is that the mode with the next strongest oscillator strength, the methyl antisymmetric stretch at 2960 cm^{-1} has a value of κ that is approximately 10 times smaller, so one would require $d >$ 15 μm to lose 50% of the IR intensity. The ramifications of this quick analysis is not only that sufficient IR intensity is present in the C–H stretching region of organic thin films to simultaneously excite contributions from $\chi^{(2)}$ at both interfaces, but that one may expect severe spectral distortions on account of the varying degrees of IR attenuation.

Another possibility concerns the ratio between the transmitted (upwards pointing dashed blue line in Figure 1.1) and reflected (solid blue line) SFG fields in relation to the contrast between the refractive indices N_1 and N_2. Many polymers are nearly index matched to glass in the visible region ($N_1 \approx N_2$), and are not far off from this condition in the infrared. It will later be demonstrated that such index-matching plays no role. Even though this results in practically no visible and infrared reflection at the medium 1–medium 2 boundary, there can still be a substantial amount of reflected SFG if $\chi^{(2)} \neq 0$ there.

One simple solution remains, and that is to have the beams incident from either side, and then exclude contributions from the second interface by virtue of *all* of the above phenomena. In other words, if films could be prepared with d on the order of millimeters, then there is no doubt since no SFG is possible due to IR absorption, and both spatial and temporal overlap are lacked. However, it is quite challenging to selectively probe the polymer–air interface using any method preparing thick films, since the surface roughness rapidly increases with solution concentration and is inversely proportional to the spinning speed.[34,35]

1.2.2.2 Layers with Molecular Dimensions

Now the case where a monolayer or near monolayer of molecules is deposited onto a substrate will be examined. This is also a single-layer (3-phase) system, except that the 'layer' has dimensions on the order of a few nanometers. The same convention where the incident medium as index N_1, and the environmental side (air or aqueous phase in Figure 1.1) has index N_3 will be maintained. Here the ratio of the fields in the molecular layer with respect to the incident p- and s-polarized fields are

$$L_{xx}^{d/2} = \frac{E_x^{z=d/2}}{E_\mathrm{p}^{z=-\infty}} = (1 - r_p)\cos\theta \tag{1.6a}$$

$$L_{yy}^{d/2} = \frac{E_y^{z=d/2}}{E_\mathrm{s}^{z=-\infty}} = (1 + r_s) \tag{1.6b}$$

$$L_{zz}^{d/2} = \frac{E_z^{z=d/2}}{E_\mathrm{p}^{z=-\infty}} = (1 + r_p)\sin\theta\left(\frac{N_1}{N'}\right)^2. \tag{1.6c}$$

and N' is the refractive index of the molecular layer.[30,36] Here r_p and r_s are the standard Fresnel reflection coefficients[37]

$$r_p = \frac{N_3 \cos\theta_1 - N_1 \cos\theta_3}{N_1 \cos\theta_3 + N_3 \cos\theta_1} \tag{1.7a}$$

$$r_s = \frac{N_1 \cos\theta_1 - N_3 \cos\theta_3}{N_1 \cos\theta_1 + N_3 \cos\theta_3}. \tag{1.7b}$$

with care given to the sign convention used in the definition of r_p. These values of the fields were labeled as those obtained at $z = d/2$ although, for such dimensions, there is no appreciable variation with z within the molecular layer. It is, in general, not straightforward to arrive at a value of N' for several reasons: (1) it is sensitive to the local environment of the molecules, which may be substantially different from what they experience in a bulk phase with index N_2; (2) the interfacial electronic structure is influenced by N_1 and N_3; (3) N' depends on the degree of order within the molecular layer, and so is anisotropic; in the simplest case $N'_x = N'_y \neq N'_z$. This last point results in a circular argument, since one of the goals of polarized SFG spectroscopy is to provide a quantitative description of the molecular orientation—an account of this anisotropy—through measurement of the non-zero values of the $\chi^{(2)}$ tensor and yet the local field correction factor L_z depends the precise details of the molecular arrangement! Fortunately, there are many cases in which approximations for L_{zz}, including an isotropic assumption, do not severely impact the experimental effort. But still, for a polymer experiment, a molecular layer of polymer molecules most likely would behave differently and not be representative of the surface of bulk materials of interest, due to different degrees of cross-linking and etc.

In conclusion, in cases where multiple beam interference effects and the interface ambiguity can be ignored, it would be either hard to measure SFG spectra due to high scattering (thick film), or it would not represent the system of interest (single molecular layer). Therefore it is inevitable to involve the multiple beam interference in these studies.

1.2.2.3 Multiple Beam Interference Model

There have been many methods and formalisms proposed for the calculation of the mean square fields. Some of these have been popularized due to their convenience, especially before computers were widely available. As it is not our intention to provide a comprehensive review or even list the various approaches, only one method will be described, that is often referred to as the exact, or electrodynamic, treatment as it incorporates the thickness and complex refractive index of each material explicitly. This is the technique originally proposed by Abèles and extended by Hansen,[38] and then Axelsen and Citra.[39] This method treats the general case of light incident from a transparent semi-infinite phase (such as air, $N_1 = n_1,\ \kappa_1 = 0$) with angle θ_1 with respect to the surface normal $\hat{z}$ onto a stratified system. Each layer j of thickness d_j has complex refractive index $N_j = n_j + i\kappa_j$, where $i = \sqrt{-1}$. Finally the beam encounters the last semi-infinite phase with $N_N = n_N + i\kappa_N$. The exact solution may be formulated in a matrix form where each of the layers (from $j = 2$ to $j = N-1$) is accounted for by a matrix $\mathbf{M}_j$ that relates the tangential components U of the electric, and V of the magnetic parts of the electromagnetic field at the first surface ($z = z_1 = 0$) to the last surface ($z = z_N$)

$$\begin{bmatrix} U_1 \\ V_1 \end{bmatrix} = \mathbf{M}_2\mathbf{M}_3\mathbf{M}_4 \cdots \mathbf{M}_{N-1} \begin{bmatrix} U_{N-1} \\ V_{N-1} \end{bmatrix}, \tag{1.8}$$

where

$$\mathbf{M}_j = \begin{bmatrix} \cos\beta_j & -\dfrac{i}{p_j}\sin\beta_j \\ -ip_j\sin\beta_j & \cos\beta_j \end{bmatrix}, \tag{1.9}$$

and $p_j^s = N_j \cos\theta_j$ with θ_j the refracted angle in medium j for s-polarized light ($\mathbf{E}$ along $\hat{y}$, perpendicular to the plane of incidence), and $p_j^p = p_j^s/N_j^2$ for p-polarized light (components of $\mathbf{E}$ along $\hat{x}$ and $\hat{z}$, parallel to the plane of incidence. The term accounting for the phase of the fields between the layers is defined as

$$\beta_j = \frac{2\pi d_j p_j}{\lambda}. \tag{1.10}$$

This matrix **M** is powerful as it directly leads to the transmittance and reflectance spectra. Our objective is to arrive at the electric fields, so one could invert **M** to obtain

$$\mathbf{N}_j = \left(\mathbf{M}_j\right)^{-1} = \begin{bmatrix} \cos\beta_j & \dfrac{i}{p_j}\sin\beta_j \\ ip_j\sin\beta_j & \cos\beta_j \end{bmatrix}, \tag{1.11}$$

with

$$\beta_k = \frac{2\pi}{\lambda} p_k (z - z_{k-1}),$$

where z_{k-1} is the thickness of phase $k-1$. These **N** matrices may be used to obtain U, V, and W at any location z in material k according to

$$\begin{bmatrix} U_k(z) \\ V_k(z) \end{bmatrix} = N_k(z) \prod_{j=k}^{2} N_j \begin{bmatrix} U_{N-1} \\ V_{N-1} \end{bmatrix} \tag{1.12a}$$

$$W_k(z) = \frac{N_1 \sin(\theta_1)}{N_k^2} U_k(z). \tag{1.12b}$$

Finally the quantities of interest are obtained via

$$E_x = U_k(z) \tag{1.13a}$$

$$E_y = V_k(z) \tag{1.13b}$$

$$E_z = W_k(z). \tag{1.13c}$$

Further details of these expressions can be found the original work.[38,39] As a result of these steps, explicit formulations of this result (for example, for 2- or 3-phase systems), or approximate equations for $\langle |\mathbf{E}|^2 \rangle$, have historically been of interest. Nevertheless, this formalism indicates that, so long as the refractive index N and thickness d are known for each material, $\langle E_x^2 \rangle$, $\langle E_y^2 \rangle$, $\langle E_z^2 \rangle$ may be readily determined. The multiple beam interference effect poses challenges however at the same time it also potentially provides solution for the $\chi^{(2)}$ contribution ambiguity. In this thesis a simple and practical scheme was proposed to calculate the multiple beam interference effect for thin film SFG experiments, and predict a selective angle of incident and film thickness combination that could provide interfacial selectivity when both side of the film are $\chi^{(2)}$ active. The method was also extended to various polarization combinations for SFG experiments.

1.3 Charged Aqueous Interfaces

1.3.1 Electrical Double Layer Theories

A large part of this thesis is focused on investigating the surface charge of silica and silicone surfaces in aqueous environments using nonlinear optics. These studies were built on the theoretical foundation of electrical double layer (EDL) models. An EDL is defined as a double layer formed on a charged surface by the surface charge and its counter ions, resulting in an ionic cloud near the surface.[40] An electrical double layer is sometimes called an electrical diffuse double layer, since the distribution of counter ions takes a diffusive structure due to thermal motion of ions. When a surface is in contact with liquid, it can become charged in one of two ways: 1) the ionization or dissociation of surface groups and 2) adsorption of ions from solution onto a previously uncharged surface.[41] Regardless of how the electrical double layer was formed, it will always end up so that the surface charge is balanced by a region of equal but oppositely charged conterions.

There exists a number of theoretical models describing the EDL. The first and simplest model is proposed by Hermann von Helmholtz, who modeled the system as a simple capacitor (Figure 1.2a). The surface charge are neutralized by a molecular layer of counter-ions. The surface charge potential is linearly dissipated from the surface to the counter-ions. Later, Louis Georges Gouy and David Chapman introduced the diffuse model of the electric double layer, in which the electric potential decreases exponentially as the distance from the surface is increased. It is the most well-known Gouy-Chapman model (Figure 1.2b). However, the Gouy–Chapman model does not hold for highly charged double layers. This model was later improved by Stern who resolved the limitations of the Gouy-Chapman model by introducing a combination of the Helmholtz and the Gouy–Chapman model, which gave rise to a internal layer called Stern layer, which is similar to what Helmholtz proposed with the capacitor model, and an outer diffuse layer, Gouy-Chapman layer (Figure 1.2c).[40] Later discussion will be mostly based on this model unless

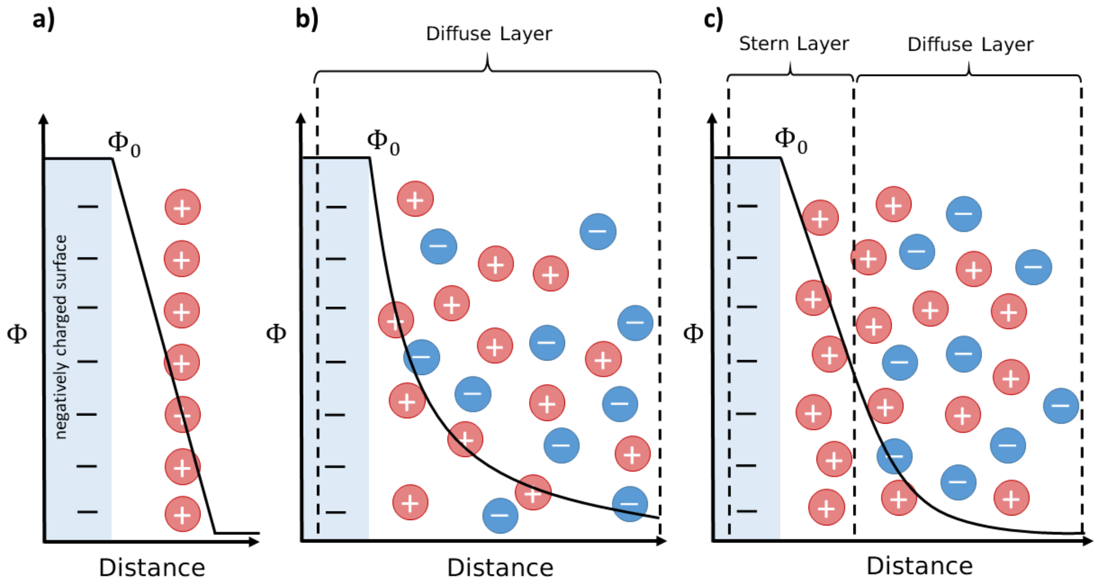

Figure 1.2: Illustration of a negatively charged aqueous interface and the potential (Φ) versus the distance to the interface, a) Helmholtz model, b) Gouy–Chapman model, c) Stern–Gouy–Chapman model.

otherwise noted.

The Poisson–Boltzmann equation is a second order partial differential equation describing the Gouy–Chapman model,[41]

$$\nabla^2\Phi = \frac{c_0 e}{\varepsilon\varepsilon_0}\cdot\left[\exp\left(\frac{e\Phi(x,y,z)}{k_B T}\right) - \exp\left(-\frac{e\Phi(x,y,z)}{k_B T}\right)\right]. \tag{1.14}$$

Here $\Phi(x,y,z)$ is the electric potential in three dimensions, e is the elementary charge, ε is the dielectric constant (relative permittivity) of the solvent, ε_0 is the permittivity of free space, c_0 is the bulk monovalent salt concentration, k_B is the Boltzmann constant, and T is the temperature in Kelvin. In most cases, the equation has to be solved numerically. However, in some situations, it can also be solved analytically. One example is a planar surface with a homogeneously distributed electric surface charge density σ on the x and y axes, and it generates a surface potential $\Phi_0 = \Phi(z=0)$, with z axis as the surface normal. This geometry happens to be the case involved in this thesis. In this case, the Poisson-

Boltzmann equation can be reduced to the z direction,

$$\frac{d^2\Phi}{dz^2} = \frac{c_0 e}{\varepsilon\varepsilon_0} \cdot \left[\exp\left(\frac{e\Phi(z)}{k_B T}\right) - \exp\left(-\frac{e\Phi(z)}{k_B T}\right)\right]. \tag{1.15}$$

There are two solutions to this equation. The first one is a linear approximation: one could apply Taylor expansion to the exponential functions, and take the first term as an approximation.[41] This leads to:

$$\Phi = \Phi_0 \cdot e^{-\kappa z}. \tag{1.16}$$

The potential decreases exponentially along the z axis. The decay length called the Debye length is given by $\lambda_D = \kappa^{-1}$. The reciprocal Debye length κ is,

$$\kappa = \sqrt{\frac{2c_0 e^2}{\varepsilon\varepsilon_0 k_B T}}. \tag{1.17}$$

This approximation would collapse at high potentials, however it is sufficient for cases where $|\Phi| \ll k_B T/e$. At room temperature it is $|\Phi| \leq 25$ mV. Another solution is the exact full solution to the Poisson–Boltzmann equation. With the full solution one can drop the assumption of low surface potential. The full solution usually takes the form of,[41]

$$\Phi(z) = \frac{2k_B T}{e} \cdot \ln\left[\frac{e^{y_0/2} + 1 + \left(e^{y_0/2} - 1\right) \cdot e^{-\kappa z}}{e^{y_0/2} + 1 - \left(e^{y_0/2} - 1\right) \cdot e^{-\kappa z}}\right], \tag{1.18}$$

where y_0 is defined as the dimensionless potential at the surface $y_0 \equiv e\Phi_0/k_B T$. According to trigonometry relationships, the solution takes an alternative form,[42]

$$\Phi(z) = \frac{2k_B T}{\mathrm{e}} \cdot \ln\left[\frac{1 + \tanh(y_0)e^{-\kappa z}}{1 - \tanh(y_0)e^{-\kappa z}}\right] = \frac{2k_B T}{\mathrm{e}} \cdot \tanh^{-1}[\tanh(y_0)e^{-\kappa z}]. \tag{1.19}$$

With the full solution, one would be able to solve the electric potential at any given distance z from any charged interface without the assumption of low surface potential.

1.3.2 Poisson–Boltzmann Equation in Non-linear Optics Studies

1.3.2.1 Eisenthal Formulation

With a charged surface presented in an aqueous solution, the water molecules surrounding the surface would also realign and reorient since water molecules are polar. This enables non-linear optics studies of charged water interfaces, since there exhibits break of centrosymmetry. Eisenthal first proposed that based on the origin of the electric field, the non-linear response can be separated into two categories: those that come from the water molecules near the surface not affected by the electric field, and those from the water molecules reoriented by the charged interface.[43] For the former:

$$\begin{aligned} E \propto P_S^{(2)} &= \int_0^\infty \chi_{\mathrm{B}}^{(2)} \delta(z) E(\omega_1) E(\omega_2) \mathrm{d}z \\ &= \chi_S^{(2)} E_{\omega_1} E_{\omega_2}, \end{aligned} \tag{1.20}$$

and for the latter:

$$P_B^{(3)} = \chi_B^{(3)} E_{\omega_1} E_{\omega_2} E_{\mathrm{DC}}. \tag{1.21}$$

Here $\chi^{(3)}$ is the third-order nonlinear susceptibility and E_{DC} is the static electric field at the charged interface. This polarization can be projected onto the surface, to create a surface polarization defined in the same way as $P^{(2)}$ by integrating along the z axis (normal to the surface) from $z = 0$ (plane of the surface) to $z = \infty$ to arrive at

$$\begin{aligned} P_S^{(3)} &= \chi_B^{(3)} E(\omega_1) E(\omega_2) \int_0^\infty E_{\mathrm{DC}}(z) dz \\ &= -\chi_B^{(3)} E(\omega_1) E(\omega_2) [\Phi_{(\infty)} - \Phi_0] \\ &= \chi_B^{(3)} E(\omega_1) E(\omega_2) \Phi_0. \end{aligned} \tag{1.22}$$

The potential at infinity is assumed to be zero. So the expression for the total electric field is as follow:

$$E \propto P = \chi^{(2)} E(\omega_1) E(\omega_2) + \chi^{(3)} E(\omega_1) E(\omega_2) \Phi_0. \tag{1.23}$$

1.3.2.2 Roke and Tian Formulation (f_3)

It is worth pointing out that in the Eisenthal formulation it was assumed that the optical fields are independent of z, which means the phases of the incoming and returning fields are assumed to be constant where the static electric field is non-zero. The validity of the assumption was proved to be compromised in a lot of cases, and a z-dependence of the incoming beams have to be incorporated. To do this, Roke[44] and Tian[45] proposed the f_3

formulation. First one will consider the wave-vector mismatch along z, Δk_z,

$$\Delta k_z = k_{1z} + k_{2z} - k_{0z}, \tag{1.24}$$

with

$$k_{iz} = \frac{\omega_i}{c\sqrt{n(\omega_i)^2 - \sin(\theta_i)^2}}. \tag{1.25}$$

Here $n(\omega_i)$ is the corresponding refractive index and θ_i is the incident angle. So now $P_S^{(3)}$ can be written as,

$$\begin{aligned} P_S^{(3)} &= \int_0^{+\infty} \chi^{(3)} E(\omega_1) E(\omega_2) E_{\mathrm{DC}}(z) e^{i\Delta k_z z} dz \\ &= \chi^{(3)} E_{\omega_1} E_{\omega_2} \int_0^{+\infty} \left(-\frac{d}{dz}\Phi(z) \right) e^{i\Delta k_z z} dz \\ &= \chi^{(3)} E_{\omega_1} E_{\omega_2} (\Phi_0 + i\Delta k_z \int_0^{+\infty} \Phi(z) e^{i\Delta k_z z} dz). \end{aligned} \tag{1.26}$$

And now use the linearized Poisson-Boltzmann equation $\Phi(z) = \Phi_0 e^{-\kappa z}$,

$$P_S^{(3)} = \chi^{(3)} E_{\omega_1} E_{\omega_2} \Phi_0 \frac{\kappa}{\kappa - i\Delta k_z}, \tag{1.27}$$

and define that $f_3 = \frac{\kappa}{\kappa - i\Delta k_z}$, so the total electric field can be expressed as,

$$E \propto \chi^{(2)} + \Phi_0 f_3 \chi^{(3)}. \tag{1.28}$$

As shown in the final equation above, since Φ_0 is real, when $\chi^{(2)}$ and $\chi^{(3)}$ are real, the phase of f_3 comes solely from the wavevector mismatch. Here Φ_0 only scales the magnitude of the $f_3\chi^{(3)}$ term. The formulation is similar to that of Eisenthal, but an extra f_3 was added to account for the wavevector mismatch.

1.3.2.3 Wen, Hore and Tyrode Formulation (g_3)

As mentioned in Section 1.3.1, the linearized solution for the Poisson–Boltzmann will collapse at higher surface potentials. To make it applicable to such interfaces, Wen *et al.*[46] and Hore and Tyrode[47] proposed the g_3 formulation. Similar to Roke and Tian's approaches, the g_3 formulation also takes the wave-vector mismatching of the incoming beams into account. First one can define $\xi = \tanh\left[e\Phi_0/4kT\right]$, so that the full solution for the Poisson–Boltzmann equation becomes:

$$\begin{aligned}\Phi(z) &= \frac{2kT}{e}\ln\left[\frac{1+\xi \mathrm{e}^{-\kappa z}}{1-\xi \mathrm{e}^{-\kappa z}}\right] \\ &= \frac{4kT}{e}\cdot\frac{1}{2}\left[\ln(1+\xi e^{-\kappa z})-\ln(1-\xi e^{-\kappa z})\right] \\ &= \frac{4kT}{e}\tanh^{-1}(\xi e^{-\kappa z}).\end{aligned} \tag{1.29}$$

When one takes the Taylor expansion of $\tanh^{-1}(\xi e^{-\kappa z})$ about $z=0$,

$$\Phi(z) = \frac{4kT}{e}\sum_{n=1}^{\infty}\frac{(\xi \mathrm{e}^{-\kappa z})^{2n-1}}{2n-1}. \tag{1.30}$$

Similar to Equation 1.26,

$$P_S^{(3)} = \chi^{(3)}E(\omega_1)E(\omega_2)(\Phi_0 + i\Delta k_z\int_0^{+\infty}\Phi(z)e^{i\Delta k_z z}dz), \tag{1.31}$$

and the integration can be solved by,

$$\begin{aligned}\int_0^{\infty}\Phi(z)\mathrm{e}^{\mathrm{i}\Delta kz}\mathrm{d}z =& \frac{4kT}{e}\int_0^{\infty}\left[\mathrm{e}^{\mathrm{i}\Delta kz}\sum_{n=1}^{\infty}\frac{(\xi \mathrm{e}^{-\kappa z})^{2n-1}}{2n-1}\right]\mathrm{d}z \\ =& -\frac{4kT}{e}\sum_{n=1}^{\infty}\frac{\xi^{2n-1}}{(2n-1)[\mathrm{i}\Delta k-\kappa(2n-1)]}.\end{aligned} \tag{1.32}$$

Therefore $P_S^{(3)}$ can be written as,

$$P_S^{(3)} = \chi^{(3)}E(\omega_1)E(\omega_2)\left(\Phi_0 - \frac{4ikT\Delta k_z}{e}\sum_{n=1}^{\infty}\frac{\xi^{2n-1}}{(2n-1)[\mathrm{i}\Delta k-\kappa(2n-1)]}\right). \tag{1.33}$$

And g_3 is defined as,

$$g_3 = \Phi_0 - \frac{4ikT\Delta k_z}{e}\sum_{n=1}^{\infty}\frac{\xi^{2n-1}}{(2n-1)[\mathrm{i}\Delta k-\kappa(2n-1)]}. \tag{1.34}$$

Finally,

$$E \propto \chi^{(2)} + g_3\chi^{(3)}. \tag{1.35}$$

Comparing to Equation 1.28, $\chi^{(3)}$ is modulated with a single g_3 term. More importantly, the surface potential Φ_0 scales the real and imaginary part of g_3 differently, making the phase of

g_3 dependent of not only the wave-vector mismatch but also Φ_0. The g_3 formulation depicts the actual physical process more accurately, it also allows measurement of the surface potential of solid–aqueous interfaces at lower ionic strengths. The details will be discussed in Chapter 7.

1.4 Scope of the Thesis

This thesis starts by introducing a method making use of the multiple beam interference phenomenon to selectively probe one side of a thin-film in SFG experiments. It is essential for interpreting experimental results and conducting functional group orientation analyses correctly. This method was also extended to multiple polarization combinations. Following that, the thesis presents a temperature-dependent study of methyl orientation on PDMS surfaces exposed to two liquids representing hydrophobic and hydrophilic environmental conditions. To showcase the methodology of determining surface charge of a solid–aqueous interface using sum frequency generation, the thesis presents a study of surface charge of silica–water interface, and discovery of enhanced deprotonation behavior of silica surface functional groups under elevated temperatures. Next the thesis demonstrates the interpretation of sum frequency generation data of PDMS–water interface under increasing ionic strength using ion adsorption models, and determining the surface charge density and hence surface potential under different ionic strengths. Finally, a unified theory for interpreting experimental results at charged aqueous interfaces, applicable to both off-resonance and on-resonance nonlinear spectroscopy experiments are proposed.

Chapter 2

Selective Probing of Thin Film Interfaces Using Internal Reflection Sum-Frequency Spectroscopy[*,†]

2.1 Introduction

Over the past three decades, visible-infrared sum-frequency generation (SFG) spectroscopy has developed into a feature rich structural probe of surfaces and buried interfaces.[36,48,49] Its surface specificity stems from the fact that, under the electric dipole approximation, the second-order electric susceptibility $\chi^{(2)}$ is non-zero only in regions that lack an inversion centre, i.e. in regions over which there is no point such that $(x, y, z) \rightarrow (-x, -y, -z)$.[29] Niche applications are therefore found at the interface between two centrosymmetric media, such as air, bulk liquids, and isotropic solids including polymers.[31,50] In such cases, the intensity of the i-polarized SFG signal is related to the intensity of the incident j-polarized visible and k-polarized infrared beams through

$$I_{i,\mathrm{SFG}} = \frac{8\pi^3 \omega_{\mathrm{SFG}}^2 \sec^2 \theta_{\mathrm{SFG}}}{c^3 n_{\mathrm{SFG}} n_{\mathrm{vis}} n_{\mathrm{IR}}} |\chi_{ijk,\mathrm{eff}}^{(2)}|^2 I_{j,\mathrm{vis}} I_{k,\mathrm{IR}}. \tag{2.1}$$

---

[*] Reproduced in part from Azam, M. S.; Cai, C.; Hore, D. K. "Selective Probing of Thin-Film Interfaces Using Internal Reflection Sum-Frequency Spectroscopy." *J. Phys. Chem. C* **123**, 23535–23544 (2019). Copyright 2019 American Chemical Society.

[†] All data collection, including preparation of polymer surfaces and solutions, and measurement of SFG spectra performed by Azam. Treatment of data, model development, and analysis of data done by Cai. Azam, Cai, and Hore contributed to the discussion of the results, and to the writing of the manuscript.

Elements of the effective second-order susceptibility are related to the actual second-order susceptibility through the relation

$$\chi^{(2)}_{ijk,\mathrm{eff}} = L_{ii,\mathrm{SFG}} : \chi^{(2)}_{ijk} \cdot L_{jj,\mathrm{vis}} \cdot L_{kk,\mathrm{IR}} \tag{2.2}$$

where L_{jj} and L_{kk} relate the incoming visible and infrared electric fields to the corresponding fields at the interface where $\chi^{(2)} \neq 0$, and L_{ii} is the equivalent local field correction for the SFG field generated at the interface to be propagated out of the material.

In addition to considering a single interface between two semi-infinite media, there is considerable interest in applying SFG spectroscopy to stratified interfaces consisting of one or more layers. Among such samples, one of the most commonly-encountered systems is a polymer film spin-coated onto a substrate, with a polymer thickness in the range of tens of nanometers up to a few hundred nanometers. As facile analysis of the SFG signal to extract quantitative structural information relies on smooth surfaces that can generate specular reflection, the film thickness must generally be kept below 1000 nm. However, the experimental convenience of spin coating films with this range of thicknesses presents an analysis challenge, as multiple beam interference necessarily occurs for the SFG, visible, and infrared beams, as is well known in the linear optics community.

There have been many schemes proposed for dealing with the effects of multiple beam interference in SFG spectroscopy[51–62] and these have been successfully applied to aid in the interpretation of many systems.[63–68] Approaches generally fall into three categories: those based on the Airy formulas,[32,54–58,60,65–68] Abèles formalism,[69] or a transfer matrix approach.[51–53,59,61,62,64] These techniques are all capable of generating the same results, but are ideally suited to specific systems. For example, the geometric converging infinite series in the Airy approach is cumbersome to expand when there are more than a few phases. Matrix techniques have the advantage of being easily extended to systems with an arbitrary number of layers, but result in solutions that are sometimes not obvious in the case where there is only one film present. In this account, we first discuss some practical considerations from an experimental perspective, highlighting cases where the phases are either sufficiently thin or sufficiently thick so as to not require any interference calculations. We then present a formalism based on Abèles method that can be described succinctly when applied to a single thin film. Finally, we present a visualization method that is particularly useful when the objective is not to include the effects of multiple sources of SFG from $\chi^{(2)}$ terms present at different interfaces, but to aid in the selection of experimental geometries that suppress signals from the undesired interface. We provide a practical scheme by which these methods can be applied, and demonstrate results with a polydimethylsiloxane film exposed to air, water, and a perfluorinated liquid.

2.2 Experimental

2.2.1 Sample preparation

Thin films of PDMS were prepared on IR-grade fused silica hemicylinder prisms (25 mm × 25 mm flat face, Quartz Plus). The prisms were cleaned in a 500 mL glass beaker containing piranha solution, a 3:1 mixture of sulfuric acid and 30% hydrogen peroxide, for 1 h. *(Note: use caution, piranha solution reacts explosively with organic compounds, should not be mixed with any organic materials.)* They were then transferred into a 500 mL Teflon beaker and copiously rinsed (5 × 300 mL) with 18.2 MΩ·cm deionized water (Milli-Q), then rinsed individually under a stream for 30 s, sonicated in 300 mL water for 2 min, and again rinsed with water (2 × 300 mL). The prisms were then placed in a preheated vacuum oven at 85°C for 1 h prior to PDMS coating. PDMS solutions were prepared using a Sylgard 184 silicone elastomer kit (Dow Corning). The base and curing agent were dissolved in spectral grade $CHCl_3$ (Fisher) to prepare 5% (wt/wt) solutions of each and then mixed in a 10:1 (A/B, wt/wt) ratio to obtain a 5% (wt/wt) solution. The prism was secured in a custom chuck adapted for our spin-coater (Specialty Coating Systems, Inc.). Approximately 300 μL of PDMS solution was placed on the flat face of the hemicylindrical prism and cast at 5000 rpm for 5 min. Finally, the samples were placed in an oven and cured at 85°C for 4 h under vacuum.

2.2.2 Film thickness measurement and selection

For subsequent data treatment, we need to know the precise thickness of the PDMS films. However, the challenge is to determine the thickness in a way that does not destroy or contaminate the films, as it is ideal to characterize them prior to SFG measurements. Also, the measurement should be fast (on the timescale of minutes) to prevent exposure to the environment that would also result in eventual contamination. Direct profilometry measurements are therefore out, as several scratches would need to be made (that could also damage the prism) and those measurements are time-consuming. Ellipsometry is not possible as there is not sufficient refractive index contrast between the polymer and glass. We have therefore developed an alternate two-step method that overcomes these challenges.

Reference films of PDMS were prepared on glass microscope slides (Fisher Scientific) following the aforementioned procedure, with the concentration within a range of 2.5% to 10.0% to obtain variable thicknesses. The thickness of the spin-coated PDMS on microscopic slides was then measured using stylus profilometer (Bruker Dektak XT). Several scratches were made on the freshly prepared substrate using a razor blade and the film thicknesses were obtained from the respective depth profiles. The average thickness of multiple measurements are plotted as a function of the PDMS concentration used to prepare the film in Figure 2.1a. Next, Raman spectra were recorded (Renishaw inVia reflex) after adjusting the sample height to maximize the signal. This procedure works since the depth resolution (ca. 5 μm using a 0.75 NA objective) was much larger than the film thickness. The Raman intensities obtained at 2905 cm^{-1} were then plotted as a function of the thickness measured by the profilometry as shown in Figure 2.1b. The correlation between the Raman intensity and the film thickness from this calibration eventually allowed us to determine the thickness of the PDMS film, particularly on the hemicylindrical prisms, simply by knowing the Raman intensity of the 2905 cm^{-1} peak.

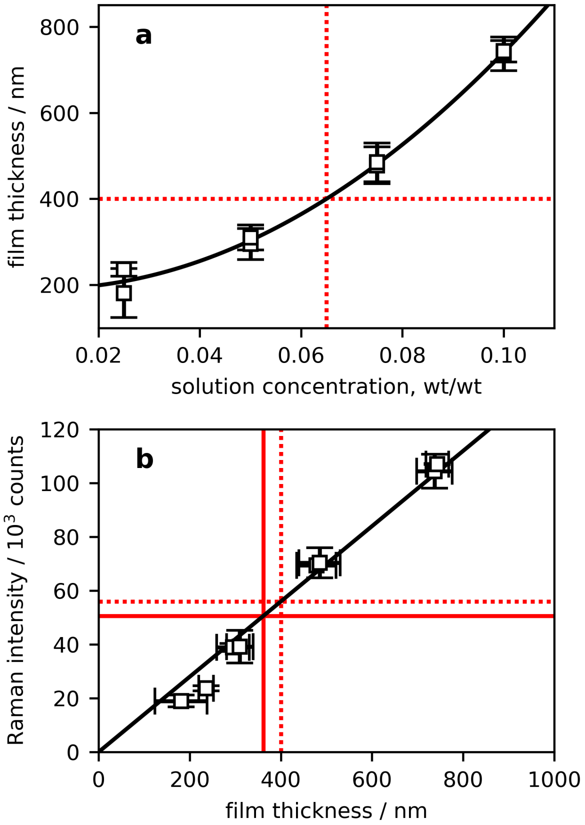

Figure 2.1: (a) Profilometry measurements of PDMS film thickness for various concentrations of PDMS in $CHCl_3$. (b) Correspondence between Raman scattering intensity of the 2905 cm^{-1} peak and the film thickness. Reprinted with permission from Ref. 33. Copyright 2019 American Chemical Society.

2.2.3 Description of the laser system

Full details of the laser system used for SFG spectroscopy have been provided previously.[70] In brief, a wavelength-scanning $\approx$ 20 ps SFG spectrometer (Ekspla, Lithuania) with nominally 4 cm^{-1} bandwidth in the IR has been used with custom stages that enable the sample and detector to be rotated about the same axis, in line with the solid (film)–liquid interface at the flat side of the hemicylindrical prism as shown in Figure 2.2. For a given film thickness, this enables the incident beam angles to be set with a precision of $\pm 0.3°$ for the visible beam on account of the +750 mm focal length lens, and $\pm 1.7°$ for the IR beam using a +150 mm lens. This spread of angles was calculated using the

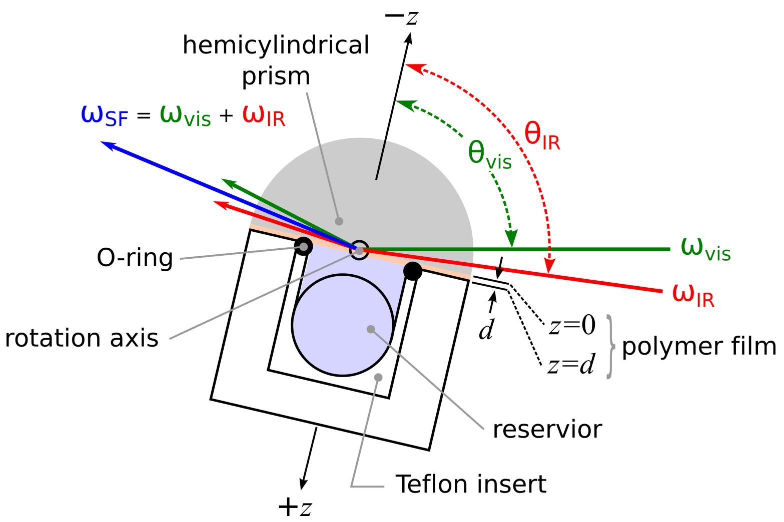

Figure 2.2: Schematic of the sample cell, illustrating the prism–polymer interface at $z = 0$ and the polymer–air/liquid interface at $z = d$. Fixed beam angles on the table with a common axis of rotation for the sample and detector enable any angle of incidence to be automatically selected while maintaining $\theta_{IR} - \theta_{vis} = 9.8°$. Reprinted with permission from Ref. 33. Copyright 2019 American Chemical Society.

collimated diameter of 6 mm for both IR and visible beams, and the numerical aperture of the individual focusing lenses. Both beams are fixed on the optical table, with the infrared angle of incidence greater by 9.8°. The detector angle was independently set using the known refractive index of the prism.

2.3 Results and Discussion

2.3.1 Single-layer thin film systems

The expressions provided in Eq. 1.13 may be used to solve for the electric field at any point z in a system consisting of an arbitrary number of layers. We now turn to the most commonly-encountered case of a single thin film composition a 3-phase system, for example air–film–substrate in external reflection, or substrate–film–aqueous in internal reflection. If we assume that there is no SFG generated in the bulk of any of the three phases, then signal can arise from only the initial film surface (which we refer to as $z = 0$) or the second film surface ($z = d$, where d is the film thickness). In external reflection, $z = 0$ is the air–film interface and $z = d$ is the buried film–substrate interface. In the case of internal reflection, the prism–film interface is at $z = 0$ while the film–air/aqueous interface is at $z = d$.

As the results of the interfacial field calculation are compact, it is worth stating them explicitly. First, the entire system is described by

$$\mathbf{M} \equiv \mathbf{M}_2 = \begin{bmatrix} \cos\beta_2 & -\frac{i}{p_2}\sin\beta_2 \\ -ip_2\sin\beta_2 & \cos\beta_2 \end{bmatrix} \tag{2.3}$$

resulting in the reflection coefficients

$$r = \frac{p_1(M_{11}+p_3M_{12})-(M_{21}+p_3M_{22})}{p_1(M_{11}+p_3M_{12})+(M_{21}+p_3M_{22})} \tag{2.4}$$

with r_s and r_p obtained using the appropriate definitions of p_1, p_2, and p_3 for s- and p-polarization as noted above. At the first interface the incident visible and infrared beams encounter, we then have the surface fields with respect to the incident fields

$$L^0_{xx} = \frac{E_x^{z=0}}{E_\mathrm{p}^{z=-\infty}} = (1-r_p)\cos\theta \tag{2.5a}$$

$$L^0_{yy} = \frac{E_x^{z=0}}{E_\mathrm{s}^{z=-\infty}} = 1+r_s \tag{2.5b}$$

$$L^0_{zz} = \frac{E_x^{z=0}}{E_\mathrm{p}^{z=-\infty}} = (1+r_p)\sin\theta\left(\frac{N_1}{N'}\right)^2. \tag{2.5c}$$

where N' is again the refractive index of the infinitesimal thin layer of polymer that generates the nonlinear polarization leading to SFG signal. As a first approximation, it is reasonable to consider $N' \approx N_2$, where the polymer surface has the same refractive index as the bulk polymer. However, this does not account for the microscopic components of the local field correction, namely the influence of a semi-infinite distribution of neighbouring molecules, and the anisotropy in the interfacial layer. For this reason a mixing rule, for example $N' \approx \frac{1}{2}(N_1+N_2)$ may be considered; more sophisticated expressions may be found in the literature.[71,72] Either way, we note that Eq. 2.5 has the same form as Eq. 1.6 (ultra thin film), except that r_p and r_s are now derived from a model (Eq. 2.4) that takes multiple reflections inside the thin film into account.

At the second interface, the local field correction factors are given by

$$L_{xx}^{d} = \frac{E_x^{z=d}}{E_{\mathrm{p}}^{z=-\infty}} = (1-r_p)\cos\theta\cos\beta_2 + i\frac{N_1\cos\theta_2}{N_2}(1+r_p)\sin\beta_2 \tag{2.6a}$$

$$L_{yy}^{d} = \frac{E_y^{z=d}}{E_{\mathrm{s}}^{z=-\infty}} = (1+r_s)\cos\beta_2 + i\frac{N_1\cos\theta}{N_2\cos\theta_2}(1-r_s)\sin\beta_2 \tag{2.6b}$$

$$L_{zz}^{d} = \frac{E_z^{z=d}}{E_{\mathrm{p}}^{z=-\infty}} = \left[\frac{N_1^2}{N_2^2}\sin\theta(1+r_p)\cos\beta_2 + i\frac{N_1\sin\theta\cos\theta}{N_2\cos\theta_2}(1-r_p)\sin\beta_2\right]\left(\frac{N_2}{N''}\right)^2 \tag{2.6c}$$

where N'' is the refractive index of the polymer film in the immediate region of second interface, for example $N'' \approx N_2$ or $N'' \approx \frac{1}{2}(N_2+N_3)$. Note that r_{p} and r_{s} are again provided by Eq. 2.4.

2.3.2 Interface selectivity

We now consider the ssp polarization scheme. Using Eq. 2.5 we plot $(L_y^0)_{\mathrm{SFG}}$, $(L_y^0)_{\mathrm{vis}}$, and $(L_z^0)_{\mathrm{IR}}$ in the left column of Figure 2.3. The equivalent results, but for the interface at $z = d$ are plotted in the middle column of Figure 2.3. As dispersion and absorptive effects are very important in the calculation of these quantities,[73] we have used frequency-dependent refractive index data for fused silica,[74] PDMS,[75,76] and water.[77] No infrared refractive index data was available for FC40, so we have used $N = 1.29$.[78] This is a reasonable approximation as FC40 has no IR resonances in the frequency range of our interest. We have compared these results to those calculated using Airy formulas, and using the transfer matrix approach[51–53] and found all three methods to be numerically identical. It is important to note that, in the case where both interfaces are SFG-active, the intensity is given by

$$\begin{aligned} I_{\mathrm{ssp}} &\propto \left| L_{yy}^0 L_{yy}^0 L_{zz}^0 \chi_{yyz,0}^{(2)} + L_{yy}^d L_{yy}^d L_{zz}^d \chi_{yyz,d}^{(2)} \right|^2 \\ &\equiv \left| (LLL)_0 \chi_0^{(2)} + (LLL)_d \chi_d^{(2)} \right|^2 \end{aligned} \tag{2.7}$$

and, even if the L factors are calculated, Eq. 2.7 can provide predictions only in the case where the magnitude and phase of both $\chi^{(2)}$ values are known. In other words, if only $|\chi_0^{(2)}|$ and $|\chi_d^{(2)}|$ are known (as can be readily determined from a combination of internal and

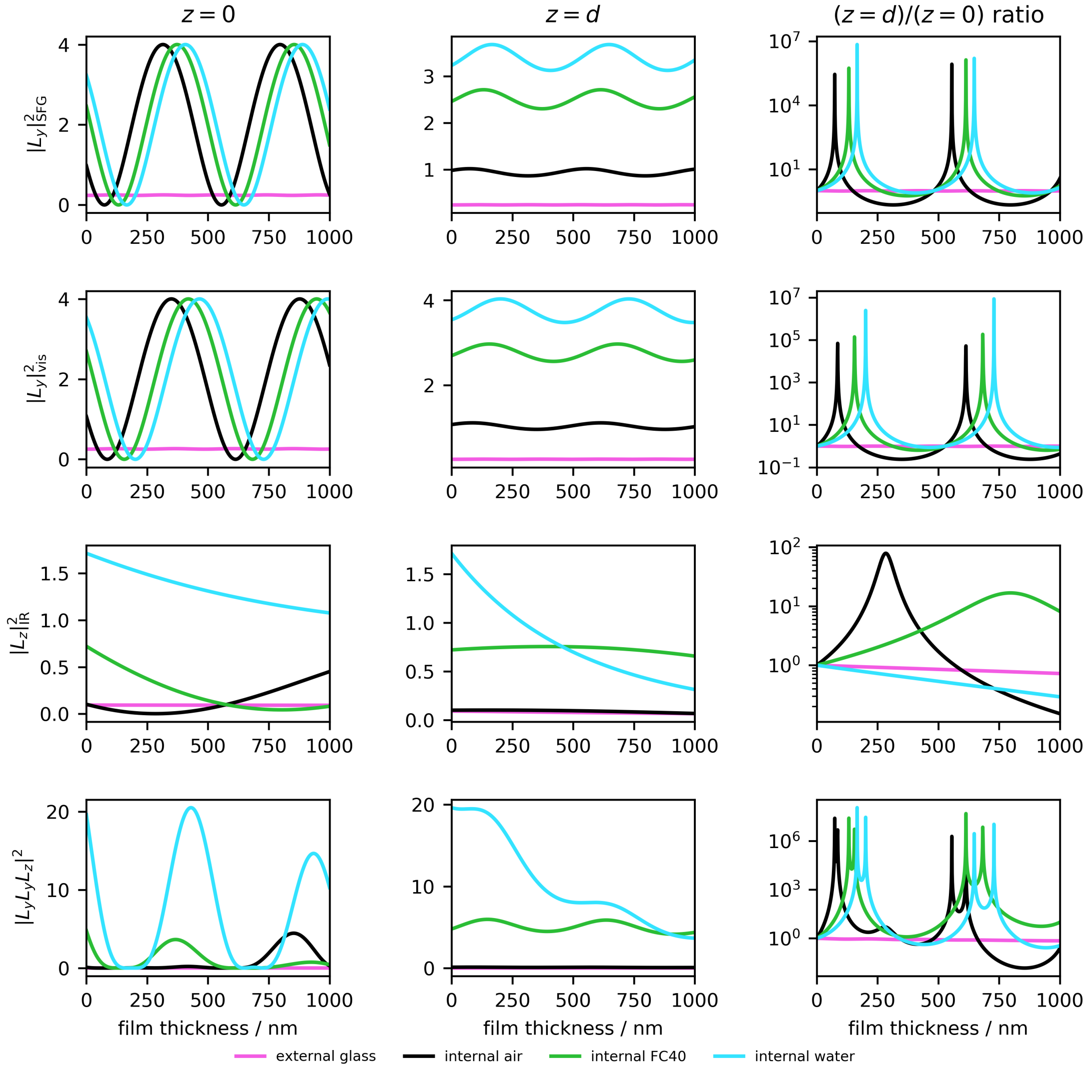

Figure 2.3: Mean square electric field amplitude, with respect to incident s- or p-polarized intensity at the first ($z = 0$, left column) and second ($z = d$, middle column) film interface for the SFG beam (top row), and incoming visible (second row) and infrared (third row) beams. The product of these three quantities, $|L_yL_yL_z|^2$, is plotted in the bottom row. In the right column, the ratio of each quantity at $z = d$ is plotted with respect to the corresponding values at $z = 0$ on a logarithmic scale. Results are illustrated for a PDMS film on glass (blue, $N_1 = 1$, beams incident from air), and internal reflection (N_1 corresponding to a silica prism), and N_3 corresponding to air (orange), water (red), and FC40 (green). Reprinted with permission from Ref. 33. Copyright 2019 American Chemical Society.

external reflection experiments from sufficiently thick films), the missing phase information prevents Eq. 2.7 from being applied.

Our approach, however is to arrive at combinations of the incident angles θ and film thickness d so that, when measurement of $\chi_0^{(2)}$ is desired, $L_y^0 L_y^0 L_z^0 \gg L_y^d L_y^d L_z^d$. Similarly, if our interest is in $\chi_d^{(2)}$ we look for a combination of angle and thickness for which $L_y^0 L_y^0 L_z^0 \ll L_y^d L_y^d L_z^d$. In cases where both interfaces are of interest, it is particularly intriguing to be able to prepare a film of thickness d and then locate two angles that achieve the desired interface selections. We start by considering the ratio of the results at $z = d$ to those at $z = 0$, as displayed in the right column of Figure 2.3. Large values of this ratio display a selectivity for the second interface, after the beams have travelled through the film thickness d, with the actual path lengths determined by the angles of incidence. The bottom right panel is the figure of merit, the ratio of the squares of the products $|(LLL)_d/(LLL)_0|^2$. We have used a logarithmic scale is order to highlight very large and small values of this ratio, as both are of interest. A difficulty associated with such a graphical representation is that these figures apply to only a specific set of visible and IR beam angles. Since there is a limit to the accuracy to which film thickness can be determined, it would be more useful to see large values of this ratio that exist over a range of thickness.

A proposed solution is to generate selectivity maps as shown in Figure 2.4. Here the individual values at $z = 0$ and $z = d$ are no longer shown, but the ratio is plotted directly, as a function of both angle of incidence and film thickness. The scaling challenge is addressed by coloring custom contour levels, regardless of the extent of the data. In our example, values of $|(LLL)_d/(LLL)_0|^2$ (or $|L^d/L^0|^2$ in the case of the individual beams) are red if they are greater than 100, and yellow for $10 < |(LLL)_d/(LLL)_0|^2 < 100$. Highlighting these custom contours simultaneously solves the reciprocal issue, as $|(LLL)_d/(LLL)_0|^2 < 0.01$ are dark blue and $0.001 < |(LLL)_d/(LLL)_0|^2 < 0.1$ are cyan. All other values $(0.1 < |(LLL)_d/(LLL)_0|^2 < 10$ are left white. In other words, white indicates that there is most likely insufficient selectivity of the two interfaces to make a distinction, and so that combination of thickness and angle is not useful.

A quick inspection of these results immediately reveals that external reflection geometries cannot, in general, be used to isolate contributions from a dielectric substrate–organic film vs film–air interface. For the internal reflection geometries, selectivity is possible, but only at angles above the critical angle. The rightmost column of Figure 2.4 is the only required piece of information to make experimental decisions, but the relative contributions of the SFG, visible, and infrared beams may be used to understand the final results. There is no combination of film thickness or angle that achieves selectivity of the infrared field at any interface. However, the multiplicative selectivity of the SFG and visible beams is sufficient to create geometries that are selective for either interface. One additional feature has been incorporated into Figure 2.4. Just because the ratio $|(LLL)_d/(LLL)_0|^2$ is large, doesn't mean that $|(LLL)_d|^2$ is of appreciable magnitude. In other words, it is not worth designing an experiment if the number of SFG counts will be below the noise level. We therefore incorporate one additional constraint in that $|(LLL)_d|^2$ must be greater than a threshold value, or else $|(LLL)_d/(LLL)_0|^2$ is colored white (instead of yellow or red). This value can be selected based on the sensitivity of the detector, of magnitude of the expected $\chi^{(2)}$ value. In this case, we have chosen unity. Likewise, cyan or blue is drawn only in the case where $|(LLL)_0|^2 > 1$.

2.3.3 Experimental demonstration

We now use the above models to present results for PDMS spectra at the surface of fused silica, air, a perfluorinated liquid (FC40), and water. There are a total of six possible experiments that can be performed, as illustrated in Figure 2.5. A typical workflow requires preparing a film close to the desired target thickness for the planned angle of incidence. For example, if we desire a film with a thickness of 400 nm, the crosshairs in Figure 2.1a indicate that we should aim for a 6.5% wt/wt solution for casting at 5000 rpm. However, after this film was prepared, instead of the anticipated 56,000 counts of Raman for the

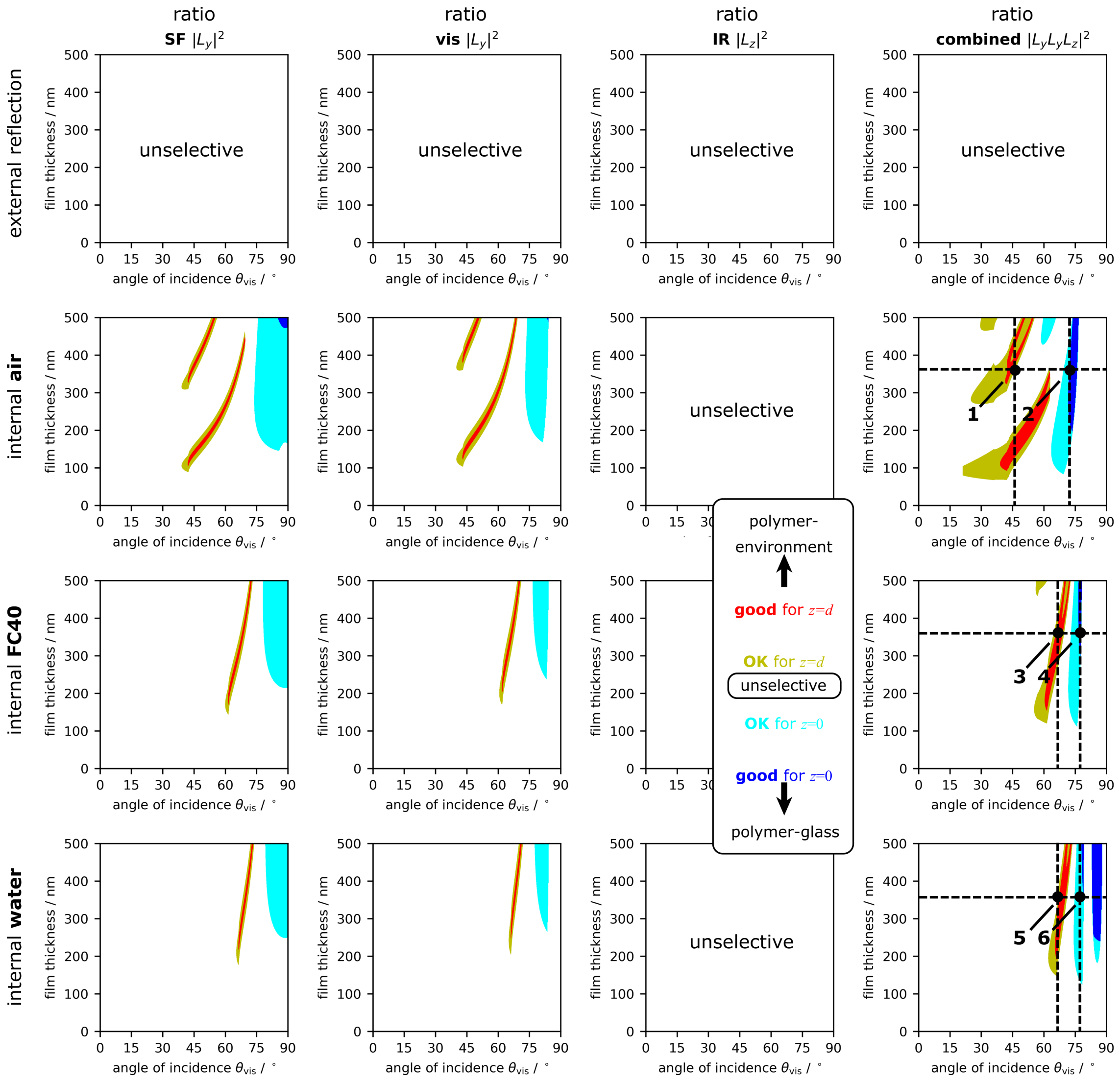

Figure 2.4: Ratio of the mean square fields L^d/L^0 as a function of film thickness and angle of incidence for the SFG beam (left column), visible (second column), infrared (third column), and product of the three factors ($|(LLL)_d/(LLL)_0|^2$, right column) for the case of external reflection (top row), and internal reflection with the environmental side of the PDMS being air (second row), FC40 (third row), or water (bottom row). Based on the local fields alone (i.e. no weighting from the relative $\chi^{(2)}$ contributions), white indicates insufficient selectivity for either interface. Values of thickness and angle that produce good selectivity ($|(LLL)_d/(LLL)_0|^2 > 10$) for the environmental side indicated in yellow; best selectivity ($|(LLL)_d/(LLL)_0|^2 > 100$) appear red. Likewise, good selectivity for the first interface ($|(LLL)_0/(LLL)_d|^2 > 10$) are in cyan; best sensitivity ($|(LLL)_0/(LLL)_d|^2 > 100$) are in dark blue. Reprinted with permission from Ref. 33. Copyright 2019 American Chemical Society.

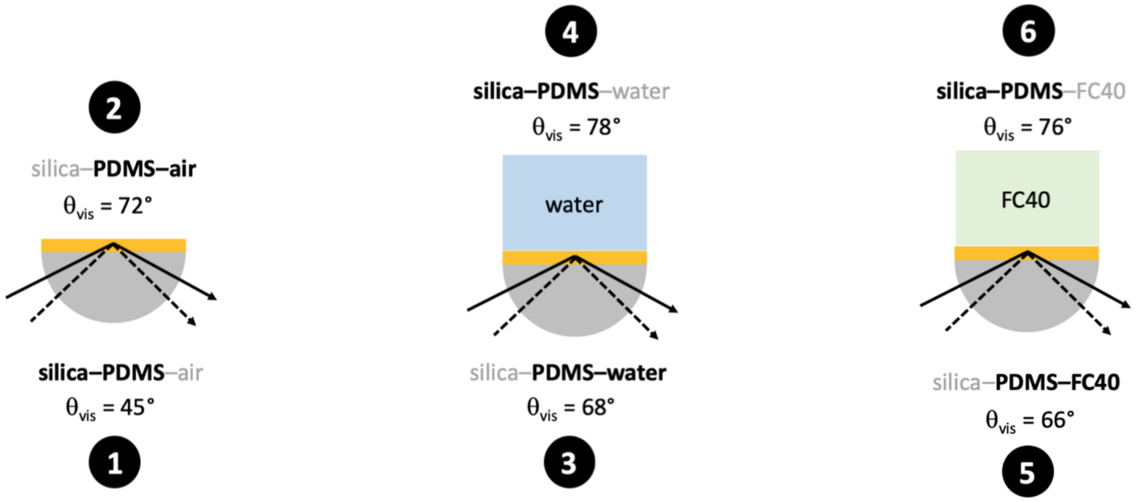

Figure 2.5: Six possible experiments that can be performed with PDMS on silica, adjacent to air, water, and FC40. In each case, $\theta_{\text{IR}} = \theta_{\text{vis}} + 9.8°$. Reprinted with permission from Ref. 33. Copyright 2019 American Chemical Society.

2905 cm^{-1} peak (dashed crosshairs in Figure 2.1b), 50,680 counts were obtained (solid crosshairs), indicating that we have made a film with a thickness of 362 nm, and the corresponding angles of incidence are recalculated.

Now we simply need to vary the angle of incidence as depicted in Figure 2.5 to selectively probe one of the two possible interfaces. Out of the six experiments performed with silica–PDMS–air, silica–PDMS–FC40, and silica–PDMS–water, we anticipated that the data obtained from the three silica–PDMS interfaces ($z = 0$) should be similar, and this is demonstrated in Figure 2.6a. On the other hand, when we probe the environmental sides we observed significantly different SFG spectra depending on the media it came in contact with. Two major peaks for PDMS are at 2910 cm^{-1} for the symmetric stretching and 2955 cm^{-1} for the antisymmetric stretching of the CH_3 group.[50,79–87] A mode near 2880 cm^{-1} has also been reported for the symmetric CH_2 stretch.[79,80,82–84] The ratio of the 2910 cm^{-1} and 2955 cm^{-1} modes has previously been observed to change depending on the hydrophobicity of the environment the CH_3 groups are interacting with, as PDMS has been shown to restructure when placed under water.[80,82,88] It has also been reported that 2910 cm^{-1} is the most intense mode when the environment is hydrophobic (air and FC40 in our case), whereas the intensity of the 2955 cm^{-1} is higher when the media is hydrophilic (water and glass in our case).[80,82,88] All the SFG spectra from the silica–PDMS interface obtained from the different experiments showed a predominant peak at 2955 cm^{-1} with a shoulder at 2910 cm^{-1} owing to the hydrophilicity of the silica. PDMS–water also produced a similar spectrum as shown in Figure 2.6b. On the contrary, for hydrophobic media we observed a flipping of relative intensity of these two peaks. Although FC40 is considered to be ultra hydrophobic, we found that the CH_3 antisymmetric stretching intensity was higher than that observed at the PDMS–air interface. This points to a difference in molecular interaction that is also indicated by a 10 cm^{-1} spectral shift from 2950 cm^{-1} for FC40 to 2960 cm^{-1} for air.

These results are intriguing as, for a fixed film thickness, the prism–film interface ($z = 0$) can be probed with a given set of angles, the film–air interface ($z = d$) with another set of angles, and then an aqueous solution can be introduced to study the film restructuring (at $z = d$) simply by rotating to a third set of angles. If the solution conditions are varied in the experiment, a setup such as our motorized hemicylinder enables continuous monitoring of the film–solution interface as long as the refractive index of medium 3 is known or can be estimated.

A point of caution is that the formalism presented here assumes only dipolar contributions to $\chi^{(2)}$.[30,49] However, one cannot rule out the possibility of quadrupolar contributions to $\chi^{(2)}$, as has been demonstrated in several experiments.[89–95] Selectively probing the interface at $z = d$ necessitates the visible and infrared beams traversing the polymer film, so quadrupolar contributions may be significant. However, in cases where measurements of sufficiently thick films is possible in both internal and external reflection geometries, the spectra may be compared to those obtained for thin films.

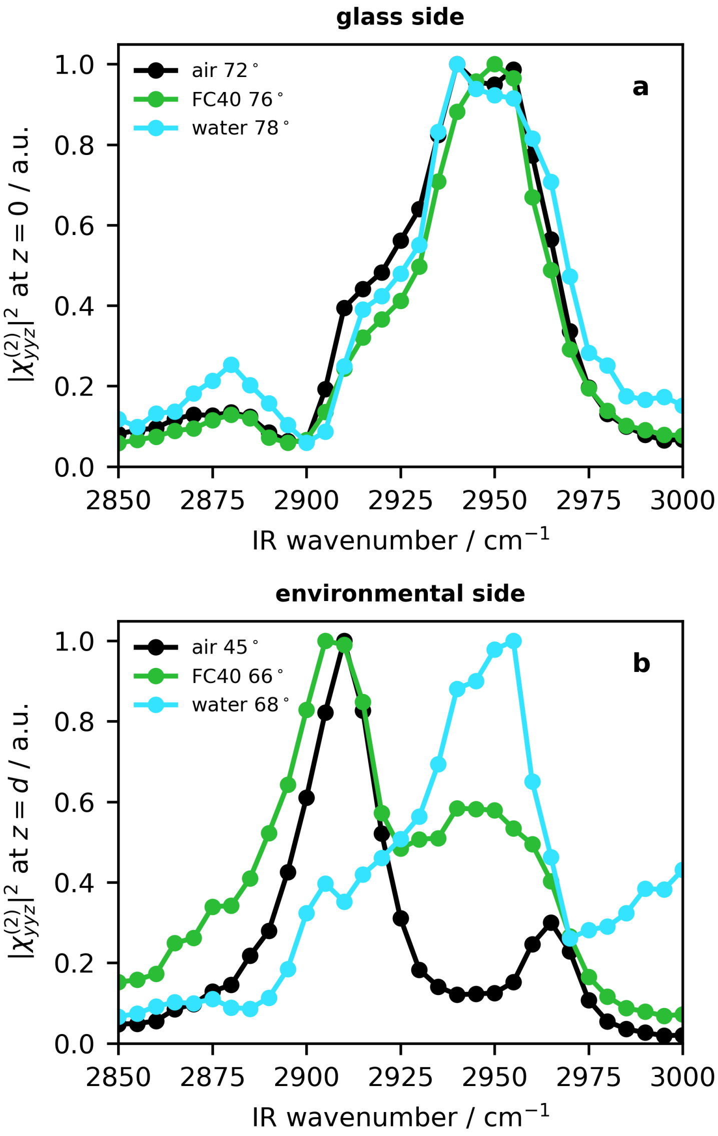

Figure 2.6: SFG spectra corresponding to the 6 different scenarios presented in Figure 2.5 and identified in Figure 2.4 for (a) the prism–film interface at $z = 0$ and (b) the film–air/FC40/water interfaces at $z = d$. Reprinted with permission from Ref. 33. Copyright 2019 American Chemical Society.

2.4 Conclusions

We have provided explicit expressions for the commonly-encountered case of a film deposited on a substrate with SFG potentially originating at the first ($z = 0$) or second ($z = d$) interface. In the case of external reflection (where the air–film interface is located at $z = 0$) there is no combination of thickness or angle that can selectively probe either interface when the film is coated on a dielectric substrate. However, the two interfaces can be selectively probed when using an internal reflection geometry. By plotting the ratio of the local field factors at $z = d$ to those at $z = 0$ using a logarithmic coloring scheme, suitable values of the film thickness and angles may be readily identified, even without any prior knowledge of the relative magnitude and phase of the $\chi^{(2)}$ contributions at either interface.

Chapter 3

Extension of the Selective Probing of Thin Film Interfaces to Multiple Beam Polarizations[*,†]

3.1 Introduction

Thin films play an important role in coatings, electronics, surface modification, and biomedical applications.[96–102] Characterizing the molecular structure at the surface of the films is a key component to understanding their chemical and physical properties. Another application of thin films, particularly in the case of polymers, is the creating of smooth surfaces of uniform thickness by spin coating. Even when the bulk material properties are of interest, optical techniques based on reflection measurements often require low roughness. Such optical methods are often desirable as they are non-destructive, can be performed under ambient or buried conditions (for example next to liquids), and the characterization can often be performed in situ to mimic the system under relevant environmental parameters. Within this subset, vibrational spectroscopy offers label-free probing of sub-molecular entities and can therefore provide information on composition, molecular orientation, and conformation.[103–105] In cases where the surface properties are

---

[*] Reproduced in part from Cai, C.; Azam, Md. S.; Hore, D. K. "Probing Either Side of Thin Films Using Vibrational Sum Frequency Spectroscopy in Multiple Beam Polarizations." *J. Phys. Chem. C* **125**, 12382–12389 (2021). Copyright 2021 American Chemical Society.

[†] All data collection, including preparation of polymer surfaces and solutions, and measurement of SFG spectra performed by Azam. Treatment of data, model development, and analysis of data done by Cai. Cai, Azam, and Hore contributed to the discussion of the results, and to the writing of the manuscript.

targeted for analysis, the challenge is to gain sufficient selectivity in excluding contributions from the bulk polymer film. Second order nonlinear optical methods have been recognized as premiere tools for such characterization as they, under the electric dipole approximation, generate signals only from regions of the sample where the inversion symmetry is broken, i.e. the interfaces.[29] Visible-infrared sum-frequency generation (SFG)[30,36] is a second-order technique that combines the sought-after characteristics of all these methods, as it can probe molecular vibrations at interfaces.

It is well-known that, when the film thickness is on the order of the probe wavelength or smaller, interference effects need to be taken into consideration, even when multiple interfaces contain only a single SFG-active layer,[32] and especially in the case when both sides of the thin film (substrate side, and exposed or environmental side) have ordered arrangements of molecules such that the second-order susceptibility $\chi^{(2)}$ is non-zero to produce SFG responses that coherently add at the detector.[51–60,62,65,106–108] This situation presents a simultaneous challenge and opportunity. It is challenging in the sense that signals from the substrate–film and film–ambient interfaces add depending on the magnitude and phase of the constituent responses. Even in the case where $\chi^{(2)}$ at one interface is small compared to $\chi^{(2)}$ at the other, the interference cross term can contribute in a significant way to the measured response.[51,53] In some cases, the interface of interest has a marked appearance in the spectra; in other cases the $|\chi^{(2)}|^2$ spectra of both interfaces are similar in appearance, and so there is no obvious way to distinguish them. This then presents obstacles in the analysis, as mixed contributions may be present. And then there is the silver lining: it is possible to make use of the interference to suppress signals for a particular interface in order to simplify the analysis and target a particular side of the film.[33,56–58,106] We have recently demonstrated that, when films are coated on an optic such as a hemicylinder that enables facile control of the angle of incidence, an internal reflection geometry may be used to selectively probe either interface by tuning the angle.[33] When the refractive index of the environmental side is changed (e.g. when film–air becomes film–water and then film–solution), the ability to change the angle mid-experiment enables the interface of interest to remain selected. Our initial demonstration was for the widely-used SSP polarization scheme (p-polarized infrared and s-polarized visible incident, s-polarized SFG detected). There are many situations in which spectra need to be collected in other or multiple polarization schemes. The classic example is when information on the molecular orientation is to be extracted, and comparing the response of a single vibrational mode in two different polarizations eliminates the dependence of the molecular number density.[82, 109–114] Another situation is that of films on metal substrates, where the so-called surface selection rules suppress molecular response from s-polarized infrared light due to the small values of the s-polarized local field.[55, 115–117]

In this work, we extend the theory and experimental demonstration to the useful SPS and PPP polarization schemes. Although the detailed conclusions depend on the specific materials (thickness and refractive index of all phases) of the particular system, our aim is to provide a simple and straightforward method that is accessible to anyone interested in selective probing of thin films. An important part of the experiment planning is the inherent trade-off between selectivity and the size of the signal. For example, a high selectivity is not useful in practice if the magntiude of the response is too small. We provide an illustration of these concepts and guidelines for a more general interpretation using a polymer thin film.

3.2 Background

Detailed discussion of multiple beam interference models and their application to SFG spectroscopy appear in the literature.[51–60, 62, 65, 106–108] Our formulation, that achieves the same result in a compact manner, and therefore straightforward to implement with minimum effort, is described in Ref. 33. We emphasize that the simplicity of this method comes with a limitation, in that only the first and last interfaces can be SFG-active. For a more general solution that can handle an arbitrary number of SFG-active layers, see

Refs. 51 and 52. However, the case of a single thin film (including the possibility of additional surface treatment or monolayers on either side) as addressed here is the most common. In brief, we consider a film of thickness d with complex refractive index $N_2 = n_2 + i\kappa_2$ sandwiched between a transparent incident medium (prism for internal reflection) with index $N_1 \approx n_1$ and a medium with index N_3. For film surfaces exposed to air, $N_3 = n_3 = 1$; when water is put next to the film, we consider $N_3 = n_3 + i\kappa_3$. The interaction of light with the film may be described by the matrix

$$\mathbf{M} = \begin{bmatrix} \cos\beta_2 & -\frac{\mathrm{i}}{p_2}\sin\beta_2 \\ -\mathrm{i}p_2\sin\beta_2 & \cos\beta_2 \end{bmatrix}. \tag{3.1}$$

where $p_2^s = N_2\cos\theta_2$ for s-polarized light, $p_2^p = p_2^s/N_2^2$ for p-polarized light,[38,39] and θ_2 is the refracted angle. The quantity $\beta_2 = 2\pi d p_2/\lambda$ accounts for the phase difference incurred by propagating through the film. Using the appropriate choice of p_2^s or p_2^p in Eq. 3.1 results in the Fresnel reflection coefficients r_s and r_p using

$$r = \frac{p_1\left(M_{11} + p_3M_{12}\right) - \left(M_{21} + p_3M_{22}\right)}{p_1\left(M_{11} + p_3M_{12}\right) + \left(M_{21} + p_3M_{22}\right)} \tag{3.2}$$

where p_1 and p_3 are defined in an analogous manner to p_2 as described above. We are interested in the local fields at two specific locations along the surface normal, z. The local field at $z = 0$ (the film–substrate interface) in Cartesian coordinates is obtained in relation to the incident field ($z = -\infty$) in the s/p basis from

$$\begin{bmatrix} E_x \\ E_y \\ E_z \end{bmatrix}_{z=0} = \begin{bmatrix} L_{xx}^0 & 0 & 0 \\ 0 & L_{yy}^0 & 0 \\ 0 & 0 & L_{zz}^0 \end{bmatrix} \begin{bmatrix} E_p \\ E_s \\ E_p \end{bmatrix}_{z=-\infty} \tag{3.3}$$

with

$$L_{xx}^0 = \left(1 - r_{\mathrm{p}}\right)\cos\theta \tag{3.4a}$$

$$L_{yy}^0 = 1 + r_s \tag{3.4b}$$

$$L_{zz}^0 = (1 + r_p)\sin\theta\left(\frac{N_1}{N'}\right)^2. \tag{3.4c}$$

Likewise, the ratio of the local fields at $z = d$ (at the film–ambient/environmental interface) to the incident fields may be obtained from

$$\begin{bmatrix} E_x \\ E_y \\ E_z \end{bmatrix}_{z=d} = \begin{bmatrix} L_{xx}^d & 0 & 0 \\ 0 & L_{yy}^d & 0 \\ 0 & 0 & L_{zz}^d \end{bmatrix} \begin{bmatrix} E_p \\ E_s \\ E_p \end{bmatrix}_{z=-\infty} \tag{3.5}$$

with

$$L_{xx}^d = \left(1 - r_\mathrm{p}\right)\cos\theta\cos\beta_2 + i\frac{N_1\cos\theta_2}{N_2}\left(1 + r_\mathrm{p}\right)\sin\beta_2 \tag{3.6a}$$

$$L_{yy}^d = \left(1 + r_\mathrm{s}\right)\cos\beta_2 + i\frac{N_1\cos\theta}{N_2\cos\theta_2}\left(1 - r_\mathrm{s}\right)\sin\beta_2 \tag{3.6b}$$

$$L_{zz}^d = \left[\frac{N_1^2}{N_2^2}\sin\theta\left(1 + r_\mathrm{p}\right)\cos\beta_2 + i\frac{N_1\sin\theta\cos\theta}{N_2\cos\theta_2}\left(1 - r_\mathrm{p}\right)\sin\beta_2\right]\left(\frac{N_2}{N''}\right)^2. \tag{3.6c}$$

Here N' and N'' are the interfacial refractive indices at the each interface. Note that the incorporation of N' and N'' is a convenience, as the same result could be obtained by including additional explicit nanoscale layers for specific interfacial features. When such features have corresponding $d' \ll \lambda$ and $d'' \ll \lambda$, the solution converges to the above presentation.

3.3 Methods

A 12.5 mm radius IR-grade fused silica hemicylindrical prism (Quartz Plus, Brookline, NH) was first cleaned with piranha solution to remove any organic residue, washed several times with 18.2 MΩ·cm deionized water, and then dried in an oven for 1 h. The flat square (25 mm × 25 mm) surface of the prism was then exposed to a solution of n-octadecyltrichlorosilane (OTS) (2 mM OTS in toluene) for 1 h prior to washing with toluene (3 × 10 mL) and methanol (3 × 10 mL) to remove any physisorbed OTS.[118] The OTS-functionalized hemicylinders were then placed in oven at 100 °C for 1 h. Poly(dimethyl siloxane) (PDMS) solution was prepared from a Sylgard 184 silicone elastomer kit (Dow Corning). The PDMS base (part A) and the curing agent (part B) were dissolved in chloroform (5 % w/w) and then mixed in a ratio of 10:1 (A:B). The polymer was then cast onto the OTS-functionalized surface of the silica prism using a custom chuck to enable spinning at 4000 rpm. Although dove prisms are easier to spin coat on account of their two parallel flat surfaces, hemicylinders or hemispheres enable a wide range of incident angles to be used. The PDMS-coated OTS-functionalized hemicylinders were then immediately baked in an oven at 85 °C under vacuum for 4 h. The film thickness was determined to be 370 ± 20 nm through a combination of profilometry and Raman spectroscopy as described in detail in Ref. 33. SFG spectra were collected using a 10 Hz scanning system (Ekspla) configured for computer-controlled variable angle of incidence[33, 119] achieved by rotating the sample and detector arm about a common axis that coincides with the point of overlap of the incoming visible (100 mJ/pulse) and IR (300 mJ/pulse) beams as shown in Figure 3.1. The incident beam geometry is fixed on the table such that $\theta_{\text{IR}} = \theta_{\text{vis}} + 9.8°$.

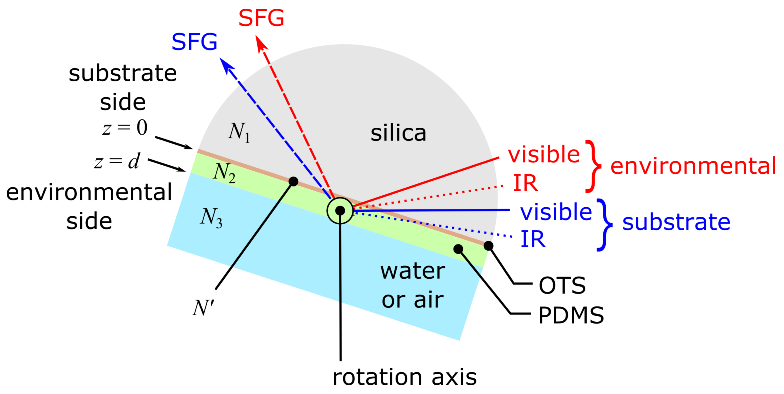

Figure 3.1: Top view of hemicylindrical prism functionalized with OTS and then coated with PDMS pressed into a liquid cell to create the silica–OTS–PDMS–water system. Two sets of beam angles are illustrated. The set with $\theta_{\text{vis}} = 68°$ (red) is selective to the environmental (air or water) side of the film, while that with $\theta_{\text{vis}} = 75°$ (blue) probes the substrate (silica/OTS) side of the film. Computer control of the sample and detector arm rotation about the common axis as indicated facilitates switching between these sets of angles. Reprinted with permission from Ref. 120. Copyright 2021 American Chemical Society.

3.4 Results and Discussion

In our previous work,[33] we have illustrated that we can design an experiment with a film thickness and combination of beam angles to tune the ratio of the L factors to selectively probe either film interface for the SSP polarization scheme. We also demonstrated a method for visualizing the experimental configuration space by plotting the ratio of $|L^0_{yy}L^0_{yy}L^0_{zz}|^2/|L^d_{yy}L^d_{yy}L^d_{zz}|^2$ against the film thickness and angle of incidence using coarse contour levels corresponding to regions of interest. In the current multi-polarization demonstration, we use a PDMS film on OTS-treated silica adjacent to water as the model system to study the interface selectivity. We can test the environmental side specificity through the suppression of OTS signals, and test the substrate side specificity through suppression of the water O–H stretching spectrum. In a more practical application, neither water or OTS are required, and the goal may be to distinguish PDMS signals from either side of the polymer interface. Since the angle between our visible and IR beams is fixed, for simplicity we refer to the angles of incidence by θ_{vis} with the understanding that θ_{IR} is 9.8° higher.

Most samples studied by SFG spectroscopy have $C_{\infty v}$ symmetry. That is, molecules are randomly oriented in the plane of the surface, and the inversion symmetry is broken along only the surface normal $\pm z$. In such cases, a tilt angle preference actually describes a cone of tilt angles. Under this symmetry, there are four non-zero polarization schemes that can be configured from the eight possible combinations of s- and p-states of each of the three beams. These are SSP (SFG, visible, infrared), SPS, PSS, and PPP.

3.4.1 SSP, SPS, and PSS polarizations

Of the four polarization schemes mentioned above, SSP, SPS, and PSS are special as, under $C_{\infty v}$ symmetry, they probe only a single element of the $\chi^{(2)}$ tensor and therefore no separation is required using additional experiments such as those at multiple combinations of beam angles.[119,121] Here the intensity is given in a straightforward manner as the interference between contributions from the $z = 0$ and $z = d$ interfaces.

$$\begin{aligned} I_{\mathrm{SFG}} &\propto \left| L^0_{ii} L^0_{jj} L^0_{kk} \chi^{(2),0}_{ijk} + L^d_{ii} L^d_{jj} L^d_{kk} \chi^{(2),d}_{ijk} \right|^2 \\ &= \left| L^0_{ii} L^0_{jj} L^0_{kk} \chi^{(2),0}_{ijk} \right|^2 + \left| L^d_{ii} L^d_{jj} L^d_{kk} \chi^{(2),d}_{ijk} \right|^2 + 2 \left| L^0_{ii} L^0_{jj} L^0_{kk} \chi^{(2),0}_{ijk} \right| \cdot \left| L^d_{ii} L^d_{jj} L^d_{kk} \chi^{(2),d}_{ijk} \right| \cos(\Delta\phi) \end{aligned} \tag{3.7}$$

where $\chi^{(2),0}$ and $\chi^{(2),d}$ represents the second order susceptibility at the respective interface, i, j, k are placeholders for the Cartesian coordinates x, y or z according to the polarization of the beams, and $\Delta\phi$ is the phase difference between the contributions from each interface. A key point is that to selectively probe one interface, the local field factor must be *significantly* larger on the targeted side. This is because the design of experiments typically doesn't consider the (often unknown) relative magnitude of $\chi^{(2),0}$ and $\chi^{(2),d}$, and yet this consideration is as important as the ratio of the magnitudes of the L factors. In the ideal cases, the L factors of the desired interface are so dominant, that if the $\chi^{(2)}$ contributions can be assumed (or known) to be comparable, interfacial selectivity can be judged on the bases of the local field enhancement/suppression alone. This is shown for the silica–OTS–PDMS–water system at 2910 cm^{-1} in SSP in Figure 3.2a and SPS (with a very similar solution for PSS in our case, since our geometry is close to colinear) in Figure 3.2b. When the goal is to probe the PDMS–water inteface, the best combination of thickness and angle is indicated in the red regions with $|L^d_{ii} L^d_{jj} L^d_{kk}|^2 / |L^0_{ii} L^0_{jj} L^0_{kk}|^2 > 100$, where i,j,k are determined depending on whether SSP (yyz), SPS (yzy) or PSS (zyy) are of interest. Possibly acceptable but less suitable configurations are shaded yellow ($10 < |L^d_{ii} L^d_{jj} L^d_{kk}|^2 / |L^0_{ii} L^0_{jj} L^0_{kk}|^2 < 100$). If the PDMS–glass/OTS interface is targeted, the experiment should be set in a dark blue region so that $|L^0_{ii} L^0_{jj} L^0_{kk}|^2 / |L^d_{ii} L^d_{jj} L^d_{kk}|^2 > 100$. A potential compromise would be the light blue regions, but these should be used cautiously as the selectivity is not as high ($10 < |L^0_{ii} L^0_{jj} L^0_{kk}|^2 / |L^d_{ii} L^d_{jj} L^d_{kk}|^2 < 100$). White regions have no selectivity as the ratio of L factors is less than 10 in either direction.

We emphasize that, even with a selectivity ratio of 100, cross terms from $\chi^{(2)}$ elements at the two interfaces may contribute to the measured signal, depending on the relative

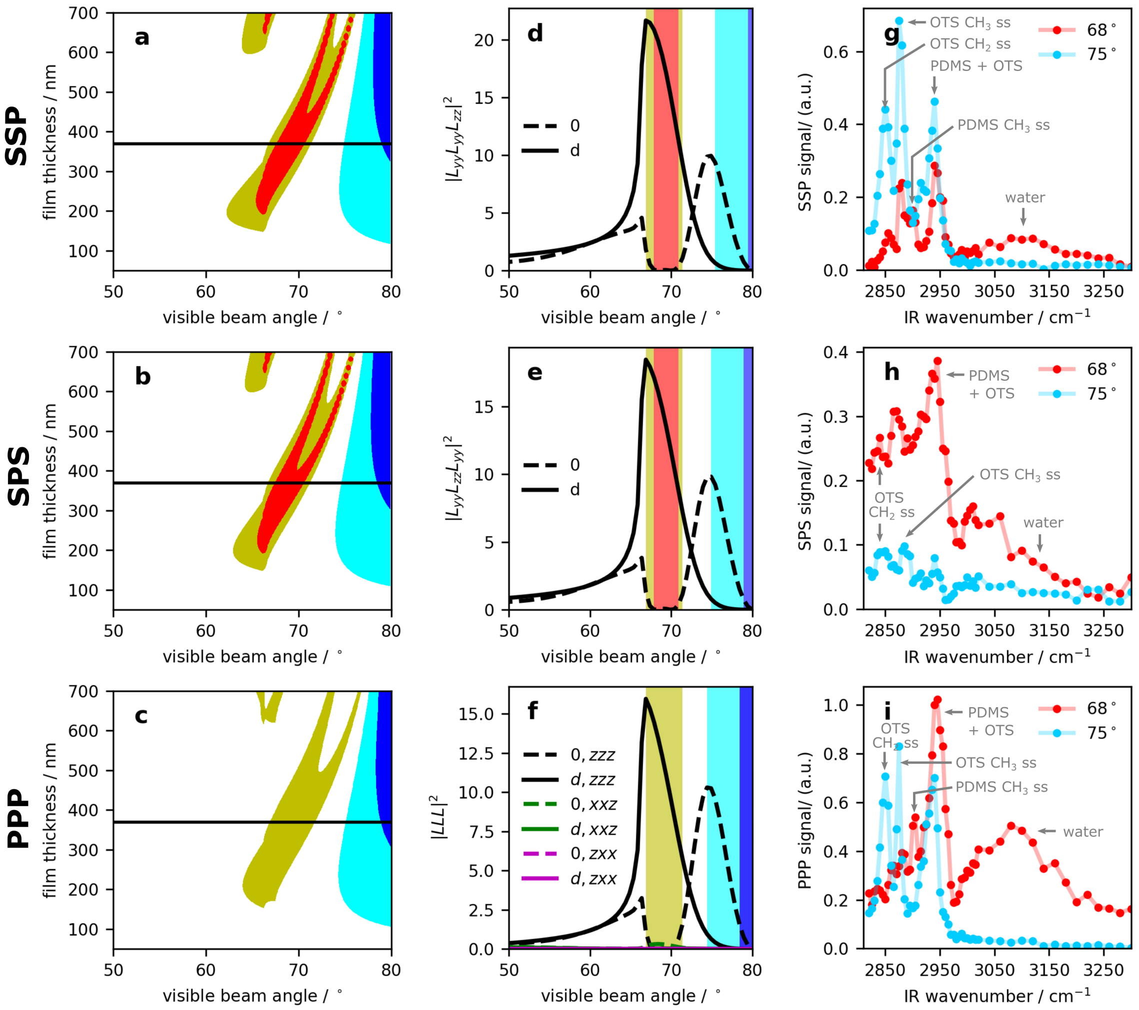

Figure 3.2: The left column displays maps of ratio of the $|L_{ii}L_{jj}L_{kk}|^2$ factors for each side of the film ($z = d/z = 0$) plotted against the film thickness and angle of incidence for the silica–OTS–PDMS–water system at 2910 cm^{-1} for (a) SSP, (b) SPS and (c) PPP polarization schemes. Yellow indicates good, and red indicates even better selectivity for the water side (see text for details). Light blue indicates good, and dark blue better, selectivity for the substrate side. White regions have no selectivity. The center column (d, e, f) shows corresponding slices of these maps for a PDMS film thickness of 370 nm. Here the solid lines are $|L^d_{ii}L^d_{jj}L^d_{kk}|^2$ on the exposed sides, and the dashed lines represent those for the substrate side, $|L^0_{ii}L^0_{jj}L^0_{kk}|^2$. In panel (f) the zxx curve represents the combined $|L_{ii}L_{jj}L_{kk}|^2$ factor that incorporates both zxx and xzx terms (see Eq. 3.9). The right column (g, h, i) displays experimental data with predicted selectivity to PDMS–water at 68° and PDMS–silica/OTS at 75° for all three polarization combinations. Reprinted with permission from Ref. 120. Copyright 2021 American Chemical Society.

magnitude and phase of the $\chi^{(2)}$ components at each interface. For this reason, one should set the boundaries of the contour colors to be at the largest possible values. For example, if the polymer–water interface is targeted, and there are large red regions (selectivity greater than 100), the existence of additional contours (such as those greater than 1000) should be explored. Another point to note is that the maps need to be constructed for a single set of IR, visible, and SFG wavelengths. The results are not very sensitive to changes on the order of ± 500 cm^{-1}, but care should be taken when collecting spectra in more separated spectral regions, i.e. fingerprint vs high frequency CH/OH stretching.

One can also plot a slice of the 2D-map along the angle dimension as shown in Figure 3.2d (SSP) and 2e (SPS) with the solid black lines corresponding to the buried interface, and dashed lines for the environmental (water) interface. The same color regions are overlaid on the graphs for reference. Although this representation enables inspection for only a single film thickness, it has an advantage in that the absolute scale of $|L^0_{ii}L^0_{jj}L^0_{kk}|^2$ and $|L^d_{ii}L^d_{jj}L^d_{kk}|^2$ are displayed rather than their ratio. This ensures that sufficient signal may be obtained, provided that $|\chi^{(2)}|$ for the interface of interest is large enough. In other words, it is important to rule out regions (beam angles) for which the selectivity may be high, but the targeted $|L_{ii}L_{jj}L_{kk}|^2$ is too small and so suppresses the SFG signal considerably.

In our experimental demonstration, we have determined the PDMS film thickness to be 370 nm, indicated by the horizontal lines in Figure 3.2a and 2b, and corresponding slides in panels 2d and 2e. Inspecting the overall appearance of the maps, one notices the strong dependence on both film thickness and angle of incidence. For this reason, it is important to know the film thickness with accuracy, and in a manner that is convenient to obtain quickly without damaging or contaminating the surface.[33] In this case, our determined film thickness suggests that setting θ_{vis} somewhere in the range of 68–71° predicts specificity for the PDMS–water interface (red region) for both SSP and SPS. Likewise, setting the incident angle above 75° predicts specificity for the PDMS–glass interface (blue region). Ideally, when the experiment is selective to the buried side, CH_3 stretching modes (2875 cm^{-1} and

2940 cm^{-1}) and CH$_2$ stretching modes (2850 cm^{-1}) from OTS should be prominent while the water signal (3000–3400 cm^{-1}) would be absent. When the experiment is selective to the environmental side, OTS signal would disappear and water OH stretching should be visible. At 68°, we observe that water signal is present in both SSP (Figure 3.2g) and SPS spectra (Figure 3.2h), but very low water OH stretching can be observed at 75° in either polarization scheme in agreement with our model. Interpreting the CH-stretching region, PDMS modes (2910 cm^{-1} and 2960 cm^{-1}) can be observed at all angles. OTS modes are prominent at 75° but still visible, albeit with lower intensity, at 68°. It is possible that OTS signals are not completely suppressed due to the large $\chi^{(2)}$ for the OTS modes in comparison to the ratio of the L factors. If the goal of the experiment were to probe PDMS at the PDMS–water interface and $|\chi_{yyz}^{(2),0}|$ was not significantly larger than $|\chi_{yyz}^{(2),d}|$, the desired interface selectivity may still be achieved. In some cases it may be possible to determine the relative magnitudes of the $\chi^{(2)}$ terms in advance, from separate experiments. As a reminder, in cases where $\chi^{(2)}$ of both species contribute, it is not enough to know their relative magnitudes in order to model and predict the interference, as their relative phase also plays a crucial role in the intensity.[51, 122]

To further investigate the appearance of OTS modes in the predicted red regions of Figure 3.2 for SSP and SPS, we switch to another system, removing the water to create the silica–OTS–PDMS–air interfaces. Predicted selectivity as a function of angle and thickness, along with measured spectra are shown in Figure 3.3. In this case, the PDMS–glass selectivity is predicted to occur at a visible beam angle of 43°. The SSP spectrum of PDMS–air at 43° is presented in Figure 3.3g, and SPS in Figure 3.3h. Here PDMS modes are prominent and no OTS modes can be observed. For SSP we have calculated that the value of $|L_{yy}^{d}L_{yy}^{d}L_{zz}^{d}|^2/|L_{yy}^{0}L_{yy}^{0}L_{zz}^{0}|^2$ for the PDMS–air system at 43° is 1132, while it for the PDMS/water system at 68° is 129. Even though they are all over the threshold of 100 to be considered as selective to the environmental side (our definition of red), the difference in the amplitude of the cross-term and the residue signal from the buried side is significant, especially when $|\chi^{(2)}|$ on the buried side is large. For SPS, the $|L^d_{yy}L^d_{zz}L^d_{yy}|^2/|L^0_{yy}L^0_{zz}L^0_{yy}|^2$ ratio for the PDMS–air system at 43° is 61516, and that of the PDMS/water system at 68° is 1109. This difference results in more than 8 times larger $|L^0_{yy}L^0_{zz}L^0_{yy}|^2$ term for PDMS–water than PDMS–air for SSP polarization, and 55 times more selective in SPS. This results in a cross term up to 3 times larger for SSP and up to 7 times larger for SPS.

3.4.2 PPP polarization

We now shift our discussion to focus on PPP polarization. Compared to the previous cases presented, PPP is more complicated as it probes a linear combination of $\chi^{(2)}$ elements. In keeping with our example of azimuthally-isotropic ($C_{\infty v}$) surfaces, the effective susceptibility can be expressed as

$$\begin{aligned}\chi^{(2)}_{\mathrm{eff,PPP}} = & -L_{xx}L_{xx}L_{zz}\chi^{(2)}_{xxz} - L_{xx}L_{zz}L_{xx}\chi^{(2)}_{xzx} \\ & + L_{zz}L_{xx}L_{xx}\chi^{(2)}_{zxx} + L_{zz}L_{zz}L_{zz}\chi^{(2)}_{zzz}.\end{aligned} \tag{3.8}$$

In the most commonly-encountered scenarios, the visible and SFG beams are far from an electronic resonance, and so the Raman tensor is symmetric. This results in $\chi^{(2)}_{xzx} = \chi^{(2)}_{zxx}$. Applying this simplification and considering that signal can come from two interfaces with $\chi^{(2),0} \neq 0$ and $\chi^{(2),d} \neq 0$ results in

$$\begin{aligned}I_{\mathrm{PPP}} \propto \Big| & - L^0_{xx}L^0_{xx}L^0_{zz}\chi^{(2),0}_{xxz} + (L^0_{zz}L^0_{xx}L^0_{xx} - L^0_{xx}L^0_{zz}L^0_{xx})\chi^{(2),0}_{zxx/xzx} + L^0_{zz}L^0_{zz}L^0_{zz}\chi^{(2),0}_{zzz} \\ & - L^d_{xx}L^d_{xx}L^d_{zz}\chi^{(2),d}_{xxz} + (L^d_{zz}L^d_{xx}L^d_{xx} - L^d_{xx}L^d_{zz}L^d_{xx})\chi^{(2),d}_{zxx/xzx} + L^d_{zz}L^d_{zz}L^d_{zz}\chi^{(2),d}_{zzz}\Big|^2.\end{aligned} \tag{3.9}$$

To investigate whether the PPP signal has a chance of interface selectivity for any combination of thickness and beam angles, the first approach is to check whether all products of L factors are sufficiently large for the interface of interest. To be explicit, if one wishes to study the water side of the film and *all* of following are satisfied:

$$|L^d_{xx}L^d_{xx}L^d_{zz}|^2 \gg |L^0_{xx}L^0_{xx}L^0_{zz}|^2 \tag{3.10a}$$

$$|L^d_{zz}L^d_{zz}L^d_{zz}|^2 \gg |L^0_{zz}L^0_{zz}L^0_{zz}|^2 \tag{3.10b}$$

$$|L^d_{zz}L^d_{xx}L^d_{xx} - L^d_{xx}L^d_{zz}L^d_{xx}| \gg |L^0_{zz}L^0_{xx}L^0_{xx} - L^0_{xx}L^0_{zz}L^0_{xx}|^2 \tag{3.10c}$$

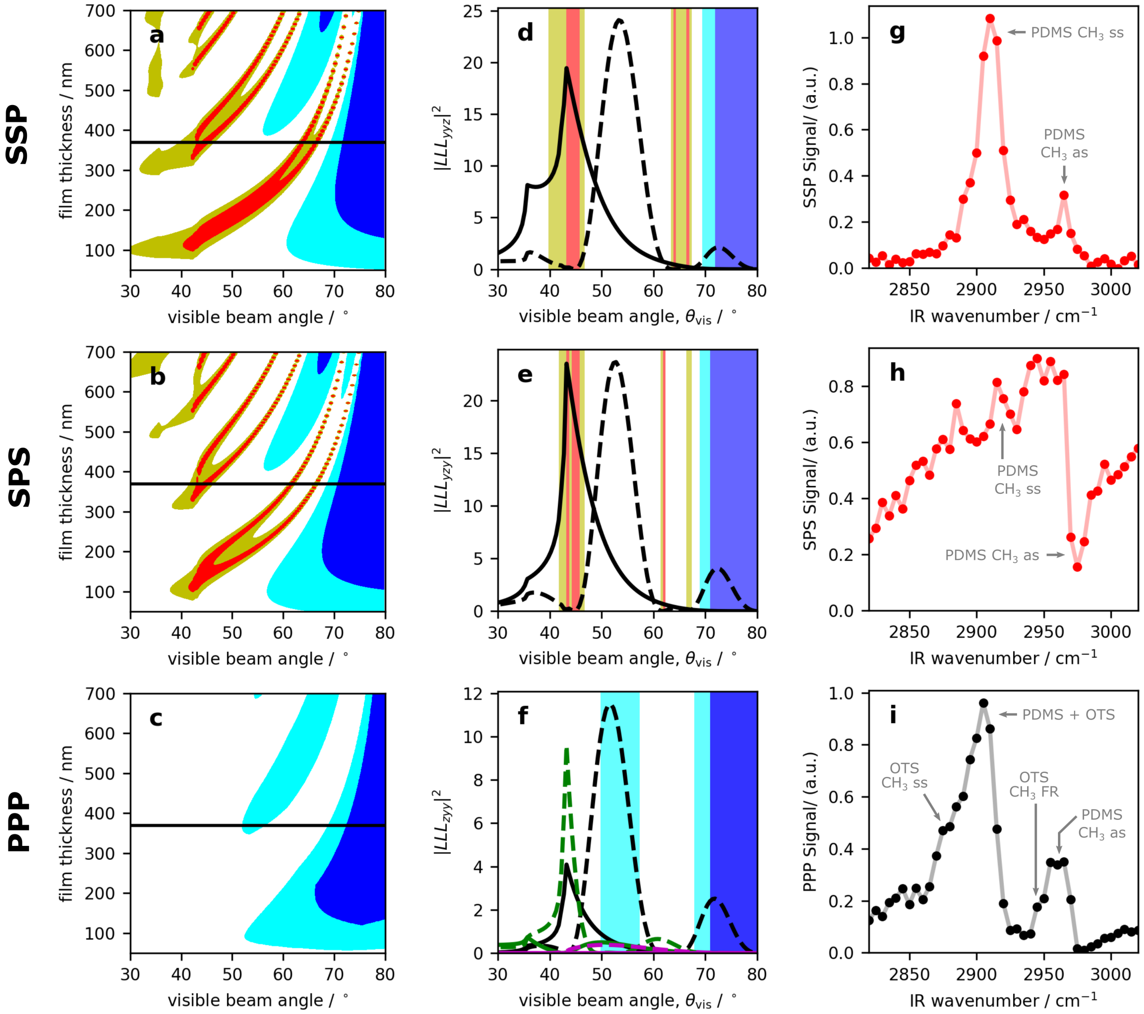

Figure 3.3: Ratio maps (a, b, c), slices at a film thickness of 370 nm (d, e, f), and experimental results (g, h, i) for the silica–OTS–PDMS–air interface at 2910 cm^{-1}. See Figure 3.2 for a description of the colours and lines. All experimental data for this system was collected at $\theta_{\text{vis}} = 43°$. Reprinted with permission from Ref. 120. Copyright 2021 American Chemical Society.

then PDMS–water selectivity exists independent of the magnitude and phase of the corresponding $\chi^{(2)}_{ijk}$ contributions. Similarly, if the following were satisfied simultaneously

$$|L^0_{xx}L^0_{xx}L^0_{zz}|^2 \gg |L^d_{xx}L^d_{xx}L^d_{zz}|^2 \tag{3.11a}$$

$$|L^0_{zz}L^0_{zz}L^0_{zz}|^2 \gg |L^d_{zz}L^d_{zz}L^d_{zz}|^2 \tag{3.11b}$$

$$|L^0_{zz}L^0_{xx}L^0_{xx} - L^0_{xx}L^0_{zz}L^0_{xx}|^2 \gg |L^d_{zz}L^d_{xx}L^d_{xx} - L^d_{xx}L^d_{zz}L^d_{xx}|^2 \tag{3.11c}$$

the selectivity will be towards the buried side. A graphical solution to Eqs. 3.10 and 3.11 is shown in Figure 3.4 where each colored region represents the film thickness and angle of incidence combination that has selectivity to the water or substrate side for the corresponding local field tensor element. Upon examining the resulting plot, there is no combination that provides specificity to the exposed side for all three components, and there is no region where the solutions overlap to simultaneously satisfy all expressions in Eqs. 3.11 for the buried side. We note that, although this was the case of the silica–OTS–PDMS–water system, it does not mean that a general PPP solution does not exist for other systems. Researchers should implement the formalism we have presented for their system if the materials of interest differ substantially in terms of their refractive indices, for example when using metal substrates.

However this does not mean it is impossible to interpret the results of a PPP spectrum with interface selectivity, merely because a global L-dominant solution does not exist. One should next consider if one set of L factors is higher than all others to effectively make a single element of the hyperpolarizability dominant the PPP response.[106] Here we have found that this is exactly the case for $L_{zz}L_{zz}L_{zz}$; the result is shown in Figure 3.2c for all combinations of film thickness and beam angles, with the corresponding slice at $d = 370$ nm in Figure 3.2f. Here white still indicates no selectivity, but the colored regions now highlight selectivity of $|L^0_{zz}L^0_{zz}L^0_{zz}|^2$ or $|L^d_{zz}L^d_{zz}L^d_{zz}|^2$ with respect to all other L factors that contribute to PPP. Although there is no region (red by our definition) where $|L^d_{zz}L^d_{zz}L^d_{zz}|^2$ is over 100 times larger than all other sets of L factors on the buried side,

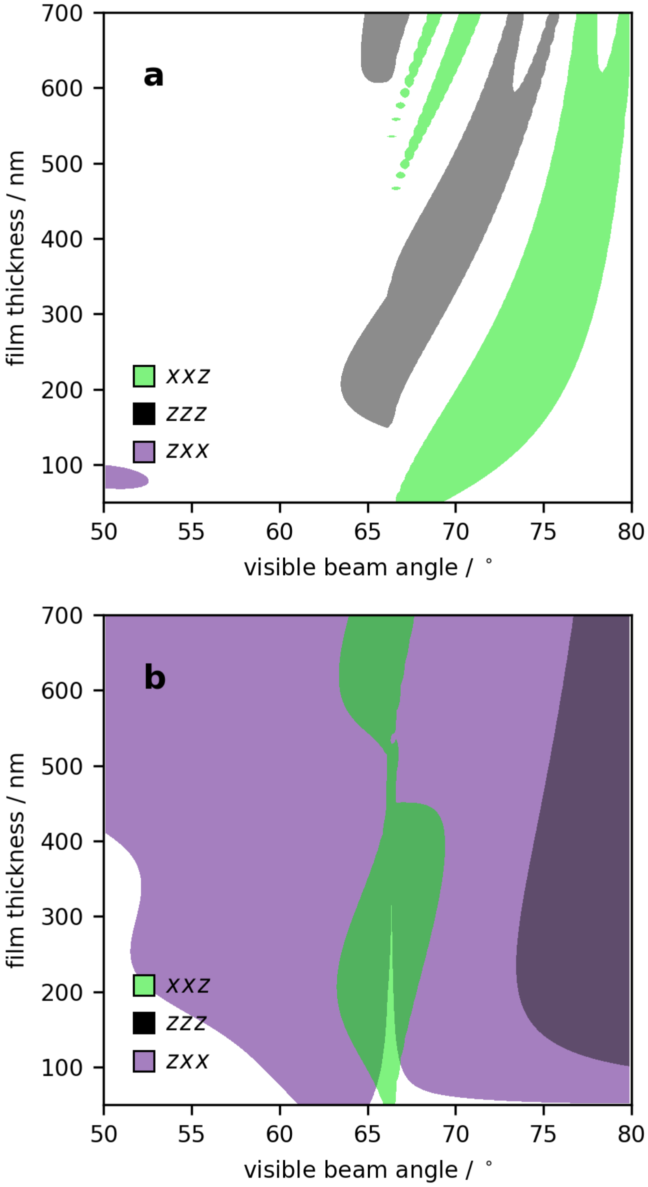

Figure 3.4: A selectivity map for L factor elements participating in PPP polarization for the silica–OTS–PDMS–water system at 2910 cm^{-1}. Each color coded region corresponds to a thickness and angle combination that provides selectivity to (a) the environmental side ($|L^d_{ii}L^d_{jj}L^d_{kk}|^2 \gg |L^0_{ii}L^0_{jj}L^0_{kk}|^2$) or (b) the substrate side ($|L^0_{ii}L^0_{jj}L^0_{kk}|^2 \gg |L^d_{ii}L^d_{jj}L^d_{kk}|^2$) for the indicated combination of L factor tensor elements. Reprinted with permission from Ref. 120. Copyright 2021 American Chemical Society.

regions of intermediate selectivity (yellow) do exist. All of the usual caution comes along with measurements in yellow (or light blue) regions—since the ratio of L factors is not excessively large, multiplying by the respective $\chi^{(2)}$ elements can enhance or reduce the interface selectivity.

As shown in Figure 3.2f, for a film with a thickness of 370 nm in the silica–OTS–PDMS–water system, $|L^d_{zz}L^d_{zz}L^d_{zz}|^2$ is dominant in the region 67–70°, while $|L^0_{zz}L^0_{zz}L^0_{zz}|^2$ is dominant when the incident angle is larger than or equal to 75°. PPP spectra with visible incident angles of 68° and 75° are shown in Figure 3.2i. At 68°, water OH-stretching bands are observed; at 75° the water modes disappear as predicted by the model. When we look at the CH stretching region, PDMS modes are visible at both angles, while the OTS modes are prominent at 75°. However, the OTS signal is still observed at 68°. Recall that the predicted selectivity was in the yellow region, so a large magnitude of $\chi^{(2)}_{\mathrm{OTS}}$ would compromise the selectivity as discussed for SSP and SPS. As for the PDMS–air interface, according to our calculation at 43° angle of incidence, there is no predicted selectivity. The corresponding experimental spectrum (Figure 3.3i) is plotted in black to highlight that it does not feature environmental (red) or substrate (blue) selectivity, and clearly features prominent OTS bands.

In summary, the steps required to carry out experiments that maximize the selectivity for a particular interface under SSP, SPS, or PSS polarization are:

1. Have knowledge of the complex refractive index of all phases at all wavelengths of interest;
2. Generate thickness-angle maps to see if sufficient selectivity can be achieved based on local field considerations alone;
3. Prepare a film of a target thickness based on the predictions;
4. Measure the actual thickness, and fine tune the angle of incidence according to the measured thickness.

In the case of PPP experiments, as there are multiple $\chi^{(2)}$ tensor elements contributing to the signal, one approach is to follow the first two steps of the above procedure for each element, and determine if there is a thickness and angle combination that has dominant local fields at the surface of interest for all elements. Alternatively, or if there is no solution based on that approach, the magnitude of individual local field factors may be compared to see if the contribution of any elements can be ignored. The procedure then continues with step 3 in the method.

3.5 Conclusions

Tuning the angle of incidence with knowledge of the film thickness offers the possibility of selectively probing either side of a thin film through enhancement/suppression of the corresponding local fields. We have described a method that enables evaluation of the anticipated performance in multiple beam polarizations. Our experimental results show that, although the general trends agree with predictions, achieving selectivity based on local fields alone sometimes requires an enhancement factor beyond what is achievable for all systems in all polarization schemes. This ultimately comes down to the relative magnitude and phase of the nonlinear susceptibility at each interface. However, even in cases where perfect selectivity is not attainable, this method enables significant improvement in isolation of signals from the interface of interest.

Chapter 4

Temperature-Dependent Chemical Functional Group Reorientation at Silicone Surfaces[*],[†]

4.1 Introduction

Silicone materials such as PDMS have a broad range of industrial and scientific applications ranging from insulators for overhead power distribution, water-repellent sealants, and materials for microfluidic devices.[123,124] Silicone insulators are important alternatives to traditional glass or ceramic devices on account of their lighter weight, better mechanical properties, high resistance to contamination, and prolonged hydrophobicity.[125–127] In addition to their electrical, mechanical, and environmental resilience,[128] performance over a wide range of temperatures is also critical. Sunlight heating has been shown to degrade the performance of high voltage silicone insulators, particularly in arid climates.[129] For this application, and in the case of silicone sealants, there is considerable interest in understanding the surface properties that can account for hydrophobicity in the temperature range −30 °C to 60 °C.[130] Properties such as surface tension and surface roughness are important parameters in predicting adhesion of elastomers, and have been shown to

---

[*] Reproduced in part from Cai, C.; Azam, M. S.; Hore, D. K. "Temperature-Dependent Chemical Functional Group Reorientation at Silicone Surfaces." *J. Phys. Chem. C* under review.

[†] All data collection, including preparation of polymer surfaces and solutions, and measurement of SFG spectra performed by Azam. Treatment of data, model development, and analysis of data done by Cai. Cai, Azam, and Hore contributed to the discussion of the results, and to the writing of the manuscript.

depend strongly on the temperature.[131] In microfluidics applications, PDMS is often used to produce the chip, as well as spin-coated onto substrates to form the floor of the channel. The motion of droplets can be thermally controlled in droplet-based microfluidics, within an operational range typically between 20–60 °C.[132–134] In addition, droplets or bubbles conveying solutes, materials or particles can be transported in a microcavity by applying a temperature gradient.[135, 136] In all of the above applications, there is an interplay between the interfacial structure of liquids such as aqueous drops, molecules adsorbed at the polymer surface, and the surface structure of the polymer itself. Examining the polymer surface as a function of temperature using a surface-specific technique is therefore important to understand this relationship.

Vibrational spectroscopy offers a label-free probe of chemical structure as the vibrational resonances of individual functional groups can be used to assess the orientation of different parts of a molecule. In surface studies, the challenge is to have sufficient specificity to molecules at the interface, so as to include signals from the same molecules in adjacent bulk phases. For this aim, second-order nonlinear optical probes such as visible-infrared sum-frequency generation (SFG) offer an extreme surface specificity, as signals arise only from regions where the bulk inversion symmetry is broken.[29, 30, 36] Unlike techniques such as evanescent-wave IR spectroscopy, SFG does not rely on shallow penetration of the probe beams to exclude bulk signals. Vibrational SFG spectroscopy has already been recognized as a premier method for investigating the surface structure of polymers,[31, 50, 109, 137–145] including PDMS.[85, 86, 86, 114, 146–149] By performing an orientation analysis through the use of multiple SFG beam polarizations, the average orientation and angular distribution of the methyl groups at the PDMS surface has been studied for the PDMS–air and PDMS–water interfaces.[82] There has also been considerable interest in investigating changes to the PDMS surface functional groups when the environment is changed.[82]

In this work, we use SFG spectroscopy to study the temperature dependence of the

PDMS surface structure in contact with water and a superhydrophobic liquid. We use our recently developed technique of manipulating the polymer film thickness and angle of incidence to selectively probe the PDMS–liquid interfaces using two different beam polarization schemes.[33, 120] The resulting data is analyzed to propose structures of the PDMS surface at different temperatures. The analysis also demonstrates a new technique in the quantitative treatment of SFG spectral data, where ratios of peak amplitudes are used in conjunction with the temperature-dependence of the amplitudes in order to provide additional information.

4.2 Methods

4.2.1 Experimental

A detailed description of the preparation of the PDMS thin films on IR-grade fused silica hemicylindrical prisms was described in a previous report.[33] In brief, the hemicylinders were first cleaned with piranha (3:1 mixture of H_2SO_4 and 30% H_2O_2), washed with 18.2 MΩ·cm deionized water, and then dried in oven at 100 °C for 1 h under vacuum. The flat square (25 mm × 25 mm) surface of was then spin-coated with PDMS solution prepared from a Sylgard 184 silicone elastomer kit (Dow Corning). PDMS base (part A) and curing agent (part B) were dissolved in spectral grade chloroform and mixed in a ratio of 10:1 (A:B) to obtain 5% (w/w) PDMS solution. This freshly prepared PDMS solution ($\approx$ 0.25 mL) was then placed on the flat surface of the cleaned prisms secured in a custom chuck that was particularly adapted for our spin-coater (Specialty Coating Systems, Inc. IN, USA), enabling casting onto hemicylinders at 4000 rpm for 5 min. Next, the PDMS-coated prisms were cured at 85 °C for 4 h under vacuum. The thickness of the as-prepared films were measured by a Raman spectroscopy method that was developed to avoid contact or prolonged exposure of the film surface.[33]

The laser system used for SFG spectroscopy has been described previously.[70] Briefly, 30 ps pulses with a repetition rate of 10 Hz at 1064 nm (fundamental) and 532 nm (second harmonic) are generated from a Nd:YAG laser (Ekspla PL2241A). These two beams are used to pump an optical parametric generator (Ekspla PG501) to produce tunable IR frequencies in the range of 2800–3000 cm^{-1}. The IR beam (diameter 0.6 mm, energy $\approx$ 300 μJ/pulse) and a portion of the visible output (diameter at the sample 0.6 mm, energy 100 μJ/pulse) are then incident on the PDMS-coated flat surface of a hemicylindrical prism pressed against a custom Teflon cell[70] containing a 10 mL reservoir volume with a fluoropolymer O-ring (Marco Rubber, NH). The cell is mounted on two concentric motor-controlled rotation stages that enable the sample and detector to be rotated to achieve control over the angle of incidence. Angles ($\theta_{\text{vis}} = 66^\circ$ and $\theta_{\text{IR}} = 76^\circ$ for FC40, and $\theta_{\text{vis}} = 69^\circ$ and $\theta_{\text{IR}} = 79^\circ$ for D_2O) have been chosen to selectively probe the PDMS-liquid interface by consideration of the local field effects together the the measured film thickness.[33,120]

The liquid reservoir was filled with either spectral grade D_2O (Sigma-Aldrich, USA) or the perfluorinated liquid FC40 (Sigma–Aldrich, USA). D_2O was used in place of H_2O for a more facile analysis of the PDMS methyl modes without interference from O–H stretching. There are many relevant hydrophobic environments of interest, including air; FC40 was chosen in order to provide better thermal conduction to the interface. The temperature of the liquid was controlled by employing a cooling and heating circulator (PolyScience 9112) channelled through the aluminum block as described in our previous report.[150] The SFG beam generated from the PDMS–liquid interface was then collected as an average of 50 laser shots while tuning the IR frequency in 5 cm^{-1} steps. The experiments were conducted in two polarization combinations, SSP (s-polarized SFG, s-polarized visible, and p-polarized IR) and SPS. For orientation analyses, PPP polarization is often used as it can provide access to an additional degree of freedom in the parameterization of an orientation distribution function.[151,152] However, PPP was not used here as we have demonstrated that it does not exhibit sufficient selectivity for the PDMS–solution interface.[120]

4.2.2 SFG data analysis

The recorded SFG signal can be expressed as

$$I_i^{\mathrm{SFG}} \propto |L_{ii} L_{jj} L_{kk} \chi_{ijk}^{(2)}|^2 I_j^{\mathrm{IR}} I_k^{\mathrm{vis}} \tag{4.1}$$

where L are the local field factors, I^{IR} and I^{vis} represent the intensity of the input beams, and i, j, k are Cartesian coordinates in the laboratory frame. The temperature-dependent refractive indices were used to calculate the local field factors $|L_{ii} L_{jj} L_{kk}|^2$ as described in previous publications.[33,120] Wavelength- and temperature-dependent (real part of the) refractive index of D_2O were taken from the literature.[153,154]

$$n(\lambda, t) = A + B/\lambda^2 + C \cdot T + D \cdot T/\lambda^2 + E \cdot T^2 + F \cdot T^3 \tag{4.2}$$

where A, B, C, D, E, and F are the Cauchy coefficients

$$A = 1.0244 \tag{4.3a}$$

$$B = 3329.2 \tag{4.3b}$$

$$C = 2.6048 \times 10^{-3} \tag{4.3c}$$

$$D = -1.630 \tag{4.3d}$$

$$E = -7.248 \times 10^{-6} \tag{4.3e}$$

$$F = 6.15 \times 10^{-9} \tag{4.3f}$$

and λ is the wavelength in microns. The imaginary part of the D_2O refractive index was close to zero[155,156] ($\kappa = 2.98 \times 10^{-8}$ at 532 nm and similar at SFG wavelengths, $\kappa = 1.416 \times 10^{-3}$ at 3.33 μm) and therefore its temperature-dependence was not a significant source of spectral intensity variation.

The temperature-dependent refractive index of silica was incorporated in our model using the expression[157]

$$n^2 - 1 = \sum_{i=1}^{3} \frac{a_i}{b_i^2 - E^2} \tag{4.4}$$

with

$$a_i = a_{i0} + a_{i1}t + a_{i2}t^2 \tag{4.5a}$$

$$b_i = b_{i0} + b_{i1}t + b_{i2}t^2. \tag{4.5b}$$

where E is the photon energy in eV, and t is the temperature in degrees Celsius. Values of the parameters a_{in} and b_{in} can be found in the literature.[157]

Published values of temperature-dependent refractive index for PDMS are not available. Since for polymers the refractive index and density have a near linear relationship,[158] temperature-dependent density data[159] was used to estimate the change in refractive index under elevated temperatures. The room temperature complex refractive index data for PDMS was taken from the literature[160,161] and reduced by 5% over the range 20–70 °C.

Similarly, there is no published temperature-dependent refractive index data for FC40. The datasheet lists the room temperature refractive index in the visible as 1.29.[78] As there are no vibrational resonances in our frequency range of interest, we consider the dispersion to be negligible. The manufacturer (3M) provides an empirical relationship to estimate the density

$$\rho = 1909 - 2.16T \ \mathrm{kg \cdot m^{-3}} \tag{4.6}$$

where T is the temperature in degrees Celsius. Over our temperature range, the density decreases by 6%.

The frequency dependence of the nonlinear susceptibility $\chi^{(2)}$ can be described using a Lorentzian lineshape

$$\chi^{(2)}_{ijk}(\omega_{\mathrm{IR}}) = \chi^{(2)}_{\mathrm{NR},ijk} + \sum_q \frac{A_{q,ijk}}{\omega_{\mathrm{IR}} - \omega_q + \Gamma_q\sqrt{-1}} \tag{4.7}$$

where $\chi^{(2)}_{\mathrm{NR}}$ is a vibrationally non-resonant contribution, and each resonant term can be described with an amplitude A_q, width Γ_q, and resonance frequency ω_q. The measured response is related to the surface chemical function groups through the molecular hyperpolarizability $\alpha^{(2)}$. Since the individual molecular responses cannot be distinguished, we use an average over the surface molecular orientations

$$\chi_{ijk}^{(2)} = \frac{N}{\varepsilon_0} \langle \alpha^{(2)} \rangle \tag{4.8}$$

where N is the number of molecules, ε_0 is the vacuum permittivity, and the angular brackets indicate an orientation average. To proceed in the analysis, one therefore requires an $\alpha^{(2)}$ model of the PDMS local modes, the methyl stretching modes in the frequency region of interest. Such a model describing two methyl groups attached to a central atom was first developed for the isopropyl group[111] and later adapted to describe the plane of the two methyl groups for PDMS.[114] The basic idea is that the methyl groups connected to the Si atom have an angle of 112° between the two methyl C_3 axes. The tilt angle of the plane, θ, is defined as the angle between the surface normal (z) and the bisecting vector of the two C–Si bonds, noted as v. The twist angle (ψ, the rotation about v) is defined so that the C–Si–C plane is perpendicular to the surface plane when $\psi = 0°$, and the two methyl groups are equidistant from the surface when $\psi = 90°$. The azimuthal angle (ϕ, describing rotation about z) is assumed to be evenly distributed and so the amplitudes in Eq. 4.7 become

$$A_{ijk}(\theta, \psi) = \int_0^{2\pi} A_{ijk}(\theta, \phi, \psi)\, \mathrm{d}\phi. \tag{4.9}$$

The non-zero hyperpolarizability elements of each methyl group are $\alpha_{aac}^{(2)}$, $\alpha_{ccc}^{(2)}$, and $\alpha_{caa}^{(2)}$, and were determined to have a ratio of $\alpha_{aac}^{(2)} : \alpha_{ccc}^{(2)} : \alpha_{caa}^{(2)} = 2.3 : 1 : 2.3$ for PDMS.[82,114] After projecting into the laboratory frame, the Lorentzian amplitudes in Eq. 4.7 become

$$\begin{aligned} A_{yyz}(\theta, \psi) = {} & \frac{N}{2\varepsilon_0}(\alpha_{aac}^{(2)} - \alpha_{ccc}^{(2)})\{(\langle \cos\theta \rangle - \langle \cos^3\theta \rangle) \\ & \times [(5 + 3\langle \cos 2\psi \rangle)(\cos\gamma - \cos^3\gamma) - 2\cos\gamma] - 2\langle \cos\theta \rangle(\cos\gamma - \cos^3\gamma)\} \\ & + \frac{N}{2\varepsilon_0}\alpha_{aac}^{(2)}\langle \cos\theta \rangle \cos\gamma \end{aligned} \tag{4.10}$$

$$\begin{aligned} A_{yzy}(\theta, \psi) = {} & \frac{N}{2\varepsilon_0}(\alpha_{aac}^{(2)} - \alpha_{ccc}^{(2)})[(\langle \cos\theta \rangle - \langle \cos^3\theta \rangle)(5 + 3\langle \cos 2\psi \rangle)(\cos\gamma - \cos^3\gamma) \\ & + 2\langle \cos\theta \rangle \cos\gamma\big(\langle \cos^2\theta \rangle + \cos^2\gamma - 2\big)] \end{aligned} \tag{4.11}$$

for the symmetric stretching frequency, and

$$\begin{aligned} A_{yyz}(\theta,\psi) = \frac{N}{\varepsilon_0}\alpha^{(2)}_{caa}\{&-2\langle\cos\theta\rangle + 3(\langle\cos\theta\rangle - \langle\cos^3\theta\rangle)(1+\langle\cos 2\psi\rangle)](\cos\gamma - \cos^3\gamma) \\ &-2(\langle\cos\theta\rangle - \langle\cos^3\theta\rangle)\cos^3\gamma\} \end{aligned} \tag{4.12}$$

$$A_{yzy}(\theta,\psi) = \frac{N}{2\varepsilon_0}\alpha^{(2)}_{caa}[3(\langle\cos\theta\rangle - \langle\cos^3\theta\rangle)(\cos\gamma - \cos^3\gamma)(1+\langle\cos 2\psi\rangle) + 2\,\langle\cos^3\theta\rangle\cos^3\gamma] \tag{4.13}$$

for the asymmetric stretching modes. Here $\gamma = 56^\circ$ is the angle between the Si–C bond vector and v.

In order to use these expressions to assess the orientation of the two-methyl plane tilt and twist angle, we need to assume the form of an orientation distribution function (ODF). One option is to consider a Gaussian distribution with mean tilt angle θ_0 and width of the tilt distribution σ_θ, and mean twist angle ψ_0 with twist width σ_ψ. This is expressed as

$$f_{\mathrm{ODF}} = \exp\left[-\frac{(\theta-\theta_0)^2}{2\sigma_\theta^2} - \frac{(\psi-\psi)^2}{2\sigma_\psi^2}\right]. \tag{4.14}$$

In the limit $\sigma_\theta = \sigma_\psi \to 0$, this collapses to a δ distribution

$$f_{\mathrm{ODF}} = \delta(\theta-\theta_0; \psi-\psi_0) \tag{4.15}$$

where $\langle\cos\theta\rangle \to \cos\theta_0$ and $\langle\cos\psi\rangle \to \cos\psi_0$. Whatever form of f_{ODF} is chosen, we can now evaluate $\chi^{(2)}_{ijk}$ through the Lorentzian amplitudes A_{ijk} as a function of the ODF parameters where the amplitudes of the resonant modes are given by

$$A_{ijk} = \frac{\displaystyle\int_0^{2\pi}\int_0^{\pi} f_{\mathrm{ODF}}(\theta,\psi)\cdot A_{ijk}(\theta,\psi)\sin\theta\;\mathrm{d}\theta\;\mathrm{d}\psi}{\displaystyle\int_0^{2\pi}\int_0^{\pi} f_{\mathrm{ODF}}(\theta,\psi)\sin\theta\;\mathrm{d}\theta\;\mathrm{d}\psi} \tag{4.16}$$

where the denominator accounts for the normalization of the ODF. Now that the vibrational mode amplitudes, and therefore the $|\chi^{(2)}|^2$ spectra can be calculated for any tilt and twist angle distribution, some options present themselves for studying the temperature dependence of the methyl plane orientation. One approach is to use ratios of amplitudes within a single polarizations scheme such as SSP. Another approach is to use ratios of amplitudes of the same mode between different polarizations, for example A_{yyz}/A_{yzy} for the asymmetric stretch. The latter is slightly more robust, as it is less sensitive to the determination of the width parameter Γ. As we will demonstrate below, the method we employ uses this ratio information, along with the amplitude trends of all peaks with respect to temperature.

4.3 Results and Discussion

4.3.1 PDMS surface exposed to hydrophobic and hydrophilic environments upon heating

The experimental $|\chi^{(2)}_{yyz}|^2$ and $|\chi^{(2)}_{yzy}|^2$ spectra obtained after correcting for the local field factors[33,120] are plotted with points in Figure 4.2, showing PDMS methyl group modes in contact with D_2O and FC40 with increasing temperature. The $\chi^{(2)}$ lineshape was then fit using Eq. 4.7 with three modes: the CH_3 symmetric stretching mode (2910 cm^{-1}), the CH_3 asymmetrical stretching mode (2963 cm^{-1}), and a Fermi resonance (2938 cm^{-1} for the PDMS–D_2O interface, but not observed for PDMS–FC40). A previous orientation analysis shows that, within a single quadrant of θ, there is only one possibility for the phase of the coupled CH_3 symmetric stretch, but the asymmetric stretch could have positive or negative amplitude within the same range of tilt angles.[114] Although we have not performed a phase-resolved measurement, from the SSP fitting we are confident that these modes have opposite phases for both FC40 and D_2O spectra at all temperatures. The phase of the asymmetric stretching mode in SPS polarization was determined by comparing the solution to the $A_{\mathrm{as},yyz}/A_{\mathrm{ss},yyz}$ ratio. The relative phase of the CH_3 symmetric and asymmetric stretching modes in the SSP spectra was obtained through fitting. However, the relative phase of the CH3 symmetric stretching mode in SPS and SSP still needs to be addressed. Since the ratio $A_{\mathrm{ss},yyz}/A_{\mathrm{as},yyz}$ is sensitive to the widths of the modes in the fitting, it is not used in the orientation analysis of the methyl groups, but it can used to determine the

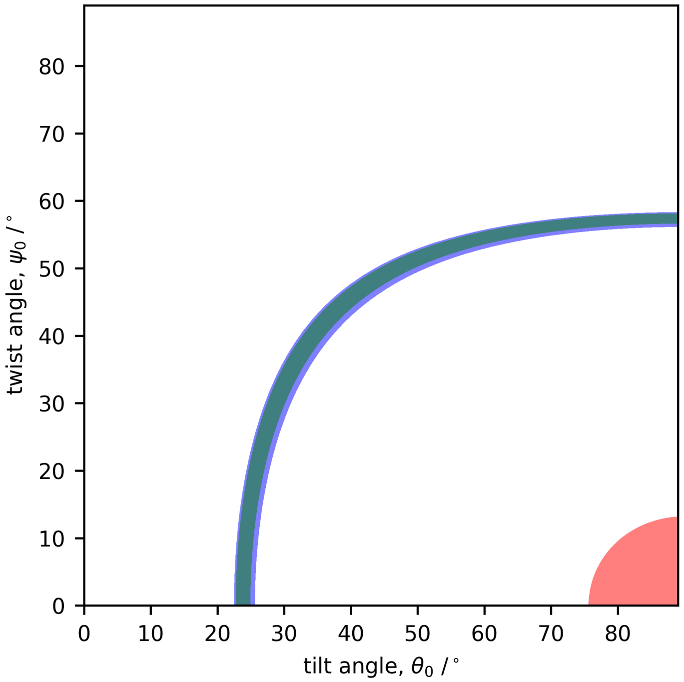

Figure 4.1: Orientation range obtained by: $A_{\mathrm{ss},yyz}/A_{\mathrm{as},yyz} = -2.27$, $A_{\mathrm{as},yyz}/A_{\mathrm{as},yzy} = -0.67$ (green),and $A_{\mathrm{as},yyz}/A_{\mathrm{as},yzy} = +0.67$ that are within 10% of the values found in the fitting of the experimental data.

phase of the CH_3 asymmetric stretching mode in SPS.[114] For example, the spectra of the PDMS–D_2O interface at 70 °C yields: $A_{\mathrm{ss},yyz} = 6.87$, $A_{\mathrm{as},yyz} = -3.03$, and $A_{\mathrm{as},yzy} = \pm 4.52$. Therefore, $A_{\mathrm{ss},yyz}/A_{\mathrm{as},yyz} = -2.27$, and $A_{\mathrm{as},yyz}/A_{\mathrm{as},yzy} = \pm 0.67$. All possible solutions of tilt and twist angles obtained from these values are presented in Figure 4.1. As shown here, $A_{\mathrm{ss},yyz}/A_{\mathrm{as},yyz} = -2.27$ and $A_{\mathrm{as},yyz}/A_{\mathrm{as},yzy} = -0.67$ gave a similar solution for the methyl orientation, while $A_{\mathrm{as},yyz}/A_{\mathrm{as},yzy} = +0.67$ gave a solution in a vastly different region. Therefore, it is determined that $A_{\mathrm{as},yzy} > 0$.

The PDMS–FC40 spectra were fitted with two modes: the CH_3 symmetric stretching mode at 2910 cm^{-1} and the CH_3 asymmetric stretching mode at 2963 cm^{-1}. The widths of the modes were determined to be 15 cm^{-1} and 8 cm^{-1}, respectively. As no Fermi resonance was observed for FC40 spectra, the FR mode was fixed at zero amplitude. The fit amplitudes are presented in Tables 4.1 and 4.2.

The PDMS–D_2O spectra were fit with three modes: the CH_3 symmetric stretching

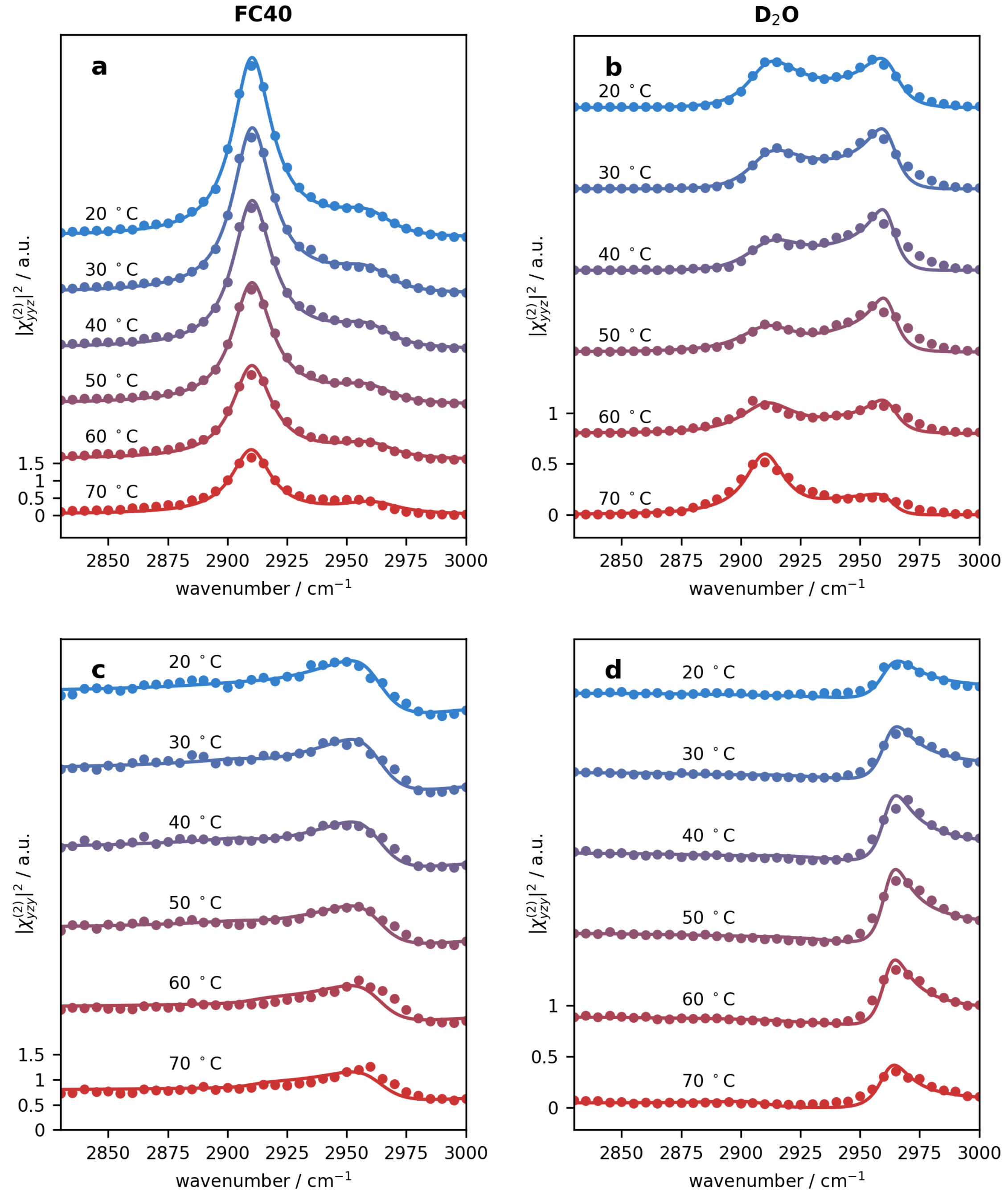

Figure 4.2: (a, b) $|\chi^{(2)}_{yyz}|^2$ and (c, d) $|\chi^{(2)}_{yyz}|^2$ spectra of the PDMS surface in contact with FC40 (a and c) and D$_2$O (b and d) with increasing temperature. Experimental data is shown in points, and the fit to Eq. 4.7 is plotted with lines.

Table 4.1: Fit amplitudes for PDMS–FC40 SSP spectra (shown in Figure 4.2a).

Temperature / °C	**CH$_3$ ss amplitude**	**CH$_3$, as amplitude**	**Fermi amplitude**	**NR amplitude**
20	21.55	−12.46	0.00	0.04
30	20.64	−12.15	0.00	0.04
40	19.57	−11.88	0.00	0.04
50	17.74	−10.69	0.00	0.04
60	15.67	−10.34	0.00	0.04
70	13.15	−9.46	0.00	0.05

Table 4.2: Fit amplitudes for PDMS–FC40 SPS spectra (shown in Figure 4.2c).

Temperature / °C	**CH$_3$ ss amplitude**	**CH$_3$, as amplitude**	**Fermi amplitude**	**NR amplitude**
20	–0.15	8.43	0.00	0.26
30	–0.44	8.41	0.00	0.25
40	–0.58	7.94	0.00	0.23
50	–0.29	7.24	0.00	0.22
60	–0.47	6.93	0.00	0.20
70	–0.62	6.69	0.00	0.16

mode at 2910 cm^{-1}, the CH$_3$ asymmetric stretching mode at 2963 cm^{-1}, and a Fermi resonance at 2938 cm^{-1}.[82,85,114,162] The width for the modes were determined to be 15 cm^{-1}, 8 cm^{-1}, and 15 cm^{-1}, respectively, from initial searching using global fitting. The fit amplitudes are presented in Tables 4.3 and 4.4.

Table 4.3: Fit amplitudes for PDMS–D$_2$O SSP spectra (shown in Figure 4.2b).

Temperature / °C	**CH$_3$ ss amplitude**	**CH$_3$, as amplitude**	**Fermi amplitude**	**NR amplitude**
20	7.71	–5.88	0.05	0.02
30	7.17	–5.43	0.44	0.03
40	6.77	–4.85	1.15	0.03
50	6.58	–4.89	2.28	0.00
60	6.89	–4.32	1.23	0.00
70	6.87	–3.03	2.19	0.00

A flowchart of the search algorithm used for the orientation analysis is presented in Figure 4.3. An exhaustive search was conducted to find ODF parameter combinations of the coupled methyl groups that would produce a $A_{\mathrm{as},yyz}/A_{\mathrm{as},yzy}$ ratio, and relative changes

Table 4.4: Fit amplitudes for PDMS–D_2O SPS spectra (shown in Figure 4.2d).

Temperature / °C	**CH_3 ss amplitude**	**CH_3, as amplitude**	**Fermi amplitude**	**NR amplitude**
20	0.23	4.13	0.00	0.08
30	0.30	4.35	0.00	0.10
40	0.43	4.58	0.00	0.11
50	0.20	4.57	0.00	0.11
60	0.13	4.42	0.00	0.10
70	0.22	4.52	0.00	0.07

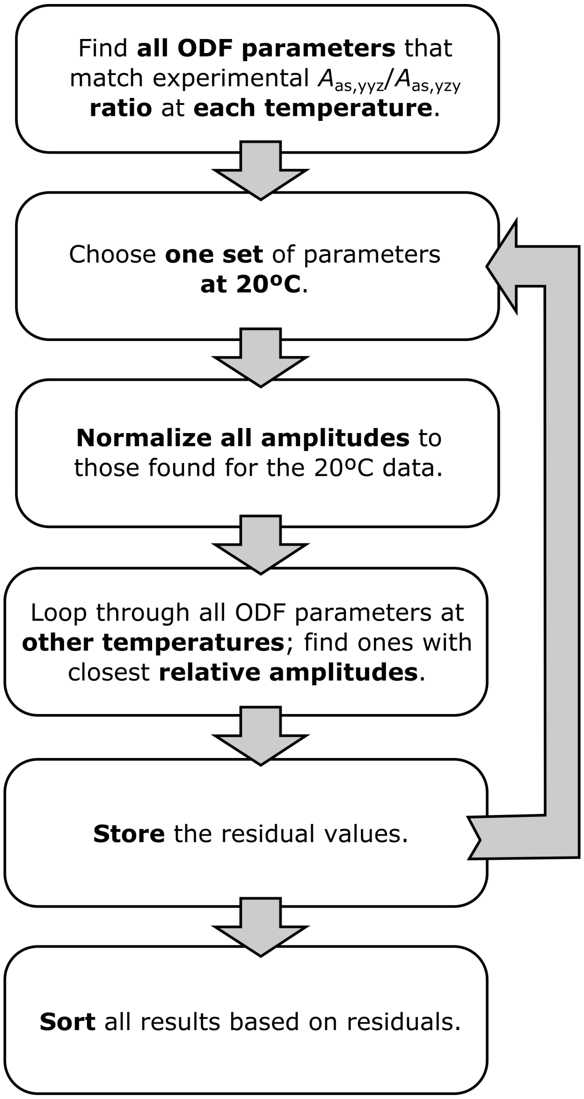

Figure 4.3: A flow chart outlining key steps of the search algorithm that uses a combination of the fit amplitudes together with the asymmetric A_{yyz}/A_{yzy} ratio to narrow the possible methyl plane tilt and twist angles.

in the amplitudes of all three CH_3 modes, that are consistent with the experimental data. This was accomplished by first finding all parameter combinations that have a $A_{\text{as},yyz}/A_{\text{as},yzy}$ ratio within 1% of the experimental value for each temperature. The combinations, together with the calculated amplitudes of the CH_3 modes, were stored for subsequent analysis. In the next step, all of the solutions for the 20 °C results are compared with those at the higher temperatures in order to restrict the solutions to those that also reproduce the changes in experimental fit amplitudes as a function of temperature. Our initial attempts used a Gaussian ODF (Eq. 4.14) to identify values of the parameters θ_0, σ_θ, ψ_0, and σ_ψ. Although solutions were found that were consistent with the experimental data, they could not be clustered with respect to temperature, and did not display any temperature trends. This is an indication that the experimental data does not provide enough constraints for a four-parameter ODF. We next explored the solutions of θ_0 and ψ_0 that resulted from a δ ODF (Eq. 4.15). Now the top 20 solutions at each temperature were determined to be highly clustered with respect to temperature (Figure 4.4) and have ratios and amplitudes in good agreement with the experimental data (Figure 4.5).

The results for PDMS–FC40 (Figure 4.4a) shows that the solutions for all temperatures (with median values indicated by black dots) lie along essentially the same $A_{\text{as},yyz}/A_{\text{as},yzy}$ grey contour. In the analysis of SFG data, it is generally considered that a constant amplitude ratio between polarization schemes indicates a constant orientation, and any intensity change is then typically attributed to a change in the surface number density N. In this case, however, we are able to make use of additional information in the form of the amplitude changes as a function of temperature. We are also in the situation where the solutions of the $A_{\text{as},yyz}/A_{\text{as},yzy}$ ratio as a function of (θ_0, ψ_0) can take on any value along a contour that extends over a very large range of θ_0 and ψ_0. By making use of the temperature trends, we are able to restrict the solutions, even though they are somewhat broad, to regions along these contours. Overall, the tilt and twist angles of the methyl groups on PDMS surface are increasing with elevated temperature. The median tilt angle

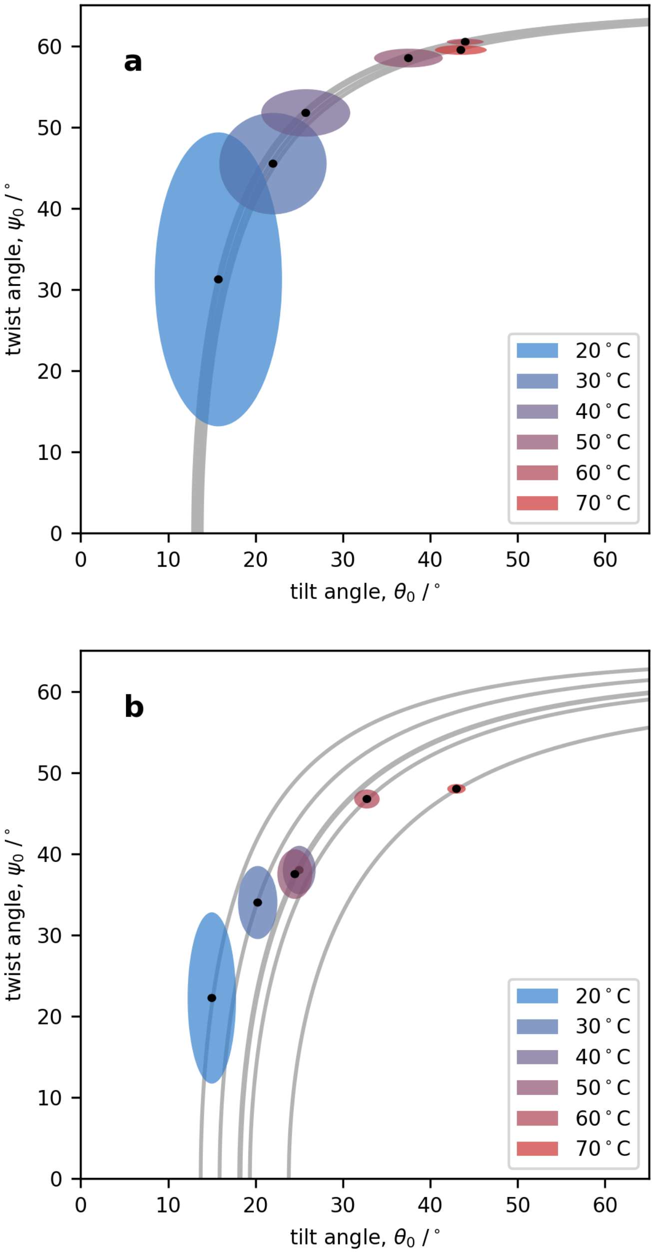

Figure 4.4: Search results of the PDMS surface methyl plane orientation in contact with (a) FC40 and (b) D_2O at different temperatures. Each contour represents a continuous set of tilt and twist angles that matches the experimental 2960 cm^{-1} symmetric/asymmetric amplitude ratio at each temperature. The ellipses are centered at the median θ_0 and ψ_0 values (black dots); their width and height indicate the range of possible solutions that are consistent with the experimental spectra.

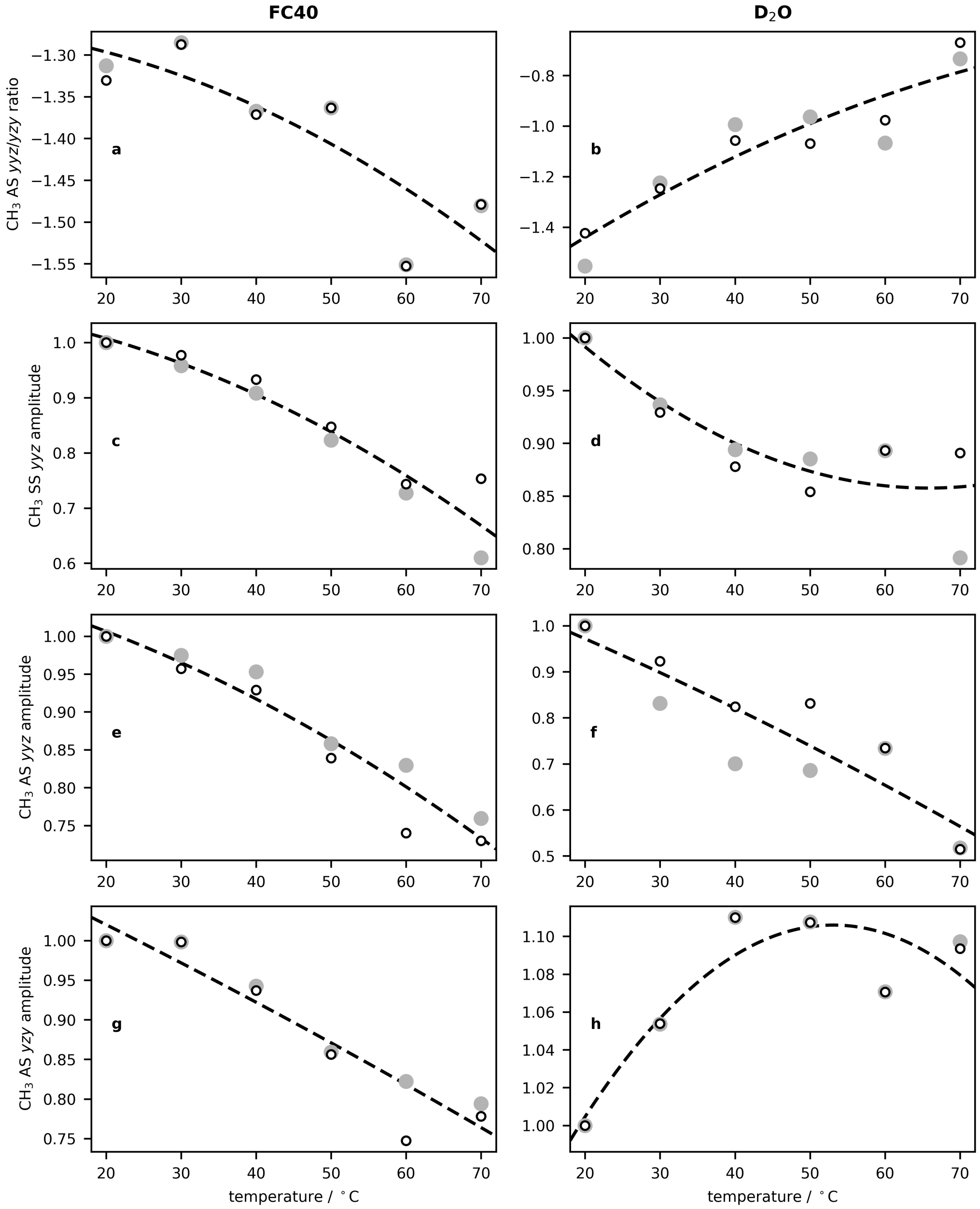

Figure 4.5: Fit (open black circles) and calculated (grey circles) (a, b) ratios and (c–h) amplitudes of the SS and AS modes in SSP and SPS polarization for FC40 and D_2O as a function of temperature, all normalized to 20 °C.

evolves from $\theta_0 = 16^\circ$ at 20 °C to $\theta_0 = 44^\circ$ at 70 °C, while the twist angle goes from $\psi_0 = 34^\circ$ at room temperature to 60 °C. The changes are generally monotonic, with θ_0 and ψ_0 levelling off at higher temperatures. For the PDMS–D_2O interface (results in Figure 4.4b) the trend is similar. Here the solutions at the different temperatures are situated on different $A_{\mathrm{as},yyz}/A_{\mathrm{as},yzy}$ contours, but our method remains the same. At room temperature the tilt angle starts at $\theta_0 = 14\ ^\circ$ and increases to $\theta_0 = 44^\circ$ at 70 °C; the corresponding twist angle increased from $\psi_0 = 22^\circ$ to $\psi_0 = 50^\circ$.

A cartoon depiction of the orientation change with temperature is presented in Figure 4.6. At room temperature (Figure 4.6a), the consequence of our θ_0 and ψ_0 determination is that the two methyl groups are both directed towards one medium. Although we lack absolute phase information in our measurements, molecular dynamics simulations of the PDMS surface exposed to vapour and bulk water show that the methyl groups remain directed into the bulk water phase, attributed to an inability of PDMS oxygen atoms to form hydrogen bonds with water.[163] As the temperature increases, both angles become larger, and bring the methyl groups closer to the plane of the surface. At 70 °C, one methyl is almost parallel to the surface, while the other has a slightly smaller tilt angle (for a single methyl group, the tilt θ_{CH3} is between the C–Si bond vector and the z axis). We propose that this may be due to the backbone of the PDMS polymer being distributed in the plane of the surface, consistent with results from simulations.[164] At elevated temperatures, our methyl plane θ_0 and ψ_0 results suggest that portions of the backbone adopt an out-of-plane conformation with respect to the surface (Figure 4.6b). Temperature-dependent viscosity data indicates that the density of PDMS decreases by 5% in our temperature range of interest.[159] On the surface, the polymer network expands more in the z direction than in the x and y directions, resulting in a more corrugated surface backbone conformation that brings the methyl groups closer to the plane of the PDMS–liquid interface. This is further supported by an increase in contact angle[131] and surface roughness[165] at elevated temperatures. The trends were found to be similar for the two different PDMS environments studied. At room temperature, experiments and simulations have shown that the PDMS surface does not significantly restructure in response to the hydrophobicity of the environment.[82, 146, 164]

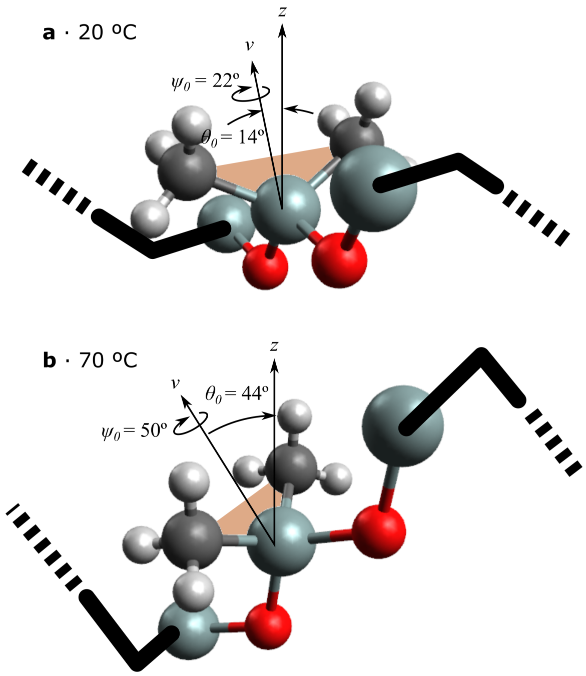

Figure 4.6: A visualization of the relationship between the methyl group plane (shaded orange) and polymer chain backbone proposed conformation at (a) 20 °C (b) 70 °C (b) when exposed to FC40 or D_2O. The blue spheres represent silicon atoms, red are oxygen atoms, grey are carbon, and white are hydrogen atoms. For clarity, methyl groups are drawn on the central Si atom only. The heavy black lines represent the extension of the PDMS backbone.

4.3.2 Other possibilities for temperature-dependent changes in the orientation distribution

Although we have established that we do not have enough data to support the analysis of simultaneous changes in mean tilt and twist angles (θ_0 and ψ_0) and changes in the width of the distributions, σ_θ and σ_ψ, we now investigate one other possibility for which the data may be sufficiently constrained for analysis. We can explore the possibility where the PDMS surface methyl plane maintains a specific mean tilt and twist angle, but the width of the distribution changes with temperature. For this, we return to the Gaussian ODF

(Eq. 4.14) and perform an analysis that is similar to that described above, except that we search for any (fixed) values of θ_0 and ψ_0 with a temperature-dependent change in σ_θ and σ_ψ.

The resulting $A_{\mathrm{as},yyz}/A_{\mathrm{as},yzy}$ ratio and relative amplitudes of the three CH_3 modes from the search, together with the experimental data are presented in Figure 4.7. Here the tilt and twist angles have a Gaussian distribution about their mean values and their widths σ_θ and σ_ψ considered to be a function of temperature. As shown in the figure, even though the calculated $A_{\mathrm{as},yyz}/A_{\mathrm{as},yzy}$ ratio is consistent with the experimental results, the calculated relative amplitudes of the three CH_3 modes are all drastically different from the experimental results, indicating that such solutions are not consistent with the experimental observations. In conclusion, changes in the width of the tilt and twist distribution alone cannot explain the temperature-dependent variation in the spectra for the two PDMS surfaces.

4.3.3 Spectral changes upon cooling

Spectra were also collected in the reverse direction, cooling from 70 °C back to room temperature. These results are shown in Figure 4.8. For both PDMS–FC40 and PDMS–D_2O interfaces, the general trends were the same in the heating and cooling directions. In the case of FC40, the results were nearly identical for heating and cooling, and the orientation changes we have presented are therefore deemed to be reversible. In the case of D_2O, the SPS spectra are the same on heating and cooling, but the SSP spectra on cooling have a more pronounced Fermi resonance at intermediate temperatures, then produce nearly identical spectra when returning to room temperature, suggesting that the tilt/twist pathway does not evolve in exactly the same manner. However, the fact that the surface structure returns to the same state upon cooling is of interest for outdoor environmental applications such as sealants and silicone power insulators, as weathering often consists of significant daily temperature fluctuations. Our studies have consisted of a single heating

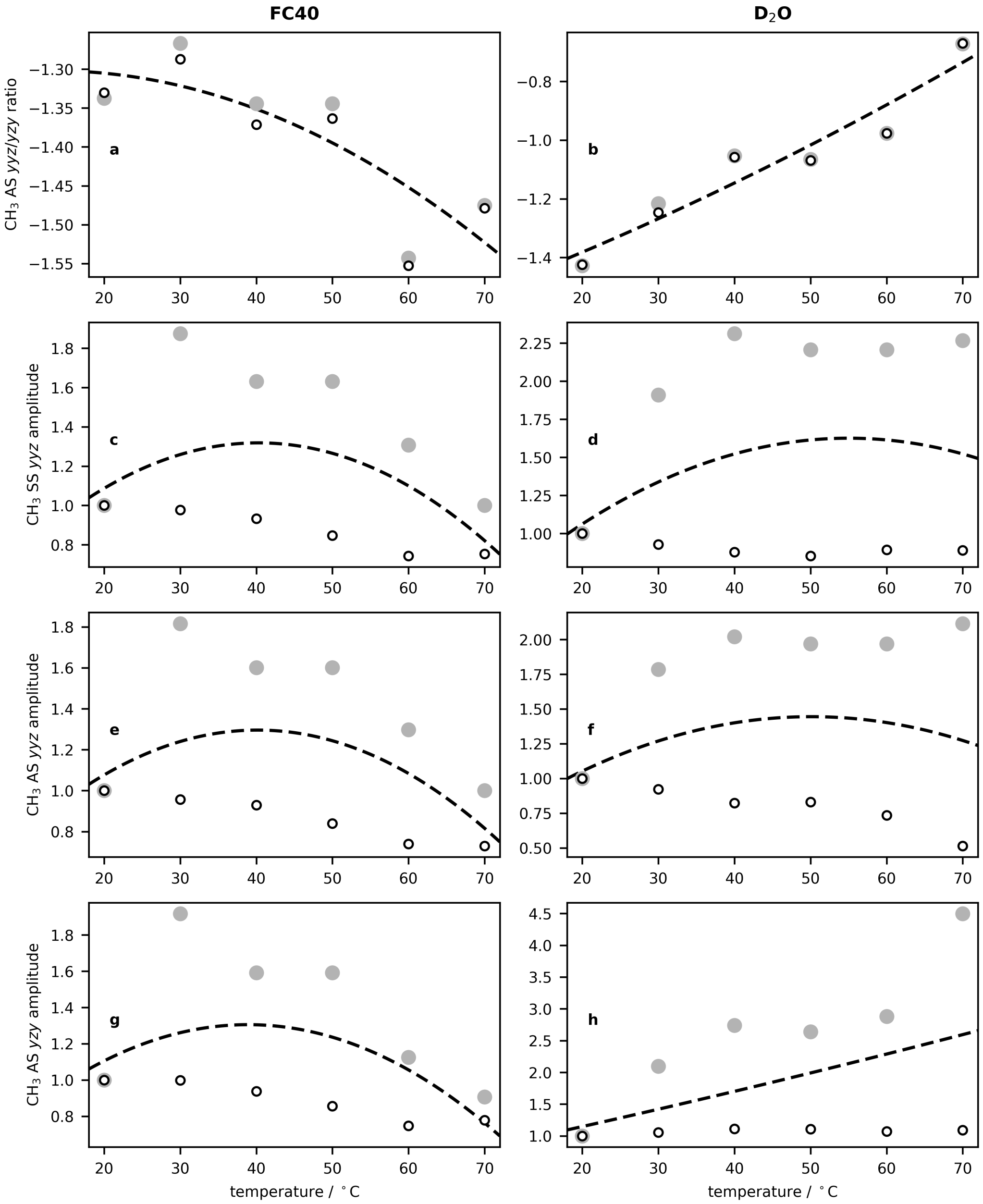

Figure 4.7: Fit (open black circles) and calculated (grey circles) (a, b) ratios and (c–h) amplitudes of the symmetric and asymmetric modes in SSP and SPS polarization for FC40 and D$_2$O as a function of temperature, all normalized to 20 °C.

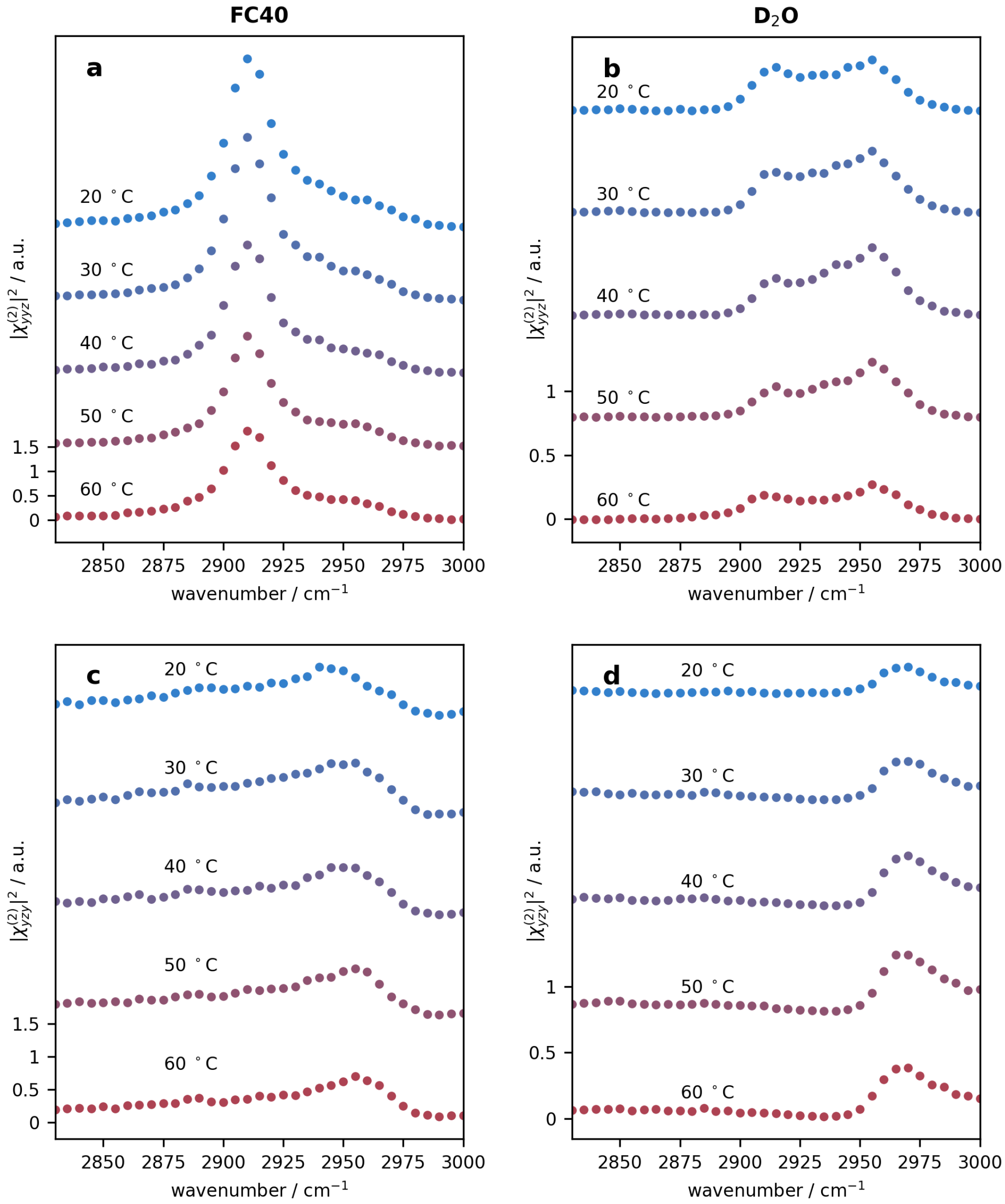

Figure 4.8: SFG spectra of the PDMS surface in contact with FC40 (a & c) and D_2O (b & d) with decreasing temperature in both SSP (a & b) and SPS (c & d) polarization schemes. The spectra at 70 °C are shown in Figure 4.2

and cooling cycle; future accelerated aging experiments investigating the effects of long-term temperature cycling on microscopic chemical level will be important.

4.4 Conclusions

We have monitored the PDMS surface exposed to hydrophobic (FC40) and hydrophilic (D_2O) liquids from 20 °C to 70 °C using vibrational SFG spectroscopy probing the surface methyl groups. We have also presented a framework that enables a deeper level of orientation analysis than is usually performed with a single ratio of vibrational mode amplitudes in two beam polarizations. When an external perturbation is applied (in this case a change in temperature), we narrow the possibilities in the parameterization of a model orientation distribution function by finding solutions that are consistent with the relative changes in mode amplitudes. The more spectra that are collected at different temperatures, the further constrained are the possibilities. This analysis suggests that the temperature-dependent change in surface methyl group orientation is similar when exposed to hydrophobic or hydrophilic environments: the methyl groups are in an approximately upright orientation at room temperature and then are increasingly tilted towards the surface at elevated temperatures. We propose that the change can be explained by the corresponding conformation of the siloxane backbone in the surface region as the surface becomes more corrugated at higher temperatures due to the concomitant decrease in density. Such findings are relevant to applications where prolonged hydrophobicity of silicone materials is of interest, and in the control of aqueous droplets through temperature programming of next-generation microfluidics technologies.

Chapter 5

Silica Surface Charge Enhancement at Elevated Temperatures Revealed by Interfacial Water Signals[*,†]

5.1 Introduction

Over the past 30 years, nonlinear optical spectroscopy has revealed some fundamental characteristics of the silica surface, particularly with respect to its interaction with water.[43,70,166–181] The hydrogen-bonding environment within the first nanometer of the surface—encompassing only 2–3 molecular layers—has been shown to be substantially different from that of bulk water, and is therefore implicated in surface chemistry and the microenvironment that dictates adsorption of organic species in aqueous solution. At the same time, such techniques are also sensitive to water molecules found further into the diffuse double layer.[43–45] Despite the recognized importance of the silica surface, it has been difficult to assess the surface charge and the thermodynamic parameters governing the silanol deprotanation from potentiometric titration on account of the temperature-dependent dissolution of colloidal silica.[182–185]

---

[*] Reproduced in part from Azam, Md. S.; Cai, C.; Gibbs, J. M.; Tyrode, E.; Hore, D. K. "Silica Surface Charge Enhancement at Elevated Temperatures Revealed by Interfacial Water Signals" *J. Am. Chem. Soc.*, **142**, 669–673 (2020). Copyright 2020 American Chemical Society.

[†] All data collection, including preparation of polymer surfaces and solutions, and measurement of SFG spectra performed by Azam. Treatment of data, model development, and analysis of data done by Cai. Gibbs and Tyrode provide expertise on silica deprotonation. Azam, Cai, and Hore contributed to the discussion of the results, and to the writing of the manuscript.

Studying a planar silica surface, we observe that upon increasing the temperature, the interfacial water signal increases up to $\approx 60^\circ$C, after which the signal drops. Using a model we have recently developed for the silica–water interface,[47] we demonstrate that this behavior is consistent with a monotonic increase in surface charge, approaching a value of -0.03 C·m^{-2} at 75 °C. These findings account for fundamental physical phenomena, such as the enhanced dissolution of silica at elevated temperatures.[182–185] They also explain the lower heat of dissociation of DNA strands on glass compared to bulk solution, a critical factor enabling that biotechnological advance.[186]

5.2 Background

For charged aqueous surfaces, the water response is considered to have a surface contribution through $\chi^{(2)}$ and a bulk contribution through $\chi^{(3)}$. The pioneering work of Eisenthal *et al.* has recognized that the $\chi^{(3)}$ contribution is modulated by the surface potential Φ_0 and proposed that $I \propto |\chi^{(2)} + \Phi_0\chi^{(3)}|^2$.[43] It was later realized that the full surface potential is not experienced at all ionic strengths, and that an angle- and ionic strength-dependent factor f_3 should be included so that $I \propto |\chi^{(2)} + f_3\Phi_0\chi^{(3)}|^2$.[44,45] It has recently been demonstrated that, at low ionic strengths where the surface potential is high, the Debye-Hückle approximation is not valid, and the product $f_3\Phi_0$ should be replaced by a more accurate function of the surface potential that we call g_3 resulting in,[47]

$$I \propto |LLL|^2|\chi^{(2)} + g_3\chi^{(3)}|^2, \tag{5.1}$$

where

$$g_3 = \Phi_0 - \frac{4ikT\Delta k}{e}\sum_{n=1}^{\infty}\frac{\xi^{2n-1}}{(2n-1)[i\Delta k - \kappa(2n-1)]}, \tag{5.2}$$

and

$$\xi = \tanh\left[\frac{e\Phi_0}{4kT}\right].$$

Here e is the electron charge, k is Boltzmann's constant, T is the absolute temperature, and L are the local field corrections that are described in more detail below. These expressions

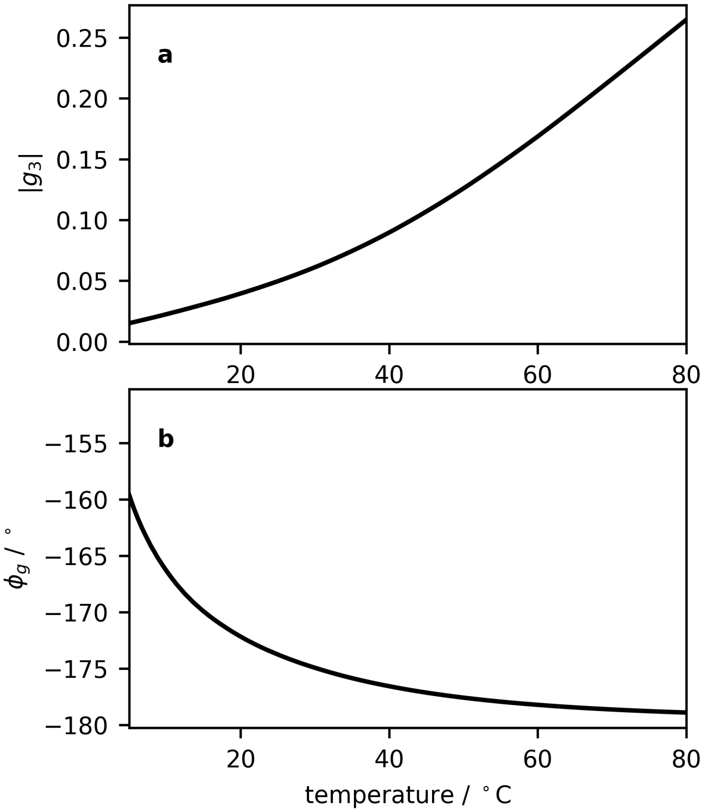

Figure 5.1: (a) Magnitude and (b) phase of g_3 as a function of temperature. Reprinted with permission from Ref. 150. Copyright 2020 American Chemical Society.

also account for the angle-dependence of the SFG intensity.[47,187] Figure 5.1 illustrates the variation in the magnitude and phase of g_3 over the temperature range of interest. The ratio of $|\chi^{(2)}|/|\chi^{(3)}|$ against temperature has been plotted in Figure 5.2.

5.3 Experimental

A detailed description of the laser system used for our vibrational SFG spectroscopy experiments has been described previously.[70] Briefly, the system consists of a Nd:YAG laser (Ekspla PL2241A) that generates a 30 ps pulse with a repetition rate of 10 Hz at 1064 nm (fundamental) and 532 nm (second harmonic). A portion of the second harmonic output and the fundamental are used to pump an optical parametric generator (Ekspla PG501) to produce tunable IR frequencies from 2800–3700 cm^{-1}. The IR beam

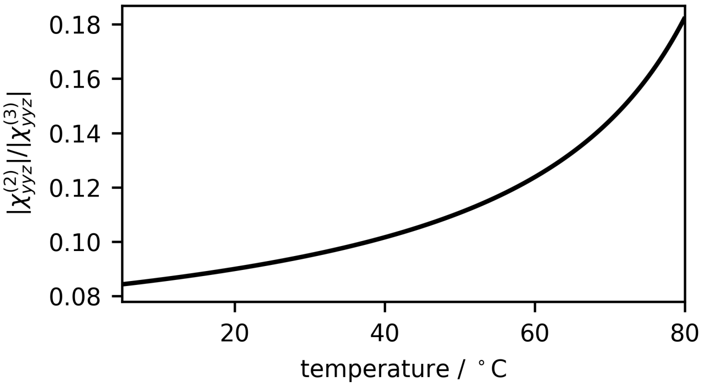

Figure 5.2: The ratio of $|\chi^{(2)}|/|\chi^{(3)}|$ as a function of temperature. Reprinted with permission from Ref. 150. Copyright 2020 American Chemical Society.

(≈ 230 μJ/pulse) and second harmonic visible output (120 μJ/pulse) were then transmitted through polarizers, and finally incident on the surface of an IR-grade fused silica dove prism (Del Mar Photonics), approaching at $\theta_{\text{IR}} = 74.3 \pm 0.3^\circ$ and $\theta_{\text{vis}} = 64.5 \pm 0.3^\circ$. Just before the surface, the each beam has a diameter of $d = 600 \pm 100$ μm. Since we are using such large angles, the intensity is significantly reduced as the area of the beams at the surface is $\frac{1}{4}\pi d^2/\cos\theta$. The prism was mounted against a custom Teflon vessel with a fluoropolymer O-ring (Marco Rubber, NH) and the vessel was filled with 18.2 MΩ·cm deionized water (Milli-Q). The temperature of the water was varied by employing a cooling and heating circulator (PolyScience 9112) channelled through an aluminum block surrounding the Teflon cell. A thermometer was immersed in the Teflon cell to read the actual temperature of water in contact with silica surface. The SFG light generated from the silica–water interface was then collected at 20 cm^{-1} IR wavenumber steps and average of 100 laser shots were recorded.

The prism was cleaned before each experiment by dipping into a 500 mL glass beaker containing piranha solution (3:1 mixture of sulfuric acid and 30% hydrogen peroxide) for 1 h. (*Note: Use caution, piranha solution reacts explosively with organic compounds.*) The prism was then taken out of the beaker, rinsed copiously in 18.2 MΩ·cm deionized water (5 × 300 mL), sonicated in 300 mL water for 2 min, and again rinsed with water (2 ×

300 mL) to completely remove any acid. The piranha-cleaned prism was then placed in a preheated oven at 85°C for 1 h under vacuum.

5.4 Results and Discussion

5.4.1 Dielectric constant, refractive index, and local fields

As the model presented in Equation 5.1 requires consideration of the local field correction factors L, we need to account for the effect of temperature on the linear optical properties. The temperature-dependent dielectric constant of water (ε_{R}) can be represented by the linear-response formula[188]

$$\varepsilon_{\mathrm{R}} = 1 + \frac{4\pi |\mathbf{M}^{\mathrm{w}}|^2}{V k_{\mathrm{B}} T} \tag{5.3}$$

where V is the volume of the simulation cell and $\mathbf{M}^{\mathrm{w}}$ is the total dipole moment of the water molecules obtained in an MD simulation by Joutsuka *et al.*[189] We obtain the temperature-dependence of ε_{R} by interpolating their simulation data. The final expression for the temperature-dependent dielectric constant of water is

$$\varepsilon_{\mathrm{R}} = 1 + \frac{22415.8721}{T} \tag{5.4}$$

Wavelength- and temperature-dependent refractive index of water were taken from the

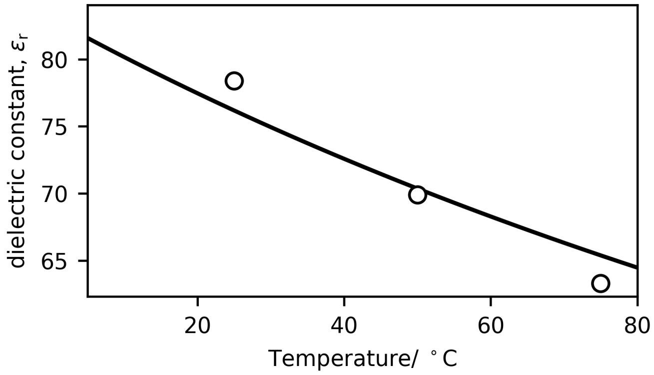

Figure 5.3: Fitted curve of temperature-dependent dielectric constant of water and experimental data from Joutsuka *et al.*[189] Reprinted with permission from Ref. 150. Copyright 2020 American Chemical Society.

literature using[190]

$$n(\lambda,t) = A(t) + \frac{B(t)}{\lambda^2} + \frac{C(t)}{\lambda^4} + \frac{D(t)}{\lambda^6} \tag{5.5}$$

where A, B, C, and D are the Cauchy coefficients as a function of temperature (t in Celcius)

$$A(t) = 1.3208 - 1.2325 \times 10^{-5}t - 1.8674 \times 10^{-6}t^2 + 5.0233 \times 10^{-9}t^3 \tag{5.6a}$$

$$B(t) = 5208.2413 - 0.5179t - 2.284 \times 10^{-2}t^2 + 6.9608 \times 10^{-5}t^3 \tag{5.6b}$$

$$C(t) = -2.5551 \times 10^8 - 18341.336t - 917.2319t^2 + 2.7729t^3 \tag{5.6c}$$

$$D(t) = 9.3495 + 1.7855 \times 10^{-3}t + 3.6733 \times 10^{-5}t^2 - 1.2932 \times 10^{-7}t^3. \tag{5.6d}$$

The temperature-dependent refractive index of silica was also incorporated in our model using the literature expression[157]

$$n^2 - 1 = \sum_{i=1}^{3} \frac{a_i}{b_i^2 - E^2} \tag{5.7}$$

and,

$$a_i = a_{i0} + a_{i1}t + a_{i2}t^2 \tag{5.8a}$$

$$b_i = b_{i0} + b_{i1}t + b_{i2}t^2. \tag{5.8b}$$

E is the photon energy in electron volt, and t is the temperature in Celsius. Values of the parameters a_{in} and b_{in} can be found in the literature.[157]

The local field coefficients were then calculated using the temperature-dependent refractive index of water and fused silica

$$(LLL)_{yyz} = L_y^{\mathrm{SFG}} L_y^{\mathrm{vis}} L_z^{\mathrm{IR}} \tag{5.9}$$

with

$$L_y = 1 + r_s \tag{5.10a}$$

$$L_z = (1 + r_p)\sin(\theta_1)\left(\frac{n_1}{n'}\right)^2 \tag{5.10b}$$

where

$$r_s = \frac{n_1\cos(\theta_1) - n_2\cos(\theta_2)}{n_1\cos(\theta_1) + n_2\cos(\theta_2)} \tag{5.11a}$$

$$r_p = \frac{n_2\cos(\theta_1) - n_1\cos(\theta_2)}{n_1\cos(\theta_2) + n_2\cos(\theta_1)} \tag{5.11b}$$

$$n' = \frac{n_1 + n_2}{2}. \tag{5.11c}$$

In the above expressions, n_1 is the refractive index at the appropriate wavelength and temperature in fused silica and n_2 is the refractive index of corresponding wavelength and temperature in water. θ_1 and θ_2 are the incident angle and refracted angle at the corresponding wavelength.

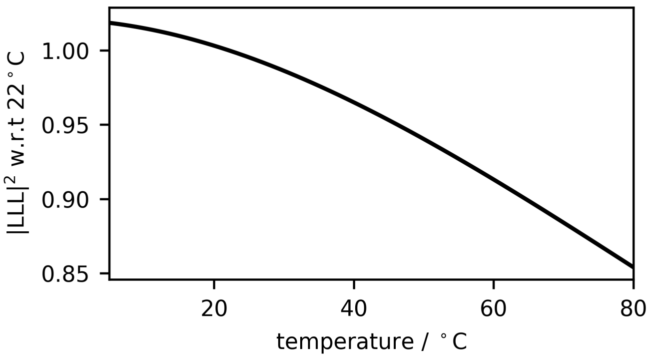

Figure 5.4: Magnitude squared of the product of the three local field coefficients, $|LLL|^2$, normalized to 22°C. Reprinted with permission from Ref. 150. Copyright 2020 American Chemical Society.

5.4.2 Deprotonation of silanol groups and resulting surface charge

The sensitivity of the water response to surface charge was first reported by Eisenthal and coworkers nearly three decades ago in a second-harmonic generation study using NaCl to modulate the surface potential of silica.[43] That work prompted many studies in the area, investigating specific ion effects,[70,166–175] the influence of surface conditions,[191,192] and bulk pH.[43,176–181] A significant development in the field was the illustration that not all water molecules experienced the effects of the surface potential, and screening due to ions limits the influence of the potential at low ionic strength.[44,45] We have recently demonstrated that the combination of low ionic strength with an experimental geometry near the critical angle results in a very sensitive probe of the surface charge density, as the Debye length becomes commensurate with the wavevector mismatch.[47] A fraction of the surface silanol groups is deprotonated at a specific bulk ionic strength, resulting in a substantial increase of the surface hydronium ion concentration. This enables the surface charge density to be determined, and ultimately results in a surface potential from the Poisson-Boltzmann equation. Experimental data obtained above and below the critical angle (effectively varying the nonlinear coherence length) enabled us to account for the spectral intensity profile at 22 °C.[47]

When applied to surface silanol deprotonation, that model intrinsically accounts for the temperature-dependence of the surface potential. At a charged interface such as a mineral oxide, third-order nonlinear effects contribute to the measured response.[43–45,47] For most systems, the dominant component of this additional response is the molecular hyperpolarizability, scaled by the inverse temperature.[43] (See the Supporting Information for details of the expressions.) Although it is challenging to experimentally separate these two contributions to the signal,[45,170,193–197] a theoretical study explicitly modelling the third-order response of water in the presence of a surface field has demonstrated that the decrease in signal is larger than what is observed for the second-order term, even after accounting for the inverse temperature dependence.[189]

We have performed sum frequency generation (SFG) measurements with the incident visible and infrared beams s- and p-polarized, respectively, and the s-component of the SFG intensity selected for detection. Spectra acquired at temperatures in the range of 10–75 °C are shown in Figure 5.5. One can observe that the intensity at all IR frequencies increases from 10–60 °C and then drops from 60–75 °C. The trend may be seen more clearly in Figure 5.6 (points). We now relate this change in SFG signal with the extent of deprotonation of the silanol groups that substantially increases with temperature.[198]

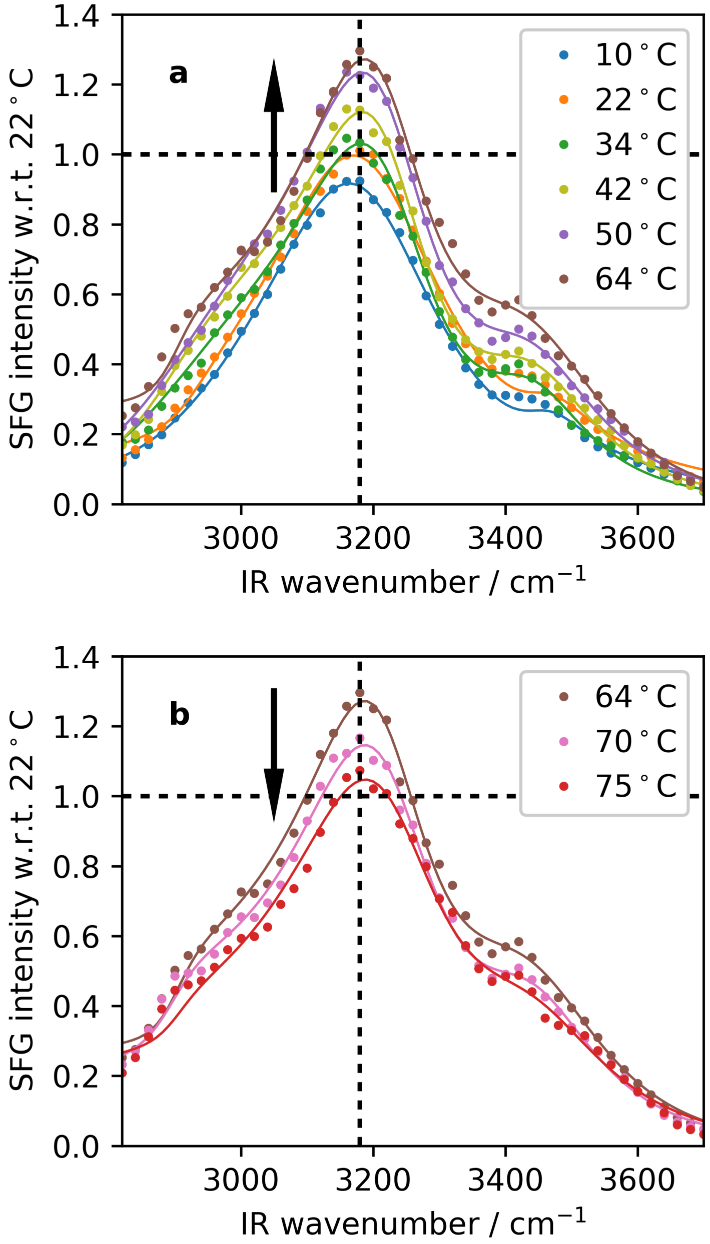

Figure 5.5: Visible-infrared sum-frequency spectra of water at the silica surface as a function of the bulk water temperature, normalized to the intensity of the 3180 cm^{-1} peak at 22°C. The intensity increases in the range (a) 10–64°C, and then (b) decreases towards 75°C. Reprinted with permission from Ref. 150. Copyright 2020 American Chemical Society.

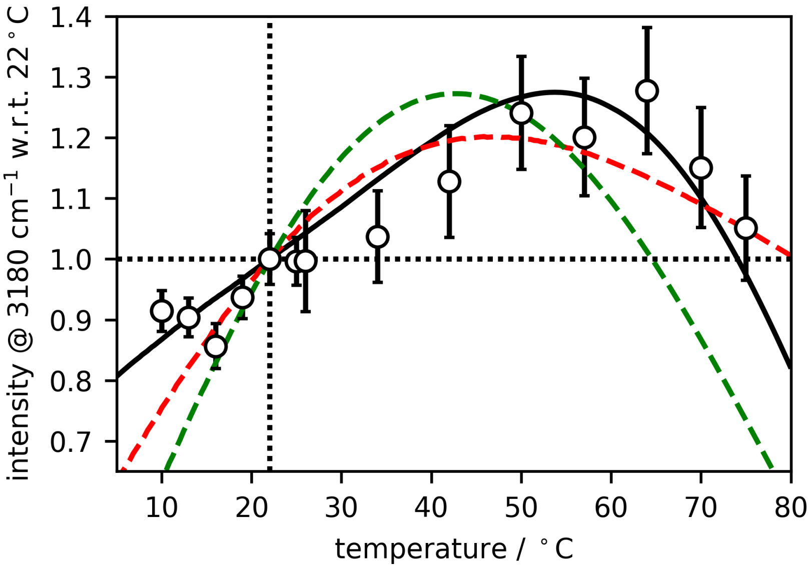

Figure 5.6: Experimental data (points) and the two-pK_a model (black line) fit to the intensity at 3180 cm^{-1}. Error bars represent the standard deviation of the mean of 100 laser shots. The dashed lines represent the results to a model with p$K_{a,1}$ only (green) and p$K_{a,2}$ only (red). Reprinted with permission from Ref. 150. Copyright 2020 American Chemical Society.

Experiments and molecular simulations of water at silica interfaces have suggested that the deprotonation is predominantly due to two different silanol sites, a more acidic site with p$K_{a,1} \approx$ 4–6, and a less acidic site with p$K_{a,2} \approx$ 7–10.[43, 168, 192, 199, 200] We have treated our data following a recent simulation study reporting p$K_{a,1} = 5.7$ and p$K_{a,2} = 8.5$.[192] Another important parameter governing the surface charge is the relative population of the two sites. Early second-harmonic generation studies by Eisenthal *et al.* illustrated a 19:81 ratio of the more to less acidic sites at high ionic strength.[43] Studies at low ionic strength indicated that the ratio is in the range of 40:60,[168, 199] and we have used this ratio in our current model. We assume that the deprotonation of each site is described by an equilibrium constant

$$K_a = \frac{[\mathrm{H}^+]_0[\mathrm{SiO}^-]_0}{[\mathrm{SiOH}]_0} \tag{5.12}$$

where the surface proton concentration $[\mathrm{H}^+]_0$ can be expressed in terms of that in the bulk

$[\mathrm{H}^+]_\infty$ by

$$[\mathrm{H}^+]_0 = [\mathrm{H}^+]_\infty \exp\left[-\frac{e\Phi_0}{kT}\right]. \tag{5.13}$$

The temperature-dependent pH data of pure water were taken from Truman.[201] This enables us to write the equilibrium constant in terms of the fraction of the surface that is deprotonated, α

$$K_a = \frac{\alpha}{1-\alpha}[\mathrm{H}^+]_\infty \exp\left[-\frac{e\Phi_0}{kT}\right]. \tag{5.14}$$

Even though we cannot rearrange Eq. 5.14 to obtain an analytical expression for α, the equation can be solved numerically from

$$\sqrt{I} = \frac{\alpha e}{A_\mathrm{M}\sqrt{8\varepsilon_\mathrm{R}\varepsilon_0 kT}}\left[\sinh\left(\frac{1}{2}\left(\ln[\mathrm{H}^+]_\infty - \ln K_a - \ln\left(\frac{1-\alpha}{\alpha}\right)\right)\right)\right]^{-1}. \tag{5.15}$$

We therefore obtain the degree of deprotonation for each of the sites α_1 (p$K_a = 5.7$) and α_2 (p$K_a = 8.5$). Now that we have a model for α_1 and α_2, we can calculate the surface charge density from the surface area per silanol, based on the relative population of each site. The surface charge density σ is given by

$$\sigma = \frac{\alpha_1 e}{A_1} + \frac{\alpha_2 e}{A_2} \tag{5.16}$$

where A is the area per silanol A_M, and e is the electron charge. A needs to take the relative population of the two sites into account. Early work considered the two sites to have population ratios of 19:81 at high ionic strength.[43] We model a ratio of 40:60 based on experiments performed at low ionic strength.[168,199] Using an area per silanol group of 90 Å^{2}[202,203] we arrive at $A_1 = 227$ Å^2 and $A_2 = 152$ Å^2. This then enables calculation of the surface potential through

$$\Phi_0 = \frac{2kT}{e}\sinh^{-1}\left[\frac{\sigma}{\sqrt{8I\varepsilon_\mathrm{R}\varepsilon_0 kT}}\right]. \tag{5.17}$$

The factor g_3 (Figure 5.1) controls the interference between the second- and third-order susceptibility $\chi^{(2)}$ and $\chi^{(3)}$, and is a function of ionic strength, beam geometry, and the surface potential (Figure 5.7). We use the temperature-dependence of $\chi^{(3)}$ reported by

Joutsuka *et al.*[189] (Figure 5.7a, points). The decreasing $\chi^{(3)}$ with increasing temperature was found to be well-correlated to the dropping of dielectric constant, and they both reflect the reduced response of water molecule reorientation to external electric field.[189] A model for the temperature-dependence of $\chi^{(2)}$ is more difficult to obtain, as it depends on the structure of the water molecules in contact with the surface. We use the calculated values for $\chi^{(2)}$ at the air–water interface from Nagata *et al.* (Figure 5.7b, points), where it was determined that negligible reorientation occurs at elevated temperatures.[204] We have used SSP data in our analysis, as it lends itself to quantitative modeling on account of the single value of the nonlinear susceptibility that it probes. However, analysis of the trends in the PPP signal (all beams p-polarized, shown in Figure 5.10) reveals a similar trend. This indicates that the structure of the bonded interfacial layer does not change appreciably with temperature, supporting the parameters we have used to construct our model. The van't Hoff equation was used to describe the $\ln K_a$ change with temperature.

$$\ln K_a = -\frac{\Delta H}{RT} + \frac{\Delta S}{R} \tag{5.18}$$

The ultimate goal is to find the ΔS and ΔH for the two silanol species that account for the trend in the SFG data. Since we are using literature pK_a values at 22°C for two species, the relationship between ΔS and ΔH can be expressed as

$$\Delta S = R\left[\frac{\Delta H}{295.15\ \mathrm{K}} + \log_e(10^{-\mathrm{p}K_a})\right] \tag{5.19}$$

for each species. We constructed a function that takes the ΔH values and evaluates the residual between the predicted SFG signal using our model described above and the experimental data. We then performed an exhaustive search spanning from 0–1000 kJ/mol for ΔH of both silanol species (ΔH_1 and ΔH_2). After our code finds the global minimum, it further optimizes the result with a downhill simplex algorithm. A fit to the experimental data using Eq. 5.18 results in the temperature-dependence of the pK_a at each site as shown in Figure 5.9a, and the fraction of each site that deprotonated in Figure 5.9b. We are therefore able to determine the surface charge density (black line in Figure 5.9c), and

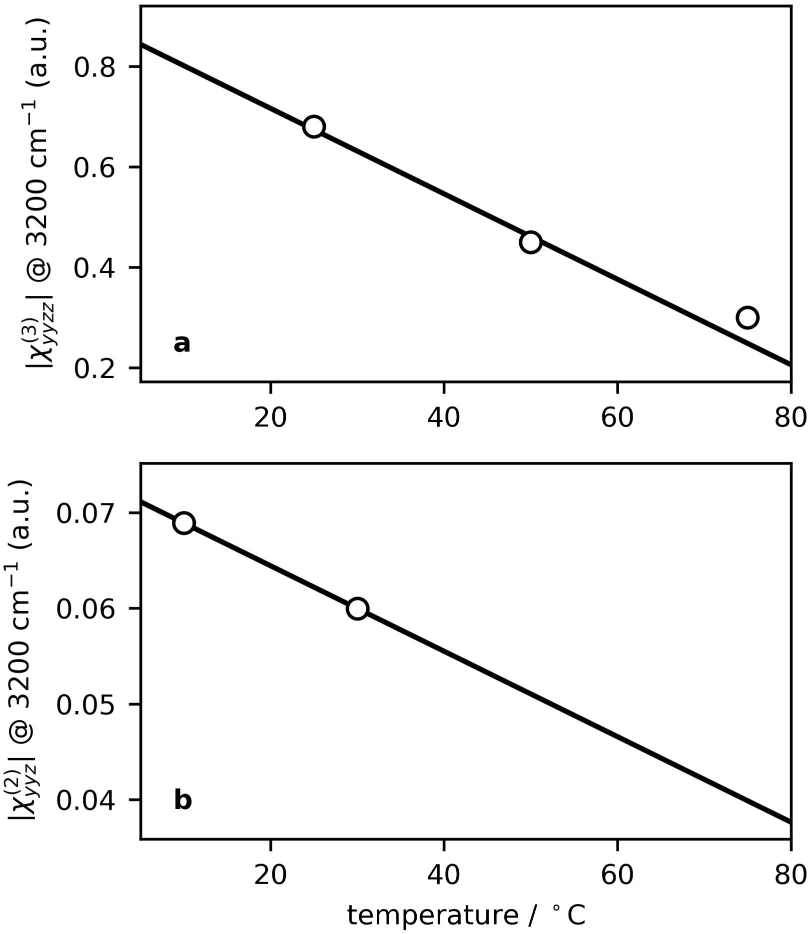

Figure 5.7: (a) Temperature dependence of $|\chi^{(3)}|$ (lines), fit to the data from Joutsuka *et al.*[189] (points). (b) Temperature dependence of $|\chi^{(2)}|$ (lines), fit to the data from Nagata *et al.*[204] (points). The two susceptibility elements have been scaled so that $|\chi^{(2)}/\chi^{(3)}| = 0.09$ at 22°C.[47] Reprinted with permission from Ref. 150. Copyright 2020 American Chemical Society.

the contribution from the less (red) and more (green) acidic sites. The resulting surface potential of the silica–water interface with change of temperature is plotted in Figure 5.8. This model accounts for the shape in the experimental data (Figure 5.6, black line) with a gradual increase in signal until $\approx$ 60°C, followed by a more rapid drop towards 75 °C. We note that, although the surface charge is dominated by the contribution from the less acidic site (red curve in Figure 5.9c), deprotonation at the more acidic site is still required to account for the experimental observation. Excluding the deprotonation of either the

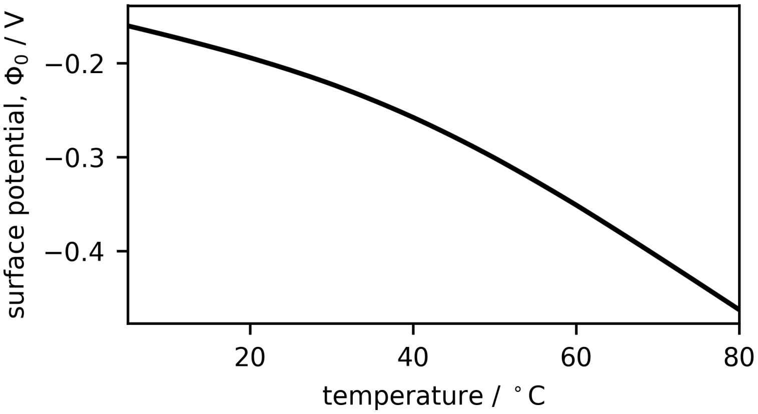

Figure 5.8: Calculated surface potential using a combination of two different silanol sites. Reprinted with permission from Ref. 150. Copyright 2020 American Chemical Society.

more acidic (p$K_{a,2}$ only, red dashed curve in Figure 5.6) or the less acidic (p$K_{a,1}$ only, green dashed curve in Figure 5.6) does not capture the temperature-dependence of the experimental data as well. At this point, we can understand why the intensity initially increases with increasing temperature and then drops. Although the surface charge density monotonically increases with temperature, eventually the decrease of $\chi^{(2)}$ and $\chi^{(3)}$ with increasing temperature dominate the behavior.

A van't Hoff analysis of the temperature-dependence of the two pK_a values using

$$\ln K_a = -\frac{\Delta H}{RT} + \frac{\Delta S}{R} \tag{5.20}$$

results in $\Delta H_1 = 81$ kJ·mol^{-1} and $\Delta S_1 = 165$ J·mol^{-1}K^{-1} for the high acidic site, and $\Delta H_2 = 270$ kJ·mol^{-1} and $\Delta S_1 = 752$ J·mol^{-1}K^{-1} for the low acidic site. Experimental[205] and theoretical[206] studies of gas-phase H_3SiO_4 have determined $\Delta H \approx 1400$ kJ·mol^{-1}, but calculations for condensed phase H_3SiO_4 arrive at a much lower value of $\Delta H =$ 83 kJ·mol^{-1}.[207] Considering a significantly lower level of hydration for silica compared to H_3SiO_4, we consider our values for ΔH_1 and ΔH_2 to be reasonable.

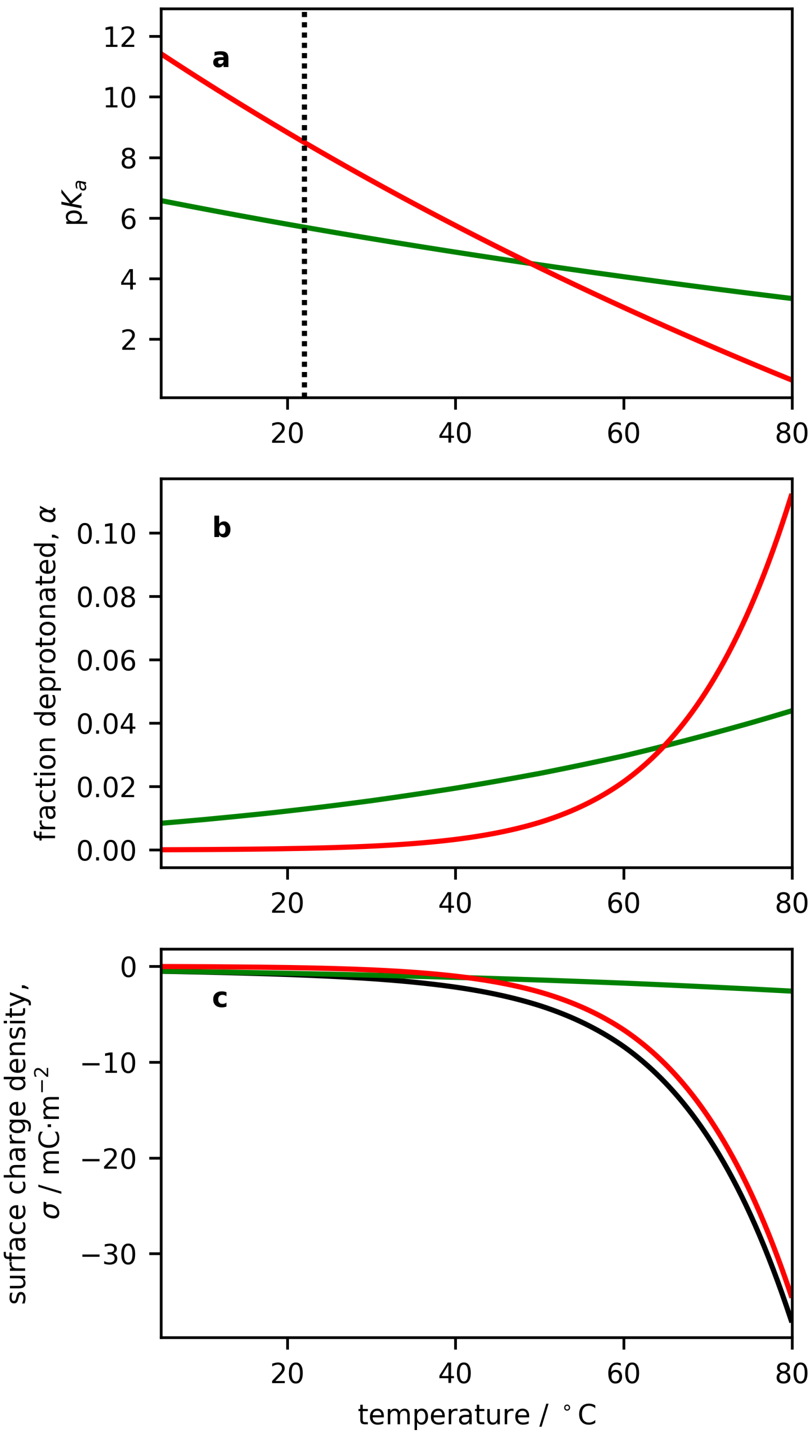

Figure 5.9: (a) Proposed model for how the silica $\mathrm{p}K_{a,1}$ (green curve) and $\mathrm{p}K_{a,2}$ (red curve) change with temperature following Eq. 5.20. (b) The resulting deprotonation of the two silanol sites. (c) Contributions from both sites to the total surface charge density (black curve). Reprinted with permission from Ref. 150. Copyright 2020 American Chemical Society.

5.4.3 Observations in other polarization schemes

Our model considers that there is no significant reorientation for surface-bound water molecules when the temperature increases. We therefore consider that the temperature-dependence of $\chi^{(2)}$ follows solely from the temperature-dependence of the linear optical properties that comprise the hyperpolarizability in the molecular frame.[204] We have chosen to use the SSP results in the modelling, as more quantitative treatment requiring local field correction of the SSP data is possible on account of the single $\chi^{(2)}$ tensor element ($\chi^{(2)}_{yyz}$) that contributes to SSP signals. To further investigate this point, we have performed measurements in the PPP polarization scheme (all beams p-polarized). As seen in Figure 5.10, the PPP trend is very similar to our SSP results. This indicates that there is no significant reorientation of water molecules with temperature, validating our premise that $\chi^{(3)}$ is a more significant contributor to the intensity trend.

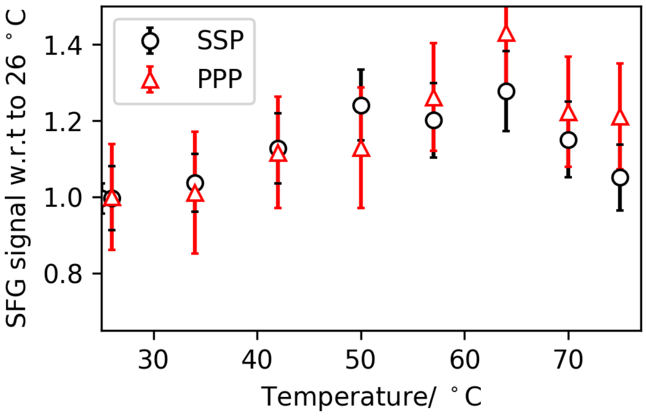

Figure 5.10: SSP (circles) and PPP (triangles) intensity at 3180 cm^{-1} plotted together as a function of temperature. Reprinted with permission from Ref. 150. Copyright 2020 American Chemical Society.

5.4.4 Reversibility

In order to investigate the reversibility of the change with temperature, we have cycled the temperature between 30–60 °C, with one cycle of the data displayed in Figure 5.11. We see that the same SFG signal was observed after heating and cooling. This indicates that dissolution of silica is an insignificant contribution to the surface environment during this short time frame.

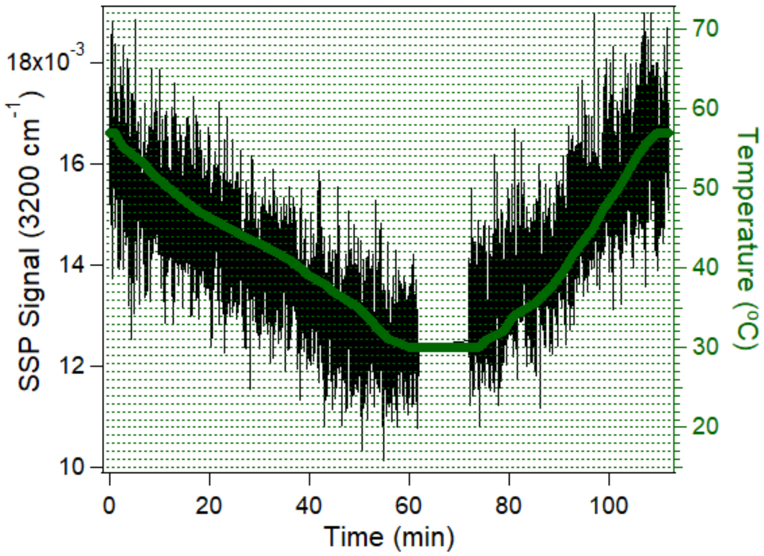

Figure 5.11: One cycle of a temperature ramp experiment in which the temperature was cycled between 30–60 °C. The SFG signal is plotted with respect to time on the left axis, and the corresponding temperature is shown on the right axis. Reprinted with permission from Ref. 150. Copyright 2020 American Chemical Society.

5.5 Conclusion

Our probe of interfacial water molecules has resulted in evidence and a quantitative description of the silica surface charge increase with temperature. We also provide values of the thermodynamic constants associated with the deprotonation of two different silanol sites. We have used a model for the silica surface potential that was recently developed using data from multiple angle-of-incidence experiments, and have extended it to temperature-dependent studies. It will be important to further develop this model and its associated parameters through experiments that can provide additional insight into the water structure and surface silanol groups. For example, isotopic dilution studies, phase-resolved measurements, and experiments with varying solution pH and ionic strength. Temperature-dependent surface charge and thermodynamic parameters are important for the development of silica-based catalysts and biosensors that operate over a wide range of temperatures,[22, 208, 209] and new silica-based drug carriers with temperature-controlled release mechanisms.[210, 211]

Chapter 6

Silicone Surface Charge Enhancement due to Ion Adsorption[*]

6.1 Introduction

Polymer materials, especially silicone materials like PDMS have been the most common base material for microfluidics devices such as micro-total analysis systems (μ-TAS), offering several advantages compared to traditional glass- and silicon-based devices such as ease of fabrication, physical properties, and low cost.[212–214] Knowledge of the electro-osmotic characteristics such as the surface potential of PDMS substrates is critical for the design and operation of these systems.[15] The zeta potential of PDMS surfaces have historically been obtained by current monitoring,[215,216] amperometric detection methods,[217] and atomic force microscopy,[218] etc. However the surface potential of PDMS remains hard to obtain. Moreover, it is common to use methods such as UV irradiation and plasma treatment to enhance the surface charge of PDMS.[13] It was found that after such treatments, the PDMS surface would have a silica-like surface, with methyl groups replaced by hydroxyl groups. But on native or "untreated" PDMS surface there was no sign of silica-like structures.[219] Also, the source of surface charge on native PDMS surface is still not well-understood.[220]

Nonlinear optics is an emerging technique for quantifying the surface charge on

---

[*] All data collection, including preparation of polymer surfaces and solutions, and measurement of SFG spectra performed by Azam. Treatment of data, model development, and analysis of data done by Cai.

aqueous interfaces. Nonlinear optical techniques have been successfully employed to measure the surface charge of various charged systems such as silica–water,[47,150,221] air–water,[45,46,222] and lipid–water[223] interfaces. The non-linear response of water from charged aqueous interfaces has contributions from the surface-bound water molecules ($\chi^{(2)}$) and water molecules in the bulk ($\chi^{(3)}$). The challenge is to deconvolute these contributions and interpret the nonlinear response correctly. Various attempts to model the contributions from the two sources have been made[43–45,47] and it was demonstrated that the $\chi^{(3)}$ contribution is modulated by a function of the DC field and the wavevector mismatch factors. It was also shown that it is more appropriate to use the full solution of the Poisson–Boltzmann equation when obtaining the DC field, instead of the linear approximation, to make it applicable for low ionic strength and high surface potential cases, resulting in a function called $g3$:

$$I \propto |LLL|^2 |\chi^{(2)} + g_3 \chi^{(3)}|^2, \tag{6.1}$$

where

$$g_3 = \Phi_0 - \frac{4ikT\Delta k}{e} \sum_{n=1}^{\infty} \frac{\xi^{2n-1}}{(2n-1)[i\Delta k - \kappa(2n-1)]} \tag{6.2}$$

and

$$\xi = \tanh\left[\frac{e\Phi_0}{4kT}\right].$$

Here e is the electron charge, k is Boltzmann's constant, T is the absolute temperature, and L are the local field corrections. Details and derivation of the Equation 6.2 can be found in Chapter 1.

In this work we use SFG spectroscopy to monitor the water -OH signal of the PDMS–water interface at various ionic strengths. The SFG spectra were taken with different angles of incidence, to provide angle-dependent data for deconvoluting the bulk and interfacial contribution of nonlinear response. The resulting data serves to quantify the surface potential of a native PDMS surface in water and provide insights into the origin of surface charge on PDMS–aqueous interface and the ion adsorption process on PDMS surfaces.

6.2 Experimental

6.2.1 Polymer film preparation

Polydimethylsiloxane (PDMS) solution was prepared from a Sylgard 184 silicone elastomer kit (DowCorning). Part A (the PDMS base) and Part B (curing agent) were dissolved in chloroform (5% w/w) and mixed with a ratio of 10:1 (A:B). The substrate was a IR-grade fused silica hemi-cylindrical prism (Quartz Plus, Brookline, NH) with a radius of 12.5 mm. Before spin-coating the substrate were cleaned in piranha solution (3:1 mixture of H_2SO_4 and 30% H_2O_2) to remove any organic on the surface. After that it was washed with 18.2 MΩ·cm deionized water, and dried in oven at 100 °C for 1 h under vacuum. When dried, the flat side of fused silica was spin-coated with the PDMS mixture in chloroform using a spin-coater (Specialty Coating Systems, Inc. IN, USA) at 4000 rpm for 5 min. Finally, the PDMS coated prism were sent to a 85 °C oven for 4 h under vacuum to cure the PDMS surface.

6.2.2 Acquisition of SFG spectra

The laser system used for SFG spectroscopy has been reported previously.[70] In brief, a Nd:YAG laser (Ekspla PL2241A) generates a 30 ps pulses with a repetition rate of 10 Hz at 1064 nm (fundamental) and another at 532 nm (second harmonic). These two lasers pump an optical parametric generator (Ekspla PG501) to produce tunable IR frequencies in the range of 2700–3700 cm^{-1}. The IR laser together with a portion of the 532 nm visible output are incident through the prism and on the PDMS surface. The prism were pressed against a custom made Teflon cell[70] with an opening, exposing to water in the 10 mL reservoir in the cell. The opening on the Teflon cell and the PDMS surface were sealed with a fluoropolymer O-ring (Marco Rubber, NH). The cell and the detector were mounted on two concentric computer-controlled motorized rotation stages that allows the sample and detector to be rotated and thus changing the angles of incident for the lasers. The angle of incident for the IR laser was set to be 9.8° higher than that of the visible laser. The reservoir were filled with salt solution with ionic strength of 10^{-5} M, 10^{-4} M, 10^{-3} M, and 10^{-2} M. The salt solution were made by dissolving NaCl (Sigma-Aldrich, MI, USA) in Milli-Q water. The SFG spectra were taken with angles of incidence at 64°, 65°, 67°, 69°, and 70° in each solution and pure Milli-Q water. The local field correction factors were calculated using the method described in Chapter 1 and 2. Since there is no -OH functional group on the PDMS–prism side, only the factors where $z = d$ where considered.

6.3 Results and Discussion

6.3.1 Surface charge density variation with ionic strength

The SFG spectra of PDMS–water interface under different ionic strengths and angles of incidence were presented in Figure 6.1. The intensities at 3200 cm^{-1} was extracted from the spectra (Figure 6.3, coloured dots) at each angle of incidence and ionic strength. The wavenumber was chosen based on the peak of OH stretching band in previous study.[47] It was observed that the signal increases with ionic strength first, plateaus at 10^{-5} M (10^{-6} M for angle of incidence of 67°), and starts to drop drastically. The local field corrected SFG intensities are shown in Figure 6.2. This is evidence that the native PDMS surface is charged, since only $\chi^{(2)}$ contributes to the nonlinear response for an uncharged surface, and the only angle-dependent term would be the local field factors. Here after local field correction the SFG intensities still shows angle dependence, and it must be contributed from the $g_3\chi^{(3)}$ term.

The wave-vector mismatch in Equations 6.1 and 6.2 can be calculated. The surface potential Φ_0 can be derived from surface charge density (σ), which is the parameter of interest, using the Grahame equation

$$\Phi_0 = \frac{2k_BT}{e}\sinh^{-1}\left(\frac{\sigma}{\sqrt{8c_0\varepsilon\varepsilon_0 k_BT}}\right). \tag{6.3}$$

Therefore, to model the system and obtain the surface potential, we must obtain the complex value of $\chi^{(2)}$ and $\chi^{(3)}$. Since the data comes from a homodyne SFG experiment

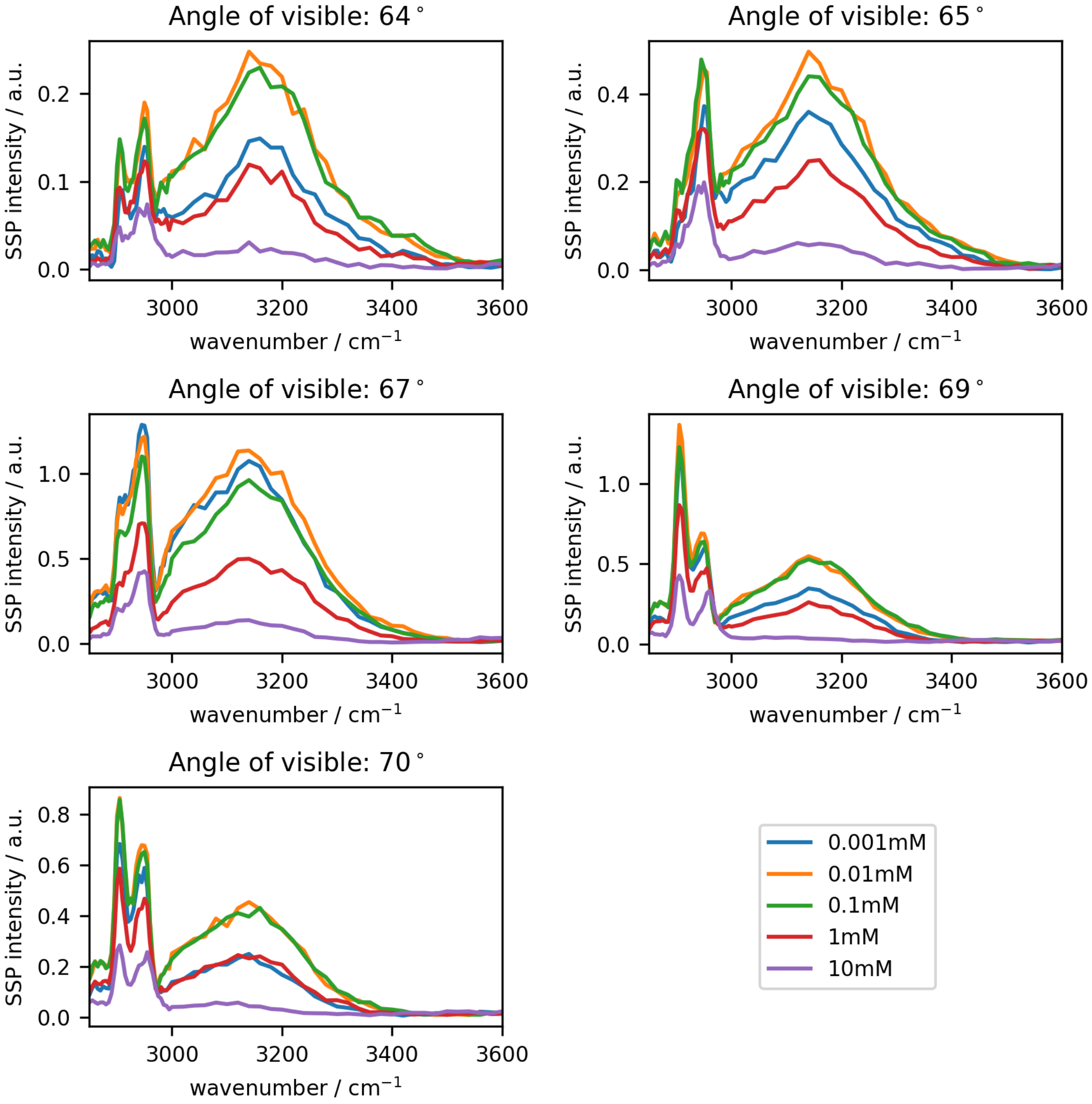

Figure 6.1: SSP spectra of the PDMS–water interface under different ionic strengths and angles of incidence.

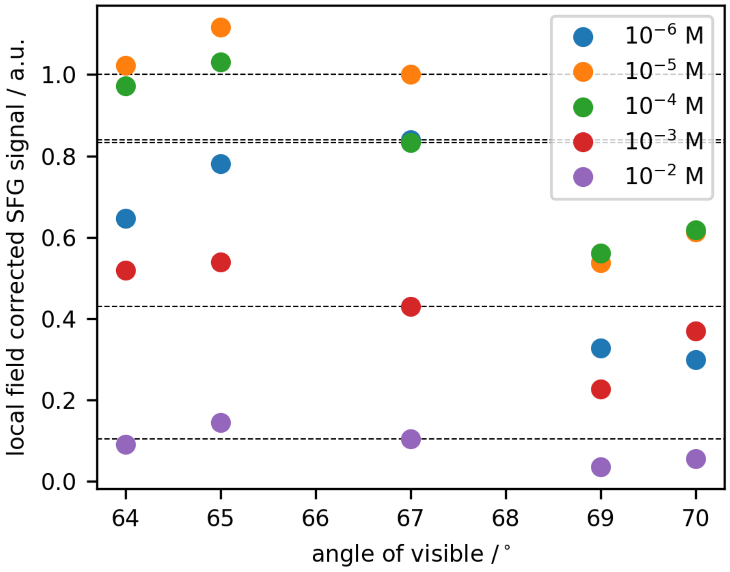

Figure 6.2: Local field corrected SFG signal (coloured dots). Each color represents signal at one ionic strength. The horizontal dashed lines are for visual reference.

and without absolute units, we rewrite Equation 6.1 as

$$I \propto |LLL|^2 \left[|R|^2 + |g_3|^2 + 2|R||g_3| \cos(\phi_2 - \phi_3 - \phi_g) \right] . \tag{6.4}$$

Here $R = |\chi^{(2)}||\chi^{(3)}|$, ϕ_2 and ϕ_3 are the phase of $\chi^{(2)}$ and $\chi^{(3)}$, and ϕ_g is the phase of g_3. It has been demonstrated that $\chi^{(3)}$ is a bulk feature of water and the complex $\chi^{(3)}$ with IR wavenumber dependence has been published.[45] Therefore ϕ_3 can be extracted from literature,[45] and only R and ϕ_2 need to be discovered. First we consider if the changes in signal can be explained with a constant surface charge density and R value. Figure 6.3a shows the fitted SFG intensity with the optimized values $\sigma = -0.12$ C·m^{-2} and $R = 0.038$. The phase difference between $\chi^{(2)}$ and $\chi^{(3)}$ ($\Delta\phi = \phi_2 - \phi_3$) was set to be 0°, 90°, 180°, or 270°. Based on the quality of fitting 180° was used as the phase difference. As shown in Figure 6.3, even though the fitted intensity matches some of the features in the SFG intensity change with ionic strength and angle of incidence, it deviates from the experimental data significantly in the lower and highest ionic strength region. This indicates that the surface charge density must be changing with ionic strength.

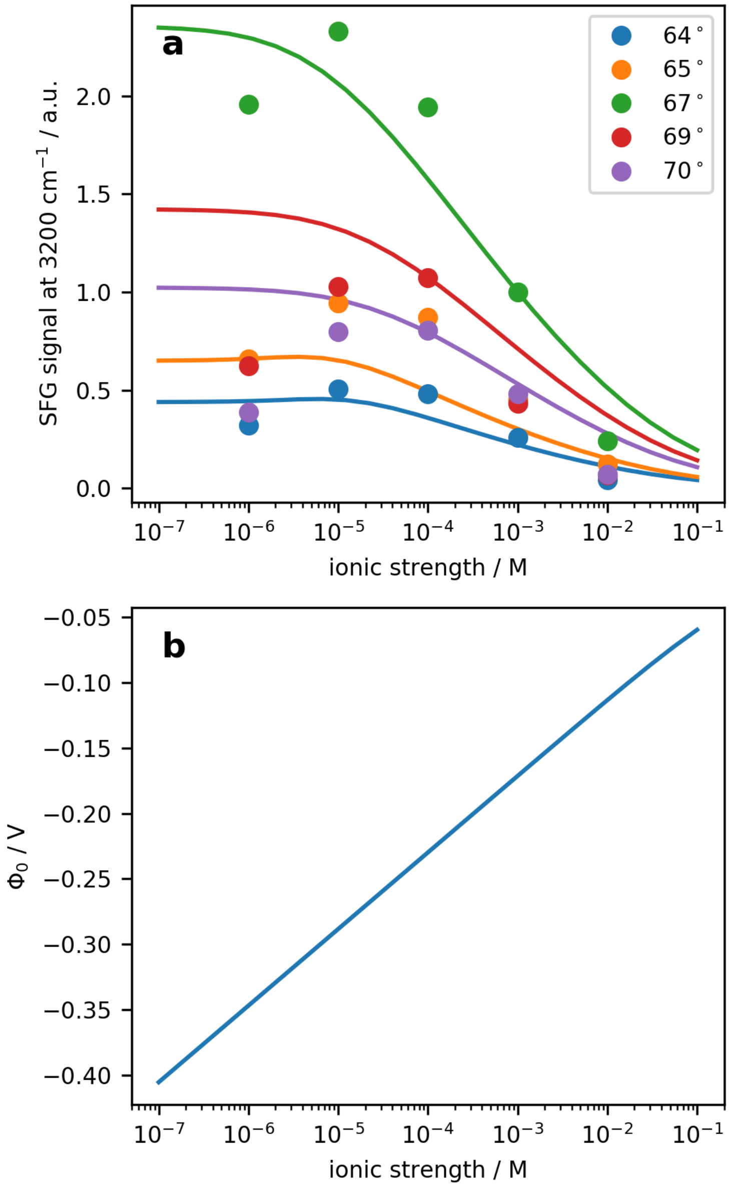

Figure 6.3: a) Experimental (coloured dots) and fitted (curves) SFG intensity at 3200 cm^{-1} with ionic strength from 10^{-6} M to 10^{-2} M and angle of incidence from 64° – 70°. The PDMS surface were assumed to have a constant surface charge density (σ) and R. All normalized to the intensity with 67° visible angle of incidence and 10^{-3} M ionic strength. b) Calculated surface potential from the fitted surface charge density.

6.3.2 Ion adsorption models

There has been speculation that the surface charge of PDMS surface comes from impurities, specifically silica fillers. However, ATR-IR spectroscopy studies of the same kind of PDMS material (Sylgard 184) shows no sign of -OH stretches, indicating that there cannot be a high concentration of silanol groups on the surface.[224] It was also found that silica fillers were buried under the surface for native surface and there are no silica-like structures found on native PDMS using surface energy and Near-Edge X-Ray Absorption Fine Structure measurements.[219] With no or very few available deprotonation sites on the PDMS surface, it is reasonable to assume the surface charge comes from specific adsorption of ions.[220] Previous vibrational spectroscopy studies[225–229] and molecular dynamics simulation studies[229,230] suggest that at there are strong preferential ion adsorption on hydrophobe–water interfaces. It was found that anions have affinity to such interfaces, while cations are repelled from the interfaces and generates a negative surface charge. To model the ionic adsorption process, we first consider a Langmuir isotherm,

$$q = Q\frac{bC}{1+bC} \tag{6.5}$$

with

$$b = \frac{K_a}{K_d}.$$

Here q is the surface ion density in mol·m^{-2}, Q is the adsorption capacity, C is the bulk ion concentration in mol·m^{-3}, and b is the ratio of the adsorption rate constant (K_a) over the desorption rate constant (K_d). The surface ion density will be used to calculate the surface charge density (σ),

$$\sigma = -|e|q \times N_A \tag{6.6}$$

where e is the elementary charge, and N_A is Avogadro's number. The value of b, Q, R and $\Delta\phi$ were optimized based on the residual values of experimental and calculated SFG intensities. The phase difference was again found to be 180°. Figure 6.4a shows the fitted SFG intensities. Similar to the result with a constant σ, the model does not fully capture the "turn-over" behaviour presented in the experimental result. The Langmuir isotherm considers the adsorption sites to be homogeneous, and the adsorption energy does not change with degree of surface coverage.[231] A poor fit to the Langmuir model may suggest that the adsorption sites on the PDMS surface are heterogeneous and the adsorption energy changes with increasing ion adsorption. To further investigate the ion adsorption behavior on PDMS surface, a Freundlich isotherm was used to fit the data. The Freundlich isotherm is a purely empirical model with the assumption of a heterogeneous adsorbing process. It may be used to model systems where the adsorption energy increases or decreases exponentially, or does not change with surface ion concentration. It is considered to be appropriate for the adsorption of small molecules and heavy metal ions on polymers.[232,233] The model can be written as

$$q = KC^N, \tag{6.7}$$

where q is the surface density of ions in mol·m^{-2}, C is the bulk concentration of ions in mol·m^{-3}, K is the Freundlich constant unique to each system at a certain temperature in mol^{-N+1}·m^{3N-2}. When $N > 1$ the adsorption energy increases with increasing surface concentration, and when $N < 1$ the adsorption energy decreases with increasing surface concentration. The fitted result is shown in Figure 6.5, with $R = 0.009$, $K = 5.03 \times 10^{-8}$ and $N = 0.197$. Since the R value is low, most contribution comes from the $g_3\chi^{(3)}$ term, so the fitted result is not sensitive to the phase difference between $\chi^{(2)}$ and $\chi^{(3)}$. The fitting result shows that the surface charge density of the PDMS increased from -0.002 C·m^{-2} to -0.012 C·m^{-2}, and the surface potential dropped from -0.16 V to -0.02 V. The resulting $N < 1$, suggests that the adsorption energy decreases with increasing surface density. This means that the adsorption stability would decrease with increasing surface density, so the adsorption rate will decrease.

A comparison of the measured zeta potential of PDMS (obtained from Refs. 218, 216, and 215) and deduced surface potential were presented in Figure 6.5b. The deduced surface potential was found to be between two sets of literature values for zeta potentials on PDMS–

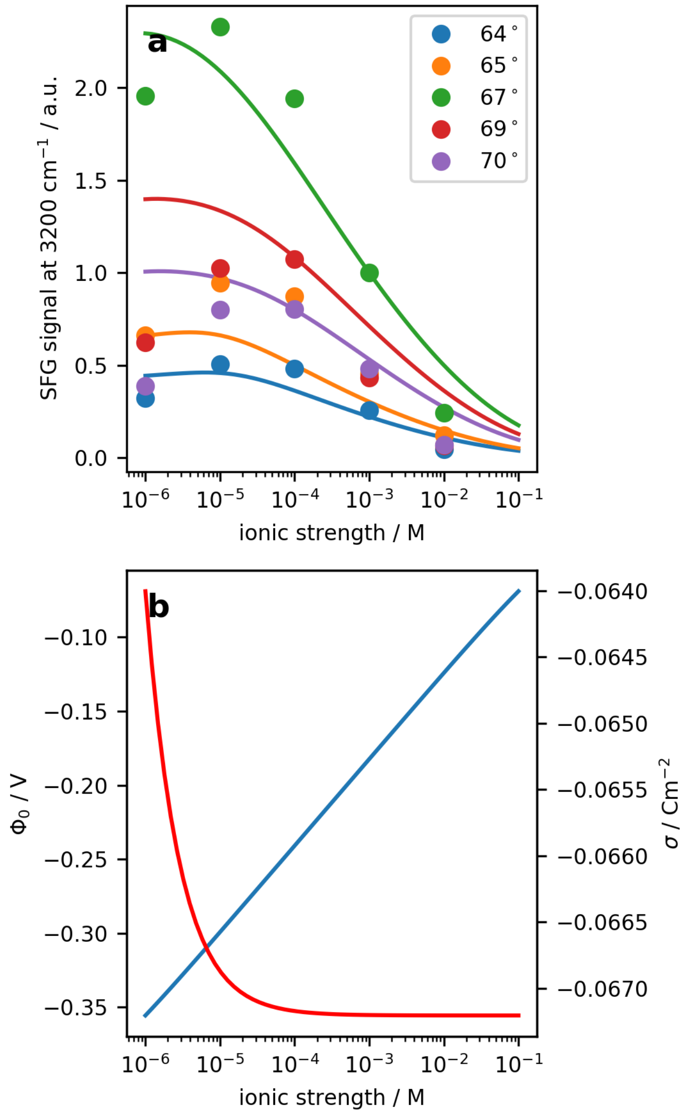

Figure 6.4: a) Experimental (coloured dots) and fitted (curves) SFG intensity at 3200 cm^{-1} with ionic strength from 10^{-6} M to 10^{-2} M and angle of incidence from 64° – 70°. The surface density were obtained from the fitted surface ion density using Langmuir isotherm. All normalized to the intensity with 67° visible angle of incidence and 10^{-3} M ionic strength. b) Calculated surface potential (blue curve) from the fitted surface charge density (red curve).

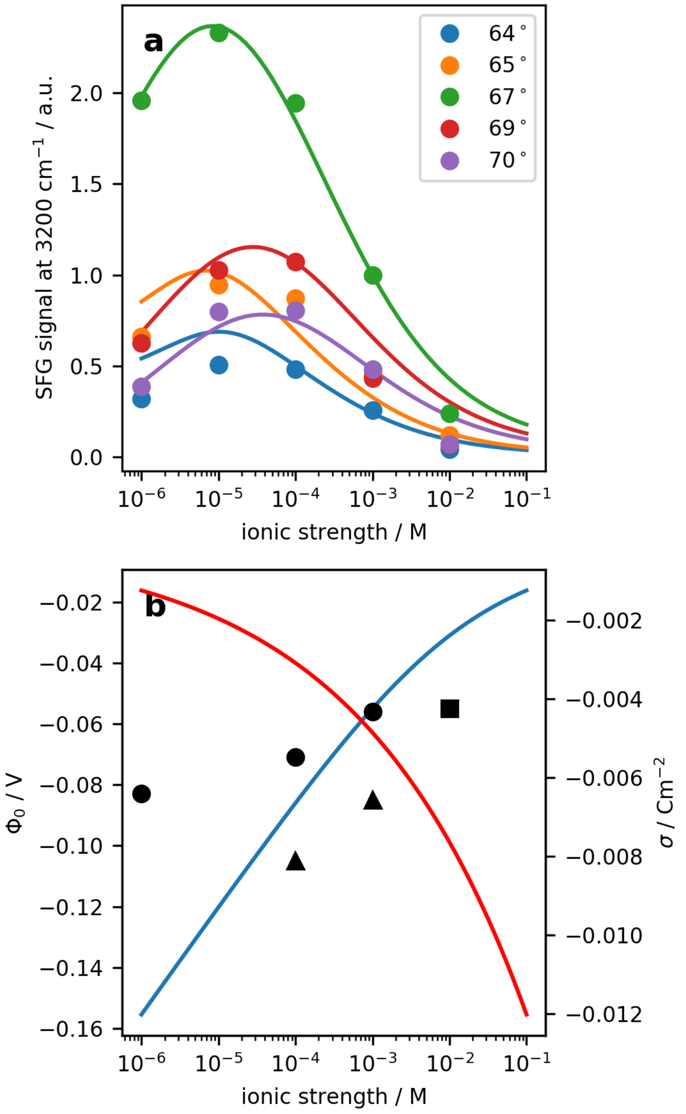

Figure 6.5: a) Experimental (coloured dots) and fitted (curves) SFG intensity at 3200 cm^{-1} with ionic strength from 10^{-6} M to 10^{-2} M and angle of incidence from 64° – 70°. The surface density were obtained from the fitted surface ion density using Freundlich isotherm. All normalized to the intensity with 67° visible angle of incidence and 10^{-3} M ionic strength. b) Calculated surface potential (blue curve) from the fitted surface charge density (red curve) and measured zeta potential of PDMS surface from Ref. 218 (circles), Ref. 216 (square), and Ref. 215 (triangles).

water interface. The surface potential should be equal to or larger than the zeta potential, as the definition of zeta potential is the electrical potential between the slipping plane and the bulk, and it is further away from the surface. The surface potential for PDMS in water could depend on the degree of cross-linking of the polymer, temperature, and types of ions in the solution, etc. As the measured zeta potential and surface potential are close, it suggests that the Stern layer is negligible. Comparing the obtained surface charge density of PDMS–aqueous interface to that of the silica–aqueous interface,[47] we found that the surface change density is 20% to 50% of that of the silica–aqueous interface. Since the silica surface charge is proportional to the surface silanol number density, if the surface charge of PDMS was originated from the silica fillers, it means that silanol number density on PDMS surface would be 20% to 50% that of silica surfaces. This is unlikely, as spectroscopic results indicate no or very few silanol groups or silica-like structures on native PDMS surface.[219,224]

Finally the ion species in the ion adsorption process should be discussed. In the experiment presented here, chloride ions from sodium chloride, hydroxide ion from autoionization of water, and bicarbonate from dissolved carbon dioxide are expected in the solution. It was demonstrated that larger ions have a higher affinity to hydrophobe surfaces,[227,230] and the concentration of chloride ion is higher than the other two except in pure milli-Q water, so the majority of the adsorbed ions should be chloride ions in those cases. However, the actual proportion would need further investigation. Nevertheless, no ion specific parameters was used in the models, so the ion adsorption process could be seen as a combined effect from all the monovalent ions.

6.4 Conclusion

In this work we first presented spectroscopic evidence that the native PDMS surface is charged in water. We have quantified the surface charge of PDMS as a function of ionic strength by probing the nonlinear response of water with multiple angles of incidence. The surface charge density of the PDMS in water was found to be varying from -0.002 C·m^{-2} to -0.012 C·m^{-2}, resulting in a surface potential of -0.16 V to -0.04 V when ionic strength increased from 10^{-6} M to 10^{-4} M. We proposed a Freundlich adsorption isotherm to describe the ion adsorption and charging process of the PDMS–aqueous interface. The ion adsorption energy was also found to be decreasing when ion adsorption density increases, leading to a less stable adsorption. These results provide evidence that the surface of PDMS in water could be charged by adsorption of anions like chloride ions in the solution to the PDMS surface. The findings presented in this work would be important for the design and operation of microfluidic devices, and provide insight into measuring the surface charge of other polymer materials.

Chapter 7

Examining Prospects for Model-Free Determination of Surface Potential using Nonlinear Optics

7.1 Introduction

Understanding the molecular structures at charged interfaces is of great importance to most biological and chemical systems. With various surface-specific reactions including hydrogen bonding, electrostatic and van der Waals interactions, the interfacial properties has been explored by scientists across many disciplines. This interfacial region is also known as 'the bonded interface layer' (BIL), which requires experimental techniques with highly sensitive surface-selective measurements. In the past decades, SHG and SFG technique have been established to provide *in situ* measurements directly next to the bulk aqueous phase, which is named as 'the diffuse layer' (DL).[45]

At charged aqueous interfaces, the optical signal response of water are generated from two sources, which are the second-order at the BIL and the electric-field-induced third-order responses from the DL. In more recent studies, the main challenge is to separate the relative contribution of these two factors. One solution to this was firstly proposed by Wen *et al.*[45] by using phase-sensitive SFG on a lipid-aqueous model. Another solution proposed by Ohno *et al.*[221] was to use a Heterodyne-Detected Second Harmonic Generation (HD-SHG) and it is capable of deconvolute the second- and third-order contribution to the SHG signal directly. Hore and Tyrode[47] also presented a method to interpret the SFG signal from charged silica/water interface with a deprotonation model of the silica surface. In this chapter we will present these methods and their applications in different systems. We would also present an universal method for interpreting the non-linear response from charged aqueous interfaces and derive the surface potential and/or surface charge density by modulating the coherence length.

7.2 Background

7.2.1 Charged Aqueous Interfaces

A host of fundamentally important processes including environmental, biological, atmospheric, and geochemical applications that take place at charged aqueous interfaces are governed by electrostatic interactions within the electrical double layer (EDL). The EDL refers to the two parallel layers formed due to the accumulation of the counter ions on charged surfaces and therefore depends on the surface charge density, surface potential, and the bulk ionic strength. Quantitative characterization of the EDL has, therefore, been an immense interest of the materials and surface scientists. Evaluation of the electrostatic potential at the slipping plane of the EDL, referred as zeta potential, is possible with the help of electrokinetic measurements but the uncertainty in the position of the slipping plane itself in an aqueous environment makes this less useful. On the other hand, potentiometric titration can estimate the surface charge density assuming only a particular reactions takes place at the solid/aqueous interface of interest.

Owing to the inherent surface specificity, nonlinear optical (NLO) spectroscopic techniques such as second-harmonic generation (SHG) and vibrational sum-frequency generation (SFG) are well capable of probing the aqueous interfaces at various conditions. The measured electric field via this techniques is proportional to the sum of two contributions—one from the water monolayers at the bonded interface layer (BIL) where the inversion symmetry is broken, and the other one from the reorientation and polarization of water molecules in the EDL in response to the static electric field generated by the surface charge. Although the NLO signal depends on the surface potential, the quantification of this surface property is not possible because of the inability to separate these two contributions from the BIL and EDL. Penetration of the surface electric field into the aqueous bulk depends on the electrostatic screening caused by the co-ions at the adjacent aqueous layer. Based on this ionic strength dependence of the potential drop across the diffuse layer, the Gouy-Chapman model of the electric double layer can be employed to describe the electric potential of the charged microparticle interface.

7.2.2 Relationship between measured signals and the surface potential

The nonlinear optics response from a charged aqueous interface can be expressed as

$$E_{\text{sig}} = \chi^{(2)}_{\text{BIL}} + \chi^{(2)}_{\text{EDL}}, \tag{7.1}$$

where $\chi^{(2)}_{\text{BIL}}$ is the nonlinear response from the interfacial binding layer while $\chi^{(2)}_{\text{EDL}}$ comes from the electrical double layer. The term $\chi^{(2)}_{\text{EDL}}$ is related to the third-order bulk nonlinear susceptibility of water, $\chi^{(3)}$. Different models describing the relative contribution from $\chi^{(2)}_{\text{BIL}}$ and $\chi^{(2)}_{\text{EDL}}$ have been presented in Section 1.3.2, here a brief summary is provided. Eisenthal[43] first proposed that

$$\chi^{(2)}_{\text{EDL}} = \Phi_0 \chi^{(3)}. \tag{7.2}$$

However it does not consider the z-dependence of the incoming beams, which is not valid in most cases. By incorporating the z-dependence of the incoming beams, Roke and Tian[44,45] introduced,

$$\chi^{(2)}_{\text{EDL}} = f_3 \Phi_0 \chi^{(3)}, \tag{7.3}$$

and later redefined[47] as

$$\chi^{(2)}_{\text{EDL}} = g_3 \chi^{(3)}. \tag{7.4}$$

Here $f_3\Phi_0$ and g_3 are the terms modulating $\chi^{(3)}$, they come from two different solutions for the Poisson-Boltzmann equation in the Gouy Chapman theory. When using the linearized solution,

$$f_3 = \frac{\kappa}{\kappa - i\Delta k_z}. \tag{7.5}$$

Here Δk_z is the wave-vector mismatch along z defined in Equation 1.25 and κ is the Debye length defined in Equation 1.17. The solution with notation of g_3 was proposed by Hore and Tyrode.[47] Under higher surface potential the linearized Gouy Chapman model breaks down and the solution of $\Phi(z) = \Phi_0 e^{-\kappa z}$ no longer depicts the actual physics of the system. When the full solution from the Poisson-Boltzmann equation is applied,

$$g_3 = \Phi_0 - \frac{4ikT\Delta k}{e} \sum_{n=1}^{\infty} \frac{\xi^{2n-1}}{(2n-1)[i\Delta k - \kappa(2n-1)]}, \tag{7.6}$$

with $\xi = \tanh[e\Phi_0/4kT]$. There are two ways to obtain the surface potential of an interface with non-linear optics, off-resonance (typically the case in electronic SHG, and less commonly in the case of vibrational SFG) or on-resonance (possible with electronic SHG, and most common in case of probing the water band on vibrational resonance near 3200 cm^{-1} in SFG). As will be discussed in detail below, off-resonance methods are able to readily deduce the surface potential.[46,221,223] However, it is challenging to separate the $\chi^{(2)}$ contributions from different sources if species other than water are contributing. Control experiments therefore need to be done in order to establish the origin of the signals. On-resonance methods provide the specificity of water molecules,[45,47,150] but so far rely on prior knowledge such as silica deprotonation models in order to connect to the surface potential.

7.3 Off-resonance methods

7.3.1 Phase-resolved options

Ohno *et al.*[221] first used a phase-resolved second harmonic generation to measure the surface potential of silica/water interface. Eqs 7.1 and 7.3 can be written with φ_3 as the phase angle of f_3,

$$E_{\text{SHG}} \propto \chi^{(2)}_{\text{BIL}} + \chi^{(3)} \Phi_0 \cos(\varphi) e^{i\varphi_3} \tag{7.7}$$

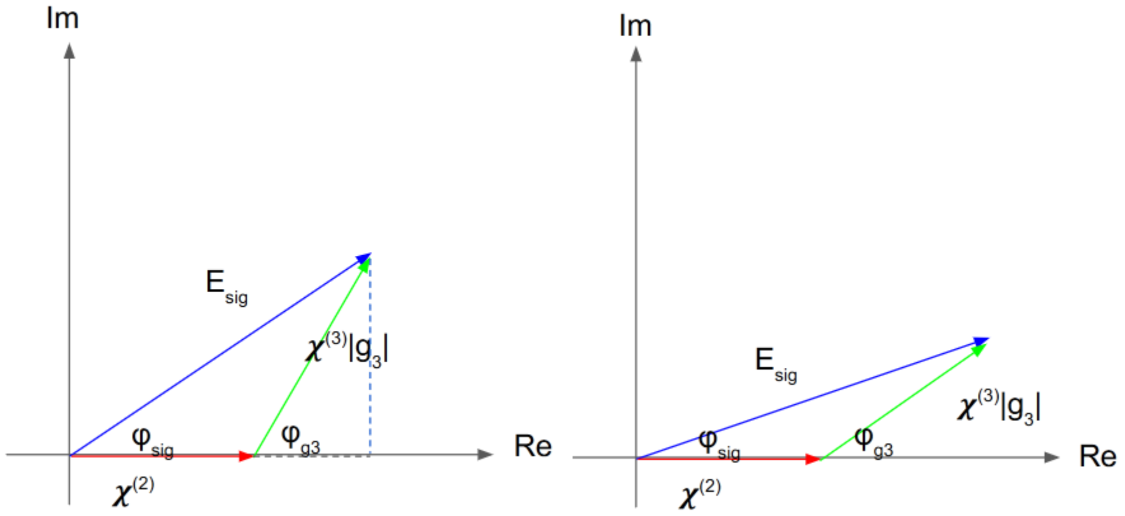

Figure 7.1: A graphical representation of the relationship between $\chi^{(2)}$, $\chi^{(3)}$, and the measured signal in off-resonance experiments. The two graphs represent two scenarios with different coherence length. Note that $\chi^{(2)}$ and $\chi^{(3)}$ does not change with the coherence length and only g_3 is changing.

and

$$\varphi_3 = \arctan(\Delta k_z \lambda_D). \tag{7.8}$$

To visualize the relative contribution to the overall signal, the argon diagram originally purposed by Ohno *et al.*[221] would be similar to Figure 7.1a, except with $g_3 \approx f_3\Phi_0$. The phase of f_3 can be calculated with the reciprocal Debye length and the phase mismatching. Debye length can be obtained from the ionic strength of the solution, and the phase mismatching in the SHG process can also be calculated. Phase-resolved SHG measurement will give the phase (φ_{sig}) and the magnitude (E_{sig}) of the SHG signal, therefore one will be able to solve for $\chi^{(3)}\Phi_0$ and $\chi^{(2)}_{\text{BIL}}$ directly using trigonometry,

$$\chi^{(3)}\Phi_0 = \frac{\sin(\varphi_{\text{SHG}})E_{\text{SHG}}}{\cos(\varphi_3)\sin(\varphi_3)} \tag{7.9a}$$

$$\chi^{(2)}_{\text{BIL}} = \cos(\varphi_{\text{sig}})E_{\text{sig}} - \cos^2(\varphi_3)\chi^{(3)}\Phi_0 \tag{7.9b}$$

To further separate the surface potential (Φ_0), the authors made several measurements under different ionic strengths. Since $\chi^{(3)}$ is a bulk water feature, it is invariant under ionic strength for up to 100 mM ionic strength,[189] thus all changes in the $f_3\Phi_0\chi^{(3)}$ comes from

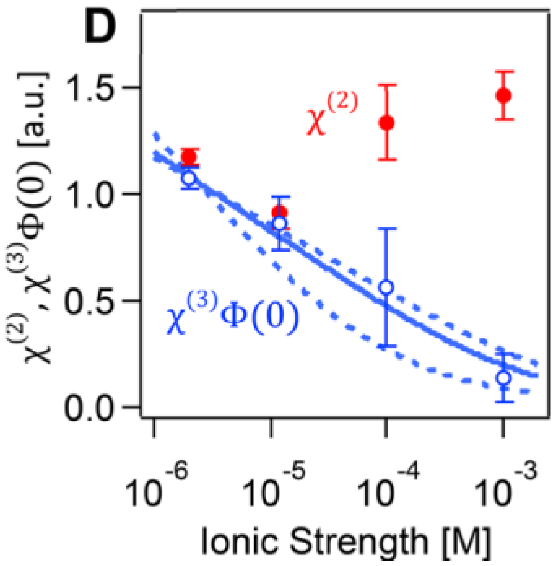

Figure 7.2: Deduce $\chi^{(2)}$ and $\chi^{(3)}\Phi_0$ value from each ionic strength. The solid line is $\chi^{(3)}\Phi_0$ calculated with Gouy Chapman theory with a surface charge density of $\sigma = -0.0024(18)$ C·m^{-2}. Reproduced from ref 221. Copyright 2019 American Chemical Society.

$f_3\Phi_0$. Relying on the Gouy-Chapman theory, $\chi^{(3)}$ and the surface charge density (σ) can be obtained, and Φ_0 under each ionic strength can be calculated (result shown in Figure 7.2).

Dalstein, Chiang, and Wen[46] also used Heterodyne-Detected Second Harmonic Generation to deduce charged water interface. Equation 7.1 & 7.3 can be expressed in real and imaginary parts,

$$\mathbb{R}\mathrm{e}\{E_{\mathrm{SHG}}\} = \chi^{(2)}_{\mathrm{BIL}} + \mathbb{R}\mathrm{e}\{\chi^{(2)}_{\mathrm{EDL}}\} = \chi^{(2)}_{\mathrm{BIL}} + \chi^{(3)} \cdot \mathbb{R}\mathrm{e}\{\Psi\} \tag{7.10a}$$

$$\mathbb{I}\mathrm{m}\{E_{\mathrm{SHG}}\} = \mathbb{I}\mathrm{m}\{\chi^{(2)}_{\mathrm{EDL}}\} = \chi^{(3)} \cdot \mathbb{I}\mathrm{m}\{\Psi\} \tag{7.10b}$$

Here $\Psi = \Phi_0 f_3$. When off resonance, $\chi^{(2)}_{\mathrm{BIL}}$ is always real, so the imaginary part of the SHG signal comes solely from $\chi^{(2)}_{\mathrm{EDL}}$.

The authors first studied a monolayer of lignoceric acid on water. This system has been studied and the relationship between the pH and deprotonation, consequently the surface charge density (σ) has been established. With this information the authors were able to extract the value of $\chi^{(3)}$ in MKS units. The obtained $\chi^{(3)}$ values are independent of the surface charge and their phases are close to zero, confirming that $\chi^{(3)}$ is a bulk water feature and is real when off-resonance. With the information of $\chi^{(3)}$ the authors were able to study other systems using equation 7.10.

At high surface potential, it is more accurate to use g_3 to solve for Φ_0 (as discussed previously). Figure 7.3 shows the phase of g_3 and $\Phi_0 f_3$ in different ionic strengths as a function of the surface potential. It exhibits one key difference between the g_3 and f_3, which is that the phase of g_3 is Φ_0 dependent. This unique feature of g_3 makes it impossible to separate $\chi^{(2)}_{\mathrm{BIL}}$ and $\chi^{(2)}_{\mathrm{DL}}$ directly from one phase resolved measurement when off-resonance without the surface potential. However it provides the possibility to deduce the surface potential with two or more phase resolved measurements in one ionic strength, without using the Gouy-Chapman theory to separate Φ_0 and f_3 terms. Furthermore it can be done in both off- or on-resonance experiments, as will be demonstrated in the rest of the paper. The expression of Heterodyne-Detected Second Harmonic Generation signal was shown in Eqns. 7.1 and 7.4. Since $\chi^{(3)}$ is a bulk water feature and remains constant, we can define $R = \chi^{(2)}/\chi^{(3)}$,

$$E_{\mathrm{SHG}} \propto R + g_3. \tag{7.11}$$

Here R is real and g_3 is complex, from trigonometry we find that,

$$\tan(\varphi_{\mathrm{sig}}) = \frac{\mathbb{I}\mathrm{m}\{g_3\}}{R + \mathbb{R}\mathrm{e}\{g_3\}}. \tag{7.12}$$

It is also worth noting that from the phase of the SHG field, the sign of the surface potential (whether the surface is positively or negatively charged) can be deduced.[223] The off-resonance $\chi^{(3)}$ has been measured to be a negative value,[46] therefore if the phase of the signal is from 0 to π (imaginary part is positive), the surface should be negatively charged. If the phase of the signal is from 0 to $-\pi$ (imaginary part is positive), the surface should be positively charged. We will later demonstrate that such conclusions cannot be made in on-resonance experiments or with intensity-only data.

Modulating the coherence length by changing the wavelength or angle of incidence one can have a pair of or more equations. In these equations everything can be calculated except

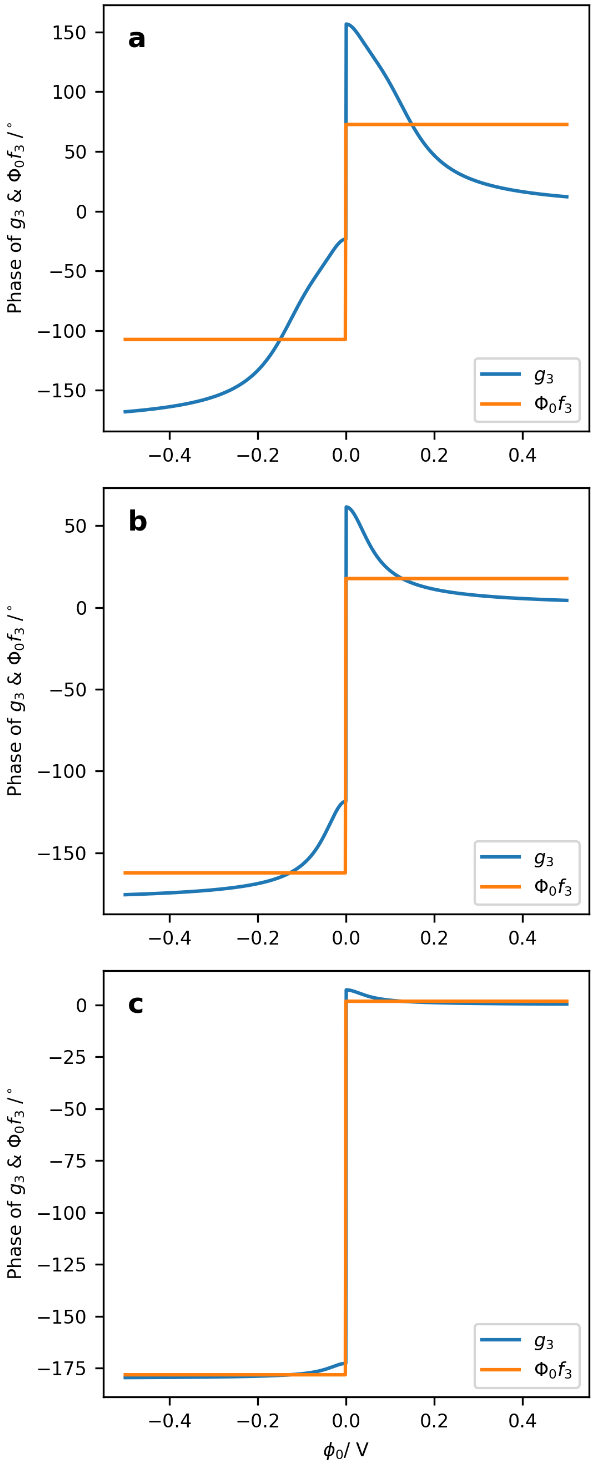

Figure 7.3: Comparison of the phase of g_3 and $\Phi_0 f_3$ in ionic strength of a) 10^{-6} M b) 10^{-4} M c) 10^{-2} M, as a function of the surface potential

R and Φ_0. They remain constant when changing the coherence length, enabling a numerical solution. After that with the magnitude of the signal it is easy to obtain the absolute value of $\chi^{(2)}_{\mathrm{BIL}}$ and $\chi^{(3)}$ if one wishes so.

This method offers several potential advantages comparing to methods using f_3. First, with just two data points it is possible to deduce the surface potential of the system. Second, it does not rely on fitting across solutions of different ionic strengths, making it possible to measure surface potential of systems with varying surface charge density depending on ionic strengths.

We now present a demonstration of the method described above. In a phase resolved SHG experiment set-up, we predict the phase of the signals measured at fundamental wavelengths of 1150 and 1500 nm. The system of study is silica-water interface and the ionic strength was set to be 10^{-6} M. We have set the surface potential to -0.2 V, and $R = -0.09$, according previous study of the silca surface in water.[47] Since only R is used here, the signal, $\chi^{(2)}$, and $\chi^{(3)}$ do not need to be in MKS units.

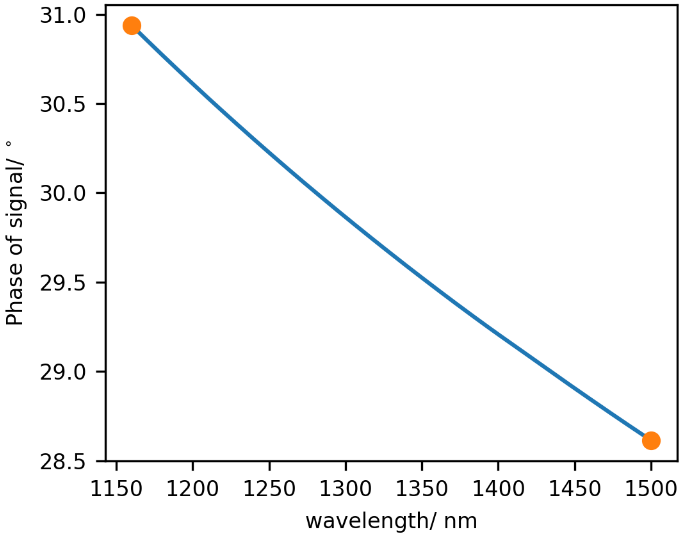

Figure 7.4: Predicted phase of the signal in a phase resolved SHG experiment and fitted date. Dots represent the prediction and solid curve represent the fitted result

As shown in Figure 7.4, the predicted phase of the signal at the fundamental wavelength of 1160 nm is about 31° and at the fundamental of 1500 nm the phase is close to 28.5°.

Since the phase of the signal is positive one can draw the conclusion that the surface is negatively charged. To solve for the surface potential from the two measurements, one simply need to use Equation 7.12 and search for the Φ_0 and R value. Here we used brute force optimizer and search for Φ_0 between -0.5 V to -10^{-4} V and R between 10^{-4} to 0.5 that matches the generated SFG intensity. The brute force result was used as an initial guess for a downhill simplex algorithm. The fitting result gave $\Phi_0 = -0.199$ V and $R = -0.0907$, which are very close to the initial parameter. In actual experiment the resolution of the phase detection might be lower. From an experimental standpoint, the ideal method of Δk_z variation depends on the laser configuration and sample stage design. When a parametric generator is available to change the wavelength over a sufficiently wide region, it is more convenient to have the beam angles remain fixed. However, for SHG experiments, fixed-frequency configurations (without an OPA) are also common, in which case angle scanning may be performed; additional caveats of this approach are discussed later.

7.3.2 Intensity-only options

Dalstein, Chiang, and Wen[222] proposed a method to measure surface potential with wavelength scanning SHG. According to Equation 7.1, 7.3, and 7.5, since $\chi^{(2)}_{\mathrm{BIL}}$ and $\chi^{(3)}$ are real and wavelength independent, when scanning the wavelength all changes in the SHG signal arises from Δk_z. With a z-cut quartz reference the authors were able to measure the SHG signal on an absolute scale. The authors studied lignoceric acid on water and by using previously obtained $\chi^{(3)}$ value of water, $\chi^{(2)}_{\mathrm{BIL}}$ of the system, and deprotonation property of lignoceric acid, they successfully predicted the wavelength scanning SHG results quantitatively. We have noticed that this method would only work when the SHG signal and $\chi^{(3)}$ value of water are in the same scale. In this case signal and $\chi^{(3)}$ value are in MKS units. However theoretically it would also work with arbitrary units as long as they are in the same scale.

Similar to the method mentioned above, one can also change the incident angle to modulate $\Delta k_z(\lambda)$ in SHG measurements. Because $\chi^{(2)}_{\mathrm{BIL}}$ and $\chi^{(3)}$ are real, the phase difference between $\chi^{(2)}_{\mathrm{BIL}}$ and $\chi^{(2)}_{\mathrm{DL}}$ is the phase of f_3 or g_3. Furthermore, with the value of off resonance $\chi^{(3)}$ it is possible to deduce the surface potential of a system without prior knowledge of the $\chi^{(2)}$ value of the BIL. Assuming an incident angle scanning SHG setup studying silica/water interface. The off resonance $\chi^{(3)}$ value is $9.56 \times 10^{-22}\mathrm{m}^2 \cdot \mathrm{V}^{-2}$,[46] and the $\chi^{(2)}$ value was assumed to be $-8 \times 10^{-23}\mathrm{m}^2 \cdot \mathrm{V}^{-1}$ and the surface potential is -0.2V.[47] The data was fitted with equation 7.1 & 7.4, searching for $\chi^{(2)}$ and Φ_0. The fitted signal was shown in Figure 7.5. The fitted result is $\chi^{(2)} = -7.99 \times 10^{-23}\mathrm{m}^2 \cdot \mathrm{V}^{-1}$ and $\Phi_0 = 0.2\mathrm{V}$.

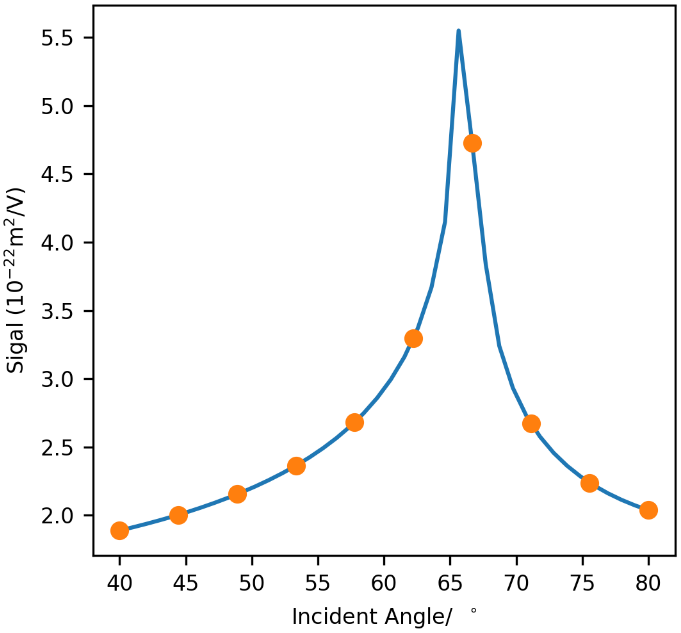

Figure 7.5: Predicted signal (dot) and fitted result (solid line) of an incident angle scanning SHG

It is worth pointing out that with traditional SHG the phase information of signal is missing, therefore the ambiguity of the sign of surface potential and $\chi^{(2)}$ exist. So the chemical nature of the charged surface (deprotonation, specific ion adsorption etc.) is required to interpret the non-linear optics result correctly.

7.4 On-resonance methods

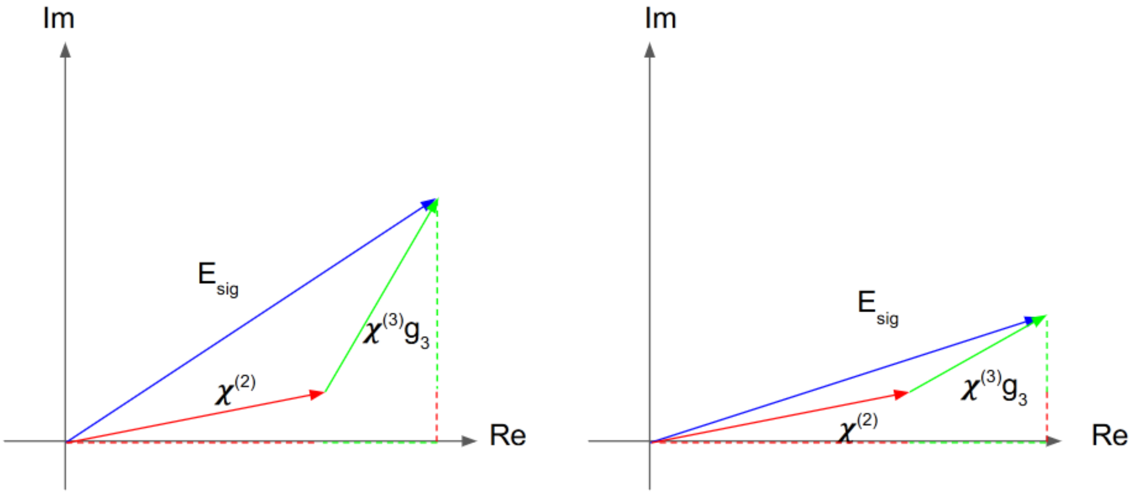

Figure 7.6: A graphical representation of the relationship of χ^2, χ^3, and signal in on resonance experiments. The two graphs represent two scenarios with different coherence length. Note that $\chi^{(2)}$ and $\chi^{(3)}$ does not change and only g_3 is changing.

7.4.1 Intensity-only options

Normal (homedyne) SFG only gives the $|E_{\text{SFG}}|^2$. And even with knowledge of $g_3\chi^{(3)}$ it is not possible to deduce the magnitude of the $\chi(2)$ term,

$$|\chi^{(2)}|^2 \neq |E_{\text{SFG}}|^2 + |g_3\chi^{(3)}|^2. \tag{7.13}$$

One piece of information is missing here, which is the phase difference between the $\chi^{(2)}$ and $g_3\chi^{(3)}$ term. To deduce the surface potential with homodyne SFG measurements by modulating the coherence length, one has to know or assume the phase difference between the two terms. Hore & Tyrode demonstrated measurement of surface potential of silica/water interface under different ionic strength using traditional SFG.[47] In the study the authors were modulating the coherence length by changing (1) the angle of incidence and (2) ionic strength (as shown in Figure 7.7). It is usually hard to determine how the surface charge behaves when changing the ionic strength, however the deprotonation of silanol groups on silica were well studied. By incorporating the deprotonation model the authors were able to correlate data with different ionic strengths. With SFG signal data on two axis it was possible to find the R value ($|\chi^{(2)}|/|\chi^{(3)}|$) and the phase difference between $\chi^{(2)}$ and $\chi^{(3)}$.

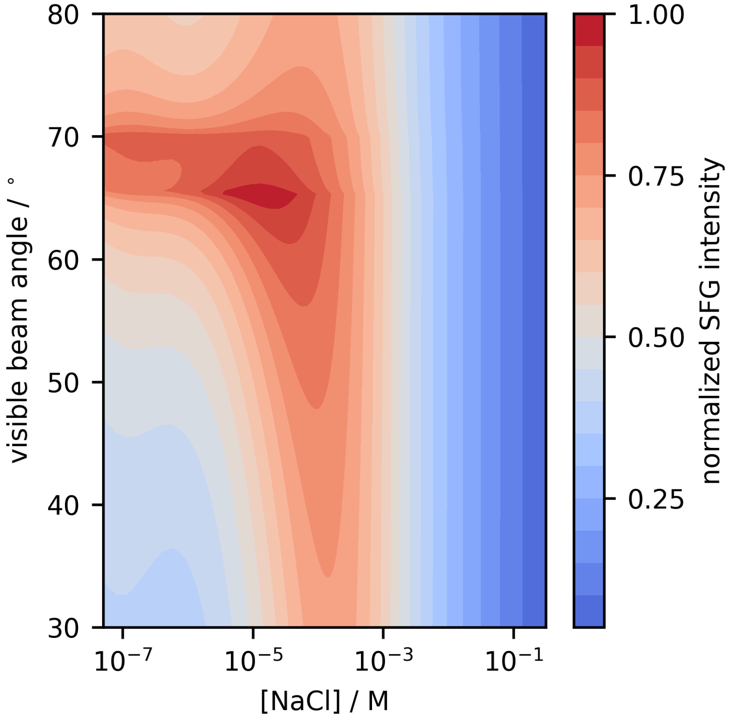

Figure 7.7: Intensity of SFG signal in the water region against ionic strength (horizontal axis) and visible beam angle (vertical axis).

With a modified deprotonation model from Hore & Tyrode, Azam *et al.* obtained the surface potential of silica/water under different temperatures.[150] The major difference between the two models was that the pK_a value for silanol deprotonation were temperature dependent following van't Hoff equation. Using the R value and phase difference from previous studies,[47,189,204] the authors were able to find the surface charge density and degree of deprotonation of the silanol groups. Elevated surface charge density and enhanced silanol deprotonation were discovered when raising the temperature.

7.4.2 Phase-resolved options

Wen *et al.* have obtained the $\chi^{(3)}$ value with phase-resolved SFG.[45] They used a monolayer of lignoceric acid on water, whose deprotonation feature has been well characterized under different pH values. By controlling the pH of the solution they were able to control the surface potential of the system. When the surface potential is low, the nonlinear susceptibility arises from BIL, E_{sig}, should remain the same as in neutral surfaces. Lignoceric acid does not deprotonate until pH ≥ 9. Therefore the E_{sig} obtained at lower pH (noted as $E_{\text{sig},0}$) could be treated as $\chi^{(2)}_{\text{BIL}}$ in low surface potential cases. Therefore $\chi^{(2)}_{\text{EDL}}$ in those cases can be obtained simply by,

$$\chi^{(2)}_{\text{EDL}} = E_{\text{sig,charged}} - E_{\text{sig},0}. \tag{7.14}$$

The surface potential can be calculated by degree of deprotonation under given pH, thus the $\chi^{(3)}$ can be extracted. The authors exhibited several $\chi^{(3)}$ spectra extracted under different environments and they remains almost identical, which demonstrated that $\chi^{(3)}$ is a bulk water feature.

Wen *et al.* have obtained the $\chi^{(3)}$ complex value in MKS units for bulk water and it has been proven to be universal in all system.[45] Such information is very useful for deducing the surface potential of a water interface with on resonance methods. For phase-resolved SFG, it is possible to deduce the surface potential directly. As shown in Figure 7.6, both $\chi^{(2)}$ and $\chi^{(3)}$ are complex when on resonance. The coherence length can be changed by varying the incident angle. Since $\chi^{(2)}$ and $\chi^{(3)}$ remain constant when changing the coherence length, the following relationship can be established,

$$\mathbb{I}\text{m}\{\chi^{(2)}\} = \mathbb{I}\text{m}\{E_{\text{SFG}}\} - \mathbb{I}\text{m}\{g_3\chi^{(3)}\} \tag{7.15a}$$

$$\mathbb{R}\text{e}\{\chi^{(2)}\} = \mathbb{R}\text{e}\{E_{\text{SFG}}\} - \mathbb{R}\text{e}\{g_3\chi^{(3)}\}. \tag{7.15b}$$

Now using the literature value of $\chi^{(3)}$ taken from Ref. 45, the only unknown remained in the equations is Φ_0 in the g_3 term and $\chi^{(2)}$. Again, it is not possible to solve for them analytically but they can be solved numerically.

A demonstration of the method is provided here. The real and imaginary part of signal are predicted in a SFG experiment. The IR wavenumber is 3200 cm^{-1}, which is in the water OH region. The visible wavelength is 532 nm and the system is silica water. The surface potential is -0.2 V and ionic strength of the solution is 10^{-6} M. The predicted signal are presented in Figure 7.8. The $\chi^{(2)}_{\text{BIL}}$ and $\chi^{(3)}$ were taken from literature.[45] The value of Φ_0 were solved using Equation 7.14 with optimization method similar to that of off resonance demonstrated before. The fitted result were presented as solid curve and the fitted value of Φ_0 was -0.02 V.

7.4.3 Limitations of the proposed methods

The basis of the methods is to change the coherence length in the g_3 term without changing other parameters. Therefore first of all the change in coherence length has to be significant. It depends on the experimental setup, the wavelength of laser used, and the refractive indices of each medium. It is highly related to two factors, which are the ionic strength of water, and the surface potential. Figures 7.9 and 7.10 are the calculated phase and magnitude of g_3 against angle of incidence in for a SFG experiment. The system of study is the silica–water interface, and the incident beams approaches the interface from the silica side. The IR wavenumber is 3200 cm^{-1}, visible wavelength is 532 nm. In (a) the ionic strength was set to be 10^{-4} M with variable surface potential, whereas in (b) the surface potential was set to be -0.02 V and changing ionic strength. As shown in the plots, with lower surface potential, the changes in magnitude are small and changes in phase are also small in higher angles. In terms of ionic strength, with high ionic strength, modulating the coherence length does not change the phase nor the magnitude of g_3 significantly. Also the phase of g_3 is close to zero, making it impossible to separate the $\chi^{(2)}_{\text{BIL}}$ and $\chi^{(3)}g_3$ terms. It will not be optimal to try to deduce the surface potential under these circumstances. In general, these method can not be applied to systems with extremely high ionic strength and extremely low surface potential, as in such environment the changes in g_3 would not be

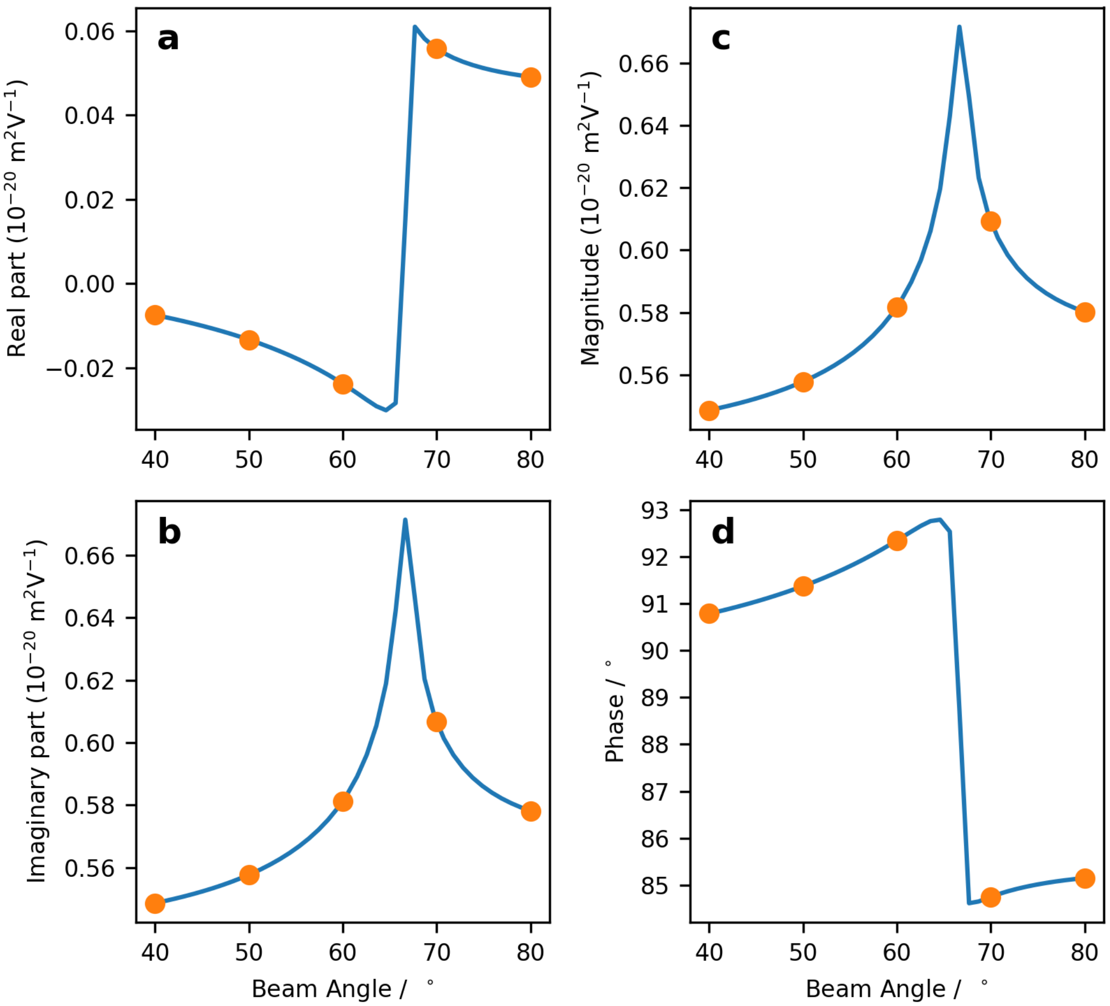

Figure 7.8: Predicted signal (dots) and fitted result (solid curve) of an angle-resolved SFG experiment on vibrational resonance at $\omega_{\mathrm{IR}} = 3200$ cm^{-1} for which the (a) real and (b) imaginary components of $\chi^{(2)}$ have been determined. Alternatively, these are displayed in terms of the (c) magnitude and (d) phase.

significant enough. And higher the ionic strength, higher surface potential is required to be detectable.

Also, as shown in equation 7.1, the contribution of the whole $\chi^{(2)}_{\mathrm{EDL}}$ term needs to be significant enough to be detectable in phase-resolved experiments. Therefore the magnitude of $\chi^{(3)}$ has to be larger than the magnitude of $\chi^{(2)}_{\mathrm{BIL}}$, otherwise the phase of the signal would be dominated by $\chi^{(2)}_{\mathrm{BIL}}$ and not much changes in the signal could be observed when modulating the coherence length. For intensity only options, the sensitivity comes

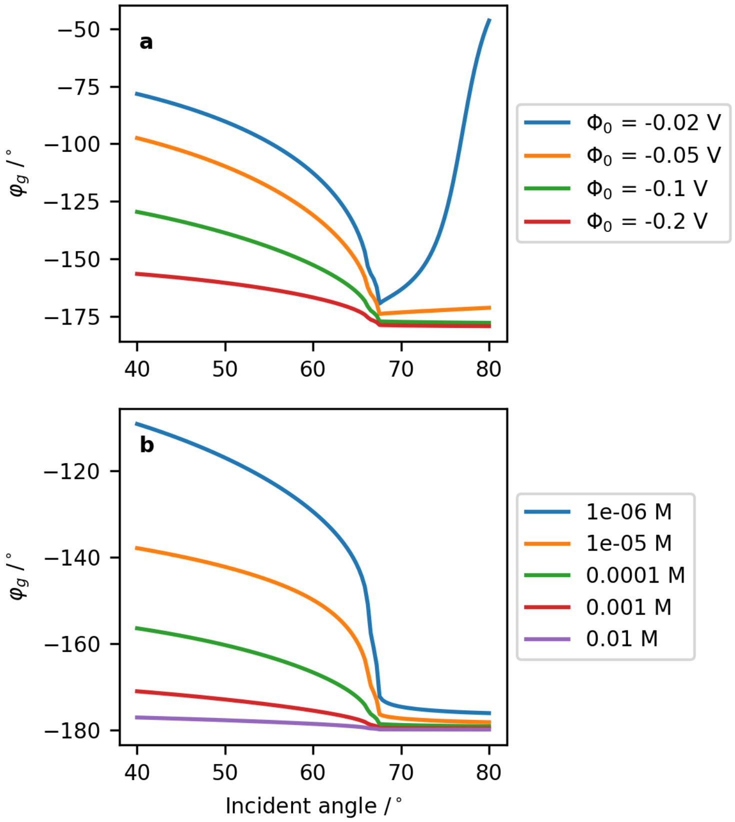

Figure 7.9: The phase of g_3 in a SFG experiment as a function of the incident angle. Plot (a) are g_3 in a constant ionic strength environment with different surface potential. Plot (b) are g_3 with given surface potential in different ionic strength environments

from the changes in signal intensity instead of the phase, therefore the value of $\chi^{(2)}_{\mathrm{BIL}}$ would not affect the sensitivity.

Finally, it is worth noting that for phase-resolved measurements, the accuracy of the method is limited by the resolution of the phase measurements of the experiment. As shown in Figure 7.9, the effect of phase measurement resolution will be more significant for less charged interfaces. Ideally the Φ_0 could be solved numerically with just two data points, however considering the experimental errors more data points might be needed in experiments.

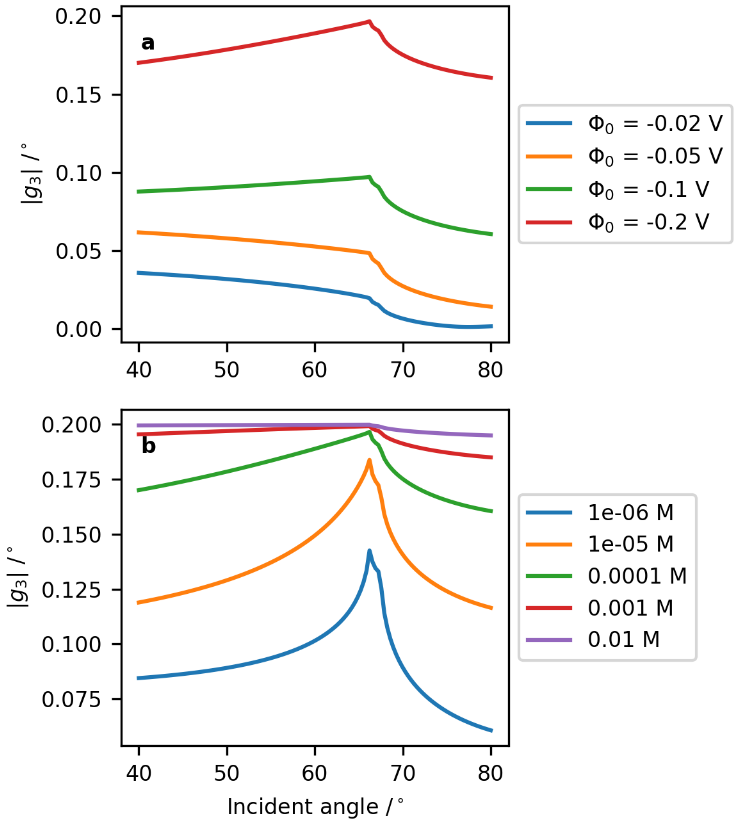

Figure 7.10: The magnitude of g_3 in a SFG experiment as a function of the incident angle. Plot (a) are g_3 in a constant ionic strength environment with different surface potential. Plot (b) are g_3 with given surface potential in different ionic strength environments

7.5 Conclusions

In this work it was shown that g_3 which was derived from the full solution of Poisson–Boltzmann equation is a more accurate depiction of the charged aqueous interface compared to $\Phi_0 \cdot f_3$, especially in cases where the surface potential is high and ionic strength is low. It was also highlighted that a major difference between the two model is that the phase of g_3 is Φ_0 dependent while f_3 is not. With this unique feature of g_3, it was proposed that by using g_3 it is possible to infer the surface potential of charged aqueous interface by changing the coherence length. Possible application of the method for phase-resolved or intensity only off-resonance experiments, and phase-resolved on-resonance experiments were demonstrated. Lastly some limitations for the method were pointed out. The changes in coherence length, in g_3, and changes in $\chi^{(3)}g_3$ also have to be significant so that the change in the intensity and/or phase of signal can be observed in experiments. All these limitations have to be satisfied in order to conduct the analysis. And the exact limits varies upon experimental set up and system of study.

Chapter 8

Conclusions

8.1 Summary

The study of interfacial properties of thin films such as polymers is an important area of surface science. However the sum-frequency generation spectroscopy result on thin-film systems need to be interpreted correctly, as the multiple beam interference effect should be taken into account, and the contribution to the total signal from both interfaces must be isolated. Straightforward and easy to use modeling and visualization tool for planning the experimental geometry when probing thin-film in liquids and air using sum frequency generation spectroscopy was presented. While there were existing model for the multiple beam interference effect, they were complicated, not readily understandable, and usually used to interpret the result after the experiment. The method was validated by examining a PDMS thin-film deposited on a fused silica substrate with a specific thickness exposed to air, water, and FC-40 environments. The method predicted no selectivity in external reflection geometry at the air–film interface, but selectively probing can be achieved in internal reflection geometry. The method was also extended to different polarization schemes, which is essential for accurate and extensive orientation analysis of interfacial functional groups. This method will be useful for all thin-film SFG experiments especially polymers, without such interfacial specificity the interpretation of the SFG result could be inaccurate or totally opposite to the actual scenario. This method was put into use in the temperature-dependent methyl orientation analysis on PDMS–liquid interface. In the study, PDMS surfaces exposed to water and FC-40 liquids were monitored using sum frequency generation spectroscopy and heated from 20 °C to 70 °C. A new framework for molecular orientation was proposed. It enables detailed orientation analysis when an external perturbation is applied. It was found that methyl groups on the PDMS surface behave similarly when exposed to hydrophobic and hydrophilic environments. The methyl groups started in a upright orientation at lower temperatures, and with rising temperature, the methyl groups became more parallel to the surface normal. The behaviour was explained by the changes in conformation of the siloxane backbone: with increasing temperature the siloxane backbone becomes more corrugated due to heterogeneous density change in the surface plane and surface normal directions.

Water is a good reporter of the surface charge on solid–aqueous interfaces. Second-order nonlinear optical techniques have been established as sensitive probes of charged interfaces, and can even provide quantitative information on the surface potential. When probing the water molecules at the silica surface under increasing temperature, the –OH stretching signal at 3180 cm^{-1} increased first, and started to drop after reached about 60 °C. A deprotonation model of silanol groups was applied to interpret the data. It was found that with elevated temperature the silanol groups on the silica surface have an enhanced deprotonation, leading to increasing surface charge density and surface potential. The surface charge at PDMS–water interface were also deduced. Spectra were taken from the PDMS–water interface with visible incident angle from 64° to 70°, and the ionic strength of water varied from 10^{-6} M to 10^{-2} M. It was determined that ion adsorption was charging PDMS surfaces in water, and the ion adsorption process can be described with a Freundlich isotherm. The surface charge of untreated PDMS surface in aqueous solutions of different ionic strengths was measured for the first time. Finally, methods that have been proposed to assess the surface potential at charged aqueous interfaces using second-order nonlinear optical methods were compared, and a unified method for measuring the surface potential using nonlinear optics were proposed. The method is free of any deprotonation or ion adsorption model. This method opens up the possibility of accurate and non-intrusive measurement of surface charge of solid–water interfaces that was hard to quantify using traditional measuring methods.

8.2 Recommendations for future work

While the method development for probing the solid–aqueous interfaces, especially for thin-films have been mostly completed, there are still aspects left to be explored. As demonstrated in Chapter 3, even though the general trend agrees with prediction, the selectivity is not always fully achieved. This is because in reality the relative contribution from each sides of the film does not only related to the local field factors, but also the magnitude and phase of the nonlinear susceptibility. Further development of the experimental setup can be focused on further enhancement of local field factors on the desired side and suppression on the other one. For example, other substrates like metals could be explored as preliminary results show that metal substrates like aluminum could greatly enhance the local field factors and possibly enable selective probing in external reflection geometries. The structural change on the PDMS–liquid interface on a molecular level was revealed. However the longevity of silicone materials are susceptible to not only high temperature, but also other external factors like high concentration salt solution treatment, UV irradiation, and electrical discharge etc. By comparing the orientation analysis results to the surface performance like hydrophobicity of silicone materials went through the same environments will give a microscopic picture of the silicone surfaces under environmental stress, and help in developing and manufacturing the next generation of silicone materials.

A detailed discussion about the relative nonlinear contribution from the water molecules on the surface and in the bulk was provided in the thesis. Recently a new imaginary term in the second-order susceptibility was reported and requires further investigations.[234] Phase-resolved sum frequency generation spectroscopy could be the tool for the investigation, as it provides on-resonance result and based on the vibrational mode the origin of the new term could be determined. Phase-resolved experiments should also be done on silica– and silicone–water interfaces and using the method proposed in Chapter 7 the surface charge derived from deprotonation or ion adsorption models could be confirmed. Surface charge measurement could also be done on PDMS surfaces after treatments like UV irradiation, plasma treatment, and electrical discharge. Combined with orientation analysis on PDMS surface groups it will lend insight into the mechanism of charging PDMS surfaces.

References

[1] Abbasi, F.; Mirzadeh, H.; Katbab, A.-A. *Polym. Int.* **2001,** *50,* 1279–1287.

[2] HILL, R. G. Biomedical Polymers. In *Biomaterials, Artificial Organs and Tissue Engineering*; Elsevier: Amsterdam, NL, 2005.

[3] Wong, I.; Ho, C.-M. *Microfluid and Nanofluidics* **2009,** *7,* 291.

[4] Amin, M.; Akbar, M.; Amin, S. *Rev. Adv. Mater. Sci.* **2007,** *16,* 10–26.

[5] Kim, S.-H.; Cherney, E. A.; Hackam, R. *IEEE Trans. Electr. Insul.* **1992,** *27,* 610–622.

[6] Kim, J.; Chaudhury, M.; Owen, M. *IEEE Trans. Dielectr. Electr. Insul.* **1999,** *6,* 695–702.

[7] Karady, G. G.; Shah, M.; Brown, R. *IEEE Trans. Power. Del.* **1995,** *10,* 1965–1971.

[8] Gorur, R.; Orbeck, T. *IEEE Trans. Electr. Insul.* **1991,** *26,* 1064–1072.

[9] Vlastos, A. E.; Orbeck, T. *IEEE Trans. Power Del.* **1996,** *11,* 1066–1070.

[10] Hillborg, H.; Tomczak, N.; Olàh, A.; Schönherr, H.; Vancso, G. J. *Langmuir* **2004,** *20,* 785–794.

[11] Vlachopoulou, M.-E.; Petrou, P.; Kakabakos, S.; Tserepi, A.; Beltsios, K.; Gogolides, E. *Microelectron. Eng.* **2009,** *86,* 1321–1324.

[12] Kirby, B. J.; Hasselbrink, E. F. *Electrophoresis* **2004,** *25,* 187–202.

[13] Zhou, J.; Ellis, A. V.; Voelcker, N. H. *Electrophoresis* **2010,** *31,* 2–16.

[14] Shirai, T.; Takai, M.; Ishihara, K. Simple and functional modification of PDMS surface for microchannel electropheresis. In *14th International Conference on Miniaturized Systems for Chemistry and Life Sciences 2010, MicroTAS 2010*, Vol. 3; MicroTAS 2010: Groningen, Netherlands, 2010.

[15] Schrott, W.; Slouka, Z.; Červenka, P.; Ston, J.; Nebyla, M.; Přibyl, M.; Šnita, D. *Biomicrofluidics* **2009,** *3,* 044101.

[16] Mampallil, D.; van den Ende, D.; Mugele, F. *Electrophoresis* **2010,** *31,* 563–569.

[17] Kump, L. R.; Brantley, S. L.; Arthur, M. A. *Annu. Rev. Earth Planet. Sci.* **2000,** *28,* 611–667.

[18] Dove, P. M.; Han, N.; Wallace, A. F.; De Yoreo, J. J. *Proc. Natl. Acad. Sci. U.S.A.* **2008,** *105,* 9903–9908.

[19] Dove, P. M.; Han, N.; Yoreo, J. J. D. *Proc. Natl. Acad. Sci. USA* **2005,** *102,* 15357–15362.

[20] Sun, L.-B.; Liua, X.-Q.; Zhou, H.-C. *Chem. Soc. Rev.* **2015,** *44,* 5092–5147.

[21] Munnik, P.; de Jongh, P. E.; de Jong, K. P. *Chem. Rev.* **2015,** *115,* 6687–6718.

[22] Luchansky, M. S.; Bailey, R. C. *Anal. Chem.* **2012,** *84,* 793–821.

[23] Walcarius, A. *Chem. Mater.* **2001,** *13,* 3351–3372.

[24] Conzone, S. D.; Pantano, C. G. *Mater. Today* **2004,** *7,* 20–26.

[25] Mills, J. C.; Roth, K. A.; Cagan, R. L.; Gordon, J. I. *Nat. Cell Biol.* **2001,** *3,* E175–E178.

[26] Yang, P.; Gaib, S.; Lin, J. *Chem. Soc. Rev.* **2012,** *41,* 3679–3698.

[27] Venitti, R. Encyclopedia of Microfluidics and Nanofluidics. In ; Li, D., Ed.; Springer: New York City, NY, 2008; Chapter Temperature Effects on the Zeta Potential, pages 1980–1987.

[28] Bracco, G.; Holst, B. *Surface science techniques;* Springer Science & Business Media: New York City, NY, 2013.

[29] Boyd, R. W. *Nonlinear Optics;* Academic Press: San Diego, 2nd ed.; 2003.

[30] Morita, A. *Theory of Sum Frequency Generation Spectroscopy;* Springer: Singapore, 2018.

[31] Chen, Z.; Shen, Y. R.; Somorjai, G. A. *Annu. Rev. Phys. Chem.* **2002,** *53,* 437–465.

[32] FitzGerald, W. R.; Jena, K. C.; Hore, D. K. *J. Mol. Struct.* **2014,** *1084,* 368-373.

[33] Azam, M. S.; Cai, C.; Hore, D. K. *J. Phys. Chem. C* **2019,** *123,* 23535–23544.

[34] Koschwanez, J. H.; Carlson, R. H.; Meldrum, D. R. *PLoS ONE* **2009,** *4(2),* e4572.

[35] Braci, M.; Mohan, T.; Kargl, R.; Hribernik, T. G. S.; Kostler, S.; Stana-Kleinscheka, K.; Fras-Zemljic, L. *RSC Adv.* **2014,** *4,* 11955–11961.

[36] Shen, Y. R. Surface Spectroscopy by Nonlinear Optics. In *Proc. Int. School of Physics, Ernico Fermi*; Hansch, T. W.; Inguscio, M., Eds.; North Holland: Amsterdam, 1994.

[37] Born, M.; Wolf, E. *Principles of Optics;* Pergamon Press Ltd.: Oxford, 4th ed.; 1970.

[38] Hansen, W. N. *J. Opt. Soc. Am.* **1968,** *58,* 380–390.

[39] Axelsen, P. H.; Citra, M. J. *Prog. Biophys. Molec. Biol.* **1996,** *66,* 227–253.

[40] Tadros, T. *Encyclopedia of Colloid and Interface Science.;* Springer: New York City, NY, 2013.

[41] Butt, H.-J.; Graf, K.; Kappl, M. *Physics and chemistry of interfaces;* John Wiley & Sons: Hoboken, NJ, 2013.

[42] Bard, A.; Faulkner, L. *Electrochemical Methods: Fundamentals and Applications, 2nd Edition;* John Wiley & Sons, Incorporated: Hoboken, NJ, 2000.

[43] Ong, S.; Zhao, X.; Eisenthal, K. B. *Chem. Phys. Lett.* **1992,** *191,* 327–335.

[44] Gonella, G.; Lütgebaucks, C.; de Beer, A. G. F.; Roke, S. *J. Phys. Chem. C* **2016,** *120,* 9165–9173.

[45] Wen, Y.-C.; Zha, S.; Liu, X.; Yang, S.; Guo, P.; Shi, G.; Fang, H.; Shen, Y. R.; Tian, C. *Phys. Rev. Lett.* **2016,** *116,* 016101.

[46] Dalstein, L.; Chiang, K. Y.; Wen, Y. C. *J. Phys. Chem. Lett.* **2019,** *10,* 5200–5205.

[47] Hore, D. K.; Tyrode, E. *J. Phys. Chem. C* **2019,** *123,* 16911–16920.

[48] Shen, Y. R. *The Principles of Nonlinear Optics;* John Wiley & Sons: New York, 1984.

[49] Shen, Y. R. *J. Phys. Chem. C* **2012,** *116,* 15505–15509.

[50] Chen, Z. *Prog. Polym. Sci.* **2010,** *35,* 1376–1402.

[51] O'Brien, D.; Massari, A. *J. Chem. Phys* **2013,** *138,* 154708.

[52] O'Brien, D. B.; Massari, A. M. *J. Opt. Soc. Am. B: Opt. Phys.* **2013,** *30,* 1503–1512.

[53] O'Brien, D. B.; Massari, A. M. *J. Chem. Phys.* **2015,** *142,* 024703.

[54] Lambert, A. G.; Neivandt, D. J.; Briggs, A. M.; Usadi, E. W.; Davies, P. B. *J. Phys. Chem. B* **2002,** *106,* 5461–5469.

[55] McGall, S. J.; Davies, P. B.; Neivandt, D. J. *J. Phys. Chem. B* **2004,** *108,* 16030–16039.

[56] Tong, Y.; Zhao, Y.; Li, N.; Osawa, M.; Davies, P. B.; Ye, S. *J. Chem. Phys* **2010,** *133,* 034704.

[57] Tong, Y.; Zhao, Y.; Li, N.; Ma, Y.; Osawa, M.; Davies, P. B.; Ye, S. *J. Chem. Phys* **2010,** *133,* 034705.

[58] Li, G.; Dhinojwala, A.; Yeganeh, M. S. *J. Phys. Chem. C* **2011,** *115,* 7554–7561.

[59] Moon, A. P.; Pandey, R.; Bender, J. A.; Cotton, D. E.; Renard, B. A.; Roberts, S. T. *J. Phys. Chem. C* **2017,** *121,* 18653–18664.

[60] Hirose, C.; Ishida, H.; Iwatsu, K.; Watanabe, N.; Kubota, J.; Wada, A.; Domen, K. *J. Chem. Phys.* **1998,** *108,* 5948–5956.

[61] Yeh, P. *et al. Optical waves in layered media;* volume 95 Wiley New York: New York City, NY, 1988.

[62] Sipe, J. *J. Opt. Soc. Am. B: Opt. Phys.* **1987,** *4,* 481–489.

[63] Hankett, J. M.; Lu, X.; Liu, Y.; Seeley, E.; Chen, Z. *Phys. Chem. Chem. Phys.* **2014,** *16,* 20097–20106.

[64] Otsuki, Y.; Ishiyama, T. S. T.; Morita, A.; Watanabe, K.; Matsumoto, Y. *Phys. Rev. B* **2017,** *96,* 115405.

[65] Lu, X.; Clarke, M. L.; Li, D.; Wang, X.; Xue, G.; Chen, Z. *J. Phys. Chem. C* **2011,** *115,* 13759–13767.

[66] Backus, E. H. G.; Garcia-Araez, N.; Bonn, M.; Bakker, H. J. *J. Chem. Phys. C* **2012,** *116,* 23351–23361.

[67] Wilk, D.; Johannsmann, D.; Stanners, C.; Shen, Y. *Phy. Rev. B* **1995,** *51,* 10057.

[68] Wang, J.; Paszti, Z.; Even, M. A.; Chen, Z. *J. Phys. Chem. B* **2004,** *108,* 3625–3632.

[69] Ramsay, M.; Beutier, C.; McGarvey, G. B.; Hore, D. K. *J. Chem. Phys.* **2019,** *150,* 014702.

[70] Jena, K. C.; Hore, D. K. *J. Phys. Chem. C* **2009,** *113,* 15364–15372.

[71] Zhuang, X.; Miranda, P. B.; Kim, D.; Shen, Y. R. *Phys. Rev. B* **1999,** *59,* 12632-12640.

[72] Okuno, M.; Ishibashi, T.-a. *J. Chem. Phys.* **2018,** *149,* 244703.

[73] Wang, L.; Nihonyanagi, S.; Inoue, K.-i.; Nishikawa, K.; Morita, A.; Ye, S.; Tahara, T. *J. Phys. Chem. C* **2019,** *123,* 15665–15673.

[74] Malitson, I. H. *J. Opt. Soc. Am.* **1965,** *55,* 1205–1209.

[75] Schneider, F.; Draheim, J.; Kamberger, R.; Wallrabe, U. *Sens. Actuators, A* **2009,** *151,* 95–99.

[76] Querry, M. “Optical Constants of Minerals and Other Materials from the Millimeter to the Ultraviolet”, Technical Report, Chemical Research Development And Engineering Center Aberdeen Proving Groundmd, 1987.

[77] Segelstein, D. J. “The Complex Refractive Index of Water”, Master’s thesis, University of Missouri, 1981.

[78] Electronics Materials Solutions Division, “3M Fluorinert Electronic Liquid FC-40”, Technical Report, 3M, 2019.

[79] Gragson, D. E.; McCarty, B. M.; Richmond, G. L. *J. Am. Chem. Soc.* **1997,** *119,* 6144–6152.

[80] Zhang, D.; Ward, R.; Shen, Y.; Somorjai, G. *J. Phys. Chem. B* **1997,** *101,* 9060–9064.

[81] Chen, Z.; Ward, R.; Tian, Y.; Baldelli, S.; Opdahl, A.; Shen, Y.-R.; Somorjai, G. A. *J. Am. Chem. Soc.* **2000,** *122,* 10615–10620.

[82] Chen, C.; Wang, J.; Chen, Z. *Langmuir* **2004,** *20,* 10186–10193.

[83] Ye, H.; Gu, Z.; Gracias, D. *Langmuir* **2006,** *22,* 1863–1868.

[84] Ye, S.; McClelland, A.; Majumdar, P.; Stafslien, S. J.; Daniels, J.; Chisholm, B.; Chen, Z. *Langmuir* **2008,** *24,* 9686–9694.

[85] Shi, Q.; Ye, S.; Spanninga, S. A.; Su, Y.; Jiang, Z.; Chen, Z. *Soft Matter* **2009,** *18,* 3487–3494.

[86] Kim, C.; Gurau, M. C.; Cremer, P. S.; Yu, H. *Langmuir* **2008,** *24,* 10155–10160.

[87] Hsiao, E.; Barnette, A. L.; Bradley, L. C.; Kim, S. H. *ACS Appl. Mater. Interfaces* **2011,** *3,* 4236–4241.

[88] Hankett, J. M.; Liu, Y.; Zhang, X.; Zhang, C.; Chen, Z. *J. Poly. Sci.* **2013,** *51,* 311–328.

[89] Yamaguchi, S.; Shiratori, K.; Morita, A.; Tahara, T. *J. Chem. Phys.* **2011,** *134,* 184705.

[90] Sun, S.; Tian, C.; Shen, Y. R. *Proc. Nat. Acad. Sci. USA* **2015,** *112,* 5883–5887.

[91] Held, H.; Lvovsky, A. I.; Wei, X.; Shen, Y. R. *Phys. Rev. B* **2002,** *66,* 205110.

[92] Maikhuri, D.; Rurohit, S. P.; Mathur, K. C. *AIP Adv.* **2015,** *5,* 047115.

[93] Wei, X.; Hong, S.-C.; Lvovsky, A. I.; Held, H.; Shen, Y. R. *J. Phys. Chem. B* **2000,** *104,* 3349–3354.

[94] Matsuzaki, K.; Nihonyanagi, S.; Yamaguchi, S.; Nagata, T.; Tahara, T. *J. Phys. Chem. Lett.* **2013,** *4,* 1654–1658.

[95] Zheng, R.; Weo, W. M.; Shi, Q. *Phys. Chem. Chem. Phys.* **2015,** *17,* 9068–9073.

[96] Li, X.; Yu, X.; Han, Y. *J. Mater. Chem. C* **2013,** *1,* 2266–2285.

[97] Zelikin, A. N. *ACS Nano* **2010,** *4,* 2494–2509.

[98] Shi, Y.; Liu, J.; Yang, Y. *J. Appl. Phys.* **2000,** *87,* 4254–4263.

[99] Prakash, S.; Chakrabarty, T.; Singh, A. K.; Shahi, V. K. *Biosens. Bioelectron.* **2013,** *41,* 43–53.

[100] Harsányi, G. *Sensor Rev.* **2000,** *20,* 98–105.

[101] Amjadi, M.; Kyung, K.-U.; Park, I.; Sitti, M. *Adv. Funct. Mater.* **2016,** *26,* 1678–1698.

[102] Vendra, V. K.; Wu, L.; Krishnan, S. Polymer Thin Films For Biomedical Applications. In *Nanotechnologies for the Life Sciences*; Kumar, C. S. S. R., Ed.; American Cancer Society: St. Louis, MO, 2011.

[103] Charney, E. *J. Opt. Soc. Am.* **1955,** *45,* 980–983.

[104] Chollet, P.-A.; Messier, J.; Rosilio, C. *J. Chem. Phys.* **1976,** *64,* 1042–1050.

[105] Dluhy, R. A. *J. Phys. Chem.* **1986,** *90,* 1373–1379.

[106] Li, X.; Li, B.; Zhang, X.; Li, C.; Guo, Z.; Zhou, D.; Lu, X. *Macromolecules* **2016,** *49,* 3116–3125.

[107] Wilson, P. T.; Briggman, K. A.; Wallace, W. E.; Stephenson, J. C.; Richter, L. J. *Appl. Phys. Lett.* **2002,** *80,* 3084–3086.

[108] Yeh, P. *Optical Waves in Layered Media;* volume 95 John Wiley & Sons, Inc.: Hoboken, New Jersey, 1988.

[109] Wang, J.; Chen, C.; Buck, S. M.; Chen, Z. *J. Phys. Chem. B* **2001,** *105,* 12118–12125.

[110] Wang, H.-F.; Gan, W.; Lu, R.; Rao, Y.; Wu, B. H. *Int. Rev. Phys. Chem.* **2005,** *24,* 191–256.

[111] Kataoka, S.; Cremer, P. S. *J. Am. Chem. Soc.* **2006,** *128,* 5516–5522.

[112] Wang, J.; Paszti, Z.; Even, M. A.; Chen, Z. *J. Am. Chem. Soc.* **2002,** *124,* 7016–7023.

[113] Chen, C.; Wang, J.; Even, M. A.; Chen, Z. *Macromolecules* **2002,** *35,* 8093–8097.

[114] Zhang, C.; Chen, Z. *J. Phys. Chem. C* **2013,** *117,* 3903–3914.

[115] Moskovits, M. *J. Chem. Phys.* **1982,** *77,* 4408–4416.

[116] Lu, X.; Li, D.; Kristalyn, C. B.; Han, J.; Shephard, N.; Rhodes, S.; Xue, G.; Chen, Z. *Macromolecules* **2009,** *42,* 9052–9057.

[117] Lu, X.; Xue, G.; Wang, X.; Han, J.; Han, X.; Hankett, J.; Li, D.; Chen, Z. *Macromolecules* **2012,** *45,* 6087–6094.

[118] McGovern, M. E.; Kallury, K. M. R.; Thompson, M. *Langmuir* **1994,** *10,* 3607–3614.

[119] Yang, W.-C.; Busson, B.; Hore, D. K. *J. Chem. Phys.* **2019,** *152,* 084708.

[120] Cai, C.; Azam, M. S.; Hore, D. K. *J. Phys. Chem. C* **2021,** *125,* 12382–12389.

[121] Gan, W.; Wu, D.; Zhang, Z.; Feng, R.-R.; Wang, H.-F. *J. Chem. Phys.* **2006,** *124,* 114705.

[122] Holman, J.; Davies, P. B.; Nishida, T.; Ye, S.; Neivandt, D. J. *J. Phys. Chem. B* **2005,** *109,* 18723–18732.

[123] Shit, S. C.; Shah, P. *Natl. Acad. Sci. Lett.* **2013,** *36,* 355–365.

[124] Perry, R.; Quinn, C.; Traver, F.; Murthy, K. Synthetics, Mineral Oils, and Bio-Based Lubricants. In ; CRC Press: Boca Raton, 2020; Chapter Silicones, pages 235–247.

[125] Ghosh, D.; Khastgir, D. *ACS Omega* **2018,** *3,* 11317–11330.

[126] Ghosh, D.; Bhandari, S.; Chaki, T. K.; Khastgir, D. *RSC Adv.* **2015,** *5,* 57608–57618.

[127] Hillborg, H.; Gedde, U. W. *IEEE Trans. Dieletr. Electr. Insul.* **1999,** *6,* 703–717.

[128] Venkatesulu, B.; Thomas, M. J. *IEEE Trans. Dielectr. Electr. Insul.* **2010,** *18,* 418–424.

[129] Khan, Y. *Am. J. Eng. Appl. Sci.* **2009,** *2,* 438–445.

[130] Glüge, J.; Scheringer, M.; Cousins, I. T.; DeWitt, J. C.; Goldenman, G.; Herzke, D.; Lohmann, R.; Ng, C. A.; Trier, X.; Wang, Z. *Environ. Sci. Process Impacts* **2020,** *22,* 2345–2373.

[131] Budziak, C. J.; Vargha-Butler, E. I.; Neumann, A. W. *J. Appl. Poly. Sci.* **1991,** *42,* 1959–1964.

[132] Yap, Y.-F.; Tan, S.-H.; Nguyen, N.-T.; Sohel Murshed, S. M.; Wong, T.-N.; Yobas, L. *J. Appl. Phys. D* **2009,** *42,* 065503.

[133] Ting, T.-H.; Yap, Y.-F.; Nguyen, N.-T.; Wong, T.-N.; Chai, J. C. K. *Appl. Phys. Lett.* **2006,** *89,* 234101.

[134] Brochard, F. *Langmuir* **1989,** *5,* 432–438.

[135] Selva, B.; Cantata, I.; Jullien, M.-C. *Phys. Fluids* **2011,** *23,* 052002.

[136] Selva, B.; Miralles, V.; Cantat, I.; Jullien, M.-C. *Lab Chip* **2010,** *10,* 1835–1840.

[137] Wang, J.; Woodcock, S. E.; Buck, S. M.; Chen, C.; Chen, Z. *J. Am. Chem. Soc.* **2001,** *123,* 9470–9471.

[138] Tateishi, Y.; Kai, N.; Noguchi, H.; Uosaki, K.; Nagamura, T.; Tanaka, K. *Polym. Chem.* **2010,** *1,* 303–311.

[139] Rao, A.; Rangwalla, H.; Varshney, V.; Dhinojwala, A. *Langmuir* **2004,** *20,* 7183–7188.

[140] Li, Q.; Hua, R.; Cheah, I. J.; Chou, K. C. *J. Phys. Chem. B* **2008,** *112,* 694–697.

[141] Clarke, M. L.; Chen, C.; Wang, J.; Chen, Z. *Langmuir* **2006,** *22,* 8800–8806.

[142] Lu, X.; Shepard, N.; Han, J.; Xue, G.; Chen, Z. *Macromolecules* **2008,** *41,* 8770–8777.

[143] Kweskin, S. J.; Komvopoulos, K.; Somorjai, G. A. *Langmuir* **2005,** *21,* 3647–3652.

[144] Liu, Y.; Messmer, M. *J. Am. Chem. Soc.* **2002,** *124,* 9714–9715.

[145] Miyamae, T.; Nozoye, H. *Surf. Sci.* **2003,** *532–535,* 1045–1050.

[146] Ahn, D.; Dhinojwala, A. Sum Frequency Generation Vibrational Spectroscopy of Silicone Surfaces and Interfaces. In *Silicone Surface Science*; Owen, M. J.; Dvornic, P. R., Eds.; Springer: New York, 2012.

[147] Voges, A. B.; Al-Abadleh, H. A.; Musorrafiti, M. J.; Bertin, P. A.; Nguyen, S. T.; Geiger, F. M. *J. Phys. Chem. B* **2004,** *108,* 18675–18682.

[148] Kurian, A.; Prasad, S.; Dhinojwala, A. *Macromolecules* **2010,** *43,* 2438–2443.

[149] Nanjundiah, K.; Hsu, P. Y.; Dhinojwala, A. *J. Chem. Phys.* **2009,** *130,* 024702.

[150] Azam, M. S.; Cai, C.; Gibbs, J. M.; Tyrode, E.; Hore, D. K. *J. Am. Chem. Soc* **2020,** *142,* 669–673.

[151] Hall, S. A.; Jena, K. C.; Covert, P. A.; Roy, S.; Trudeau, T. G.; Hore, D. K. *J. Phys. Chem. B* **2014,** *118,* 5617–5636.

[152] Hall, S. A.; Hickey, A. D.; Hore, D. K. *J. Phys. Chem. C* **2010,** *114,* 9748–9757.

[153] Odhner, H.; Jacobs, D. *J. Chem. Eng. Data* **2012,** *57,* 166–168.

[154] Frontas' Ev, V.; Shraiber, L. *J. Struct. Chem.* **1965,** *6,* 493–500.

[155] Kedenburg, S.; Vieweg, M.; Gissibl, T.; Giessen, H. *Opt. Mater. Express* **2012,** *2,* 1588–1611.

[156] Max, J.-J.; Chapados, C. *J. Chem. Phys.* **2009,** *131,* 184505.

[157] Matsuoka, J.; Kitamura, N.; Fujinaga, S.; Kitaoka, T.; Yamashita, H. *J. Non-Cryst. Solids* **1991,** *135,* 86–89.

[158] Looyenga, H. *J. Polym Sci.* **1973,** *11,* 1331–1336.

[159] Roberts, C. C.; Graham, A.; Nemer, M.; Phinney, L. M.; Garcia, R. M.; Soehnel, M. M.; Stirrup, E. K. **2017,** .

[160] Zhang, X.; Qiu, J.; Li, X.; Zhao, J.; Liu, L. *Appl. Opt.* **2020,** *59,* 2337–2344.

[161] Zhang, X.; Qiu, J.; Zhao, J.; Li, X.; Liu, L. *J. Quant. Spectrosc. Radiat. Transfer* **2020,** *252,* 107063.

[162] Liu, Y.; Leng, C.; Chisholm, B.; Stafslien, S.; Majumdar, P.; Chen, Z. *Langmuir* **2013,** *29,* 2897–2905.

[163] Ismail, A. E.; Grest, G. S.; Heine, D. R.; Steves, M. J.; Tsige, M. *Macromolecules* **2009,** *42,* 3186–3194.

[164] Tsige, M.; Soddemann, T.; Rempe, S. B.; Grest, G. S.; Kress, J. D.; Robbins, M. O.; Sides, S. W.; Stevens, M. J.; Webb, E. *J. Chem. Phys.* **2003,** *118,* 5132–5142.

[165] Cabrera, J. N.; Ruiz, M. M.; Fascio, M.; D'Accorso, N.; Mincheva, R.; Dubois, P.; Lizarraga, L.; Negri, R. M. *Polymers* **2017,** *9,* 331.

[166] Azam, M. S.; Weeraman, C. N.; Gibbs-Davis, J. M. *J. Phys. Chem. Lett.* **2012,** *3,* 1269–1274.

[167] Azam, M. S.; Weeraman, C. N.; Gibbs-Davis, J. M. *J. Phys. Chem. C* **2013,** *117,* 8840–8850.

[168] Azam, M. S.; Darlington, A.; Gibbs-Davis, J. M. *J. Phys.: Condens. Matter* **2014,** *26,* 244107.

[169] DeWalt-Kerian, E. L.; Kim, S.; Azam, M. S.; Zeng, H.; Liu, Q.; Gibbs, J. M. *J. Phys. Chem. Lett.* **2017,** *8,* 2855–2861.

[170] Jena, K. C.; Covert, P. A.; Hore, D. K. *J. Phys. Chem. Lett.* **2011,** *2,* 1056–1061.

[171] Covert, P. A.; Jena, K. C.; Hore, D. K. *J. Phys. Chem. Lett.* **2014,** *5,* 143–148.

[172] Yang, Z.; Li, Q.; Chou, K. C. *J. Phys. Chem. C* **2009,** *113,* 8201–8205.

[173] Lovering, K. A.; Bertram, A. K.; Chou, K. C. *J. Phys. Chem. C* **2016,** *120,* 18099–18104.

[174] Flores, S. C.; Kherb, J.; Cremer, P. S. *J. Phys. Chem. C* **2012,** *116,* 14408–14413.

[175] Flores, S. C.; Kherb, J.; Nonelick, N.; Chen, X.; Cremer, P. S. *J. Phys. Chem. C* **2012,** *116,* 5730–5734.

[176] Du, Q.; Freysz, E.; Shen, Y. R. *Phys. Rev. Lett.* **1994,** *72,* 238–241.

[177] Campen, R. K.; Pymer, A. K.; Nihonyanagi, S.; Borguet, E. *J. Phys. Chem. C* **2010,** *114,* 18465–18473.

[178] Ostroverkhov, V.; Waychunas, G. A.; Shen, Y. R. *Chem. Phys. Lett.* **2004,** *386,* 144–148.

[179] Ostroverkhov, V.; Waychunas, G. A.; Shen, Y. R. *Phys. Rev. Lett.* **2005,** *94,* 046102.

[180] Dewan, S.; Yeganeh, M. S.; Borguet, E. *J. Phys. Chem. Lett.* **2013,** *4,* 1977–1982.

[181] Dalstein, L.; Potapova, E.; Tyrode, E. *Phys. Chem. Chem. Phys.* **2017,** *19,* 10343–10349.

[182] Fournier, R. O.; Rowe, J. J. *Am. Mineral.* **1977,** *62,* 1052–1056.

[183] Siever, R. *J. Geol.* **1962,** *70,* 127–150.

[184] Alexander, G. B.; Heston, W. M.; Iler, R. K. *J. Phys. Chem.* **1954,** *58,* 453–455.

[185] Crundwell, F. K. *ACS Omega* **2017,** *2,* 1116–1127.

[186] Azam, S.; Gibbs-Davis, J. M. *Anal. Chem.* **2013,** *85,* 8031–8038.

[187] Schaefer, J.; Gonella, G.; Bonn, M.; Backus, E. H. G. *Phys. Chem. Chem. Phys.* **2017,** *19,* 16875–16880.

[188] Zhang, C.; Sprik, M. *Phy. Rev. B* **2016,** *93,* 144201.

[189] Joutsuka, T.; Morita, A. *J. Phys. Chem. C* **2018,** *122,* 11407–11413.

[190] Bashkatov, A. N.; Genina, E. A. *Proc. SPIE* **2003,** *5068,* 393–395.

[191] Gibbs-Davis, J. M.; Kruk, J. J.; Konek, C. T.; Scheidt, K. A.; Geiger, F. M. *J. Am. Chem. Soc.* **2008,** *130,* 15444–15447.

[192] Sulpizi, M.; Gaigeot, M.-P.; Sprik, M. *J. Chem. Theory Comput.* **2012,** *8,* 1037–1047.

[193] de Beer, A. G. F.; Campen, R. K.; Roke, S. *Phys. Rev. B* **2010,** *82,* 235431.

[194] Rehl, B.; Rashwan, M.; DeWalt-Kerian, E. L.; Jarisz, T.; Darlington, A.; Hore, D. K.; Gibbs, J. M. *J. Phys. Chem. C* **2019,** *123,* 10991–11000.

[195] García Rey, N.; Weißenborn, E.; Schulze-Zachau, F.; Gochev, G.; Braunschweig, B. *J. Phys. Chem. C* **2019,** *123,* 1279–1286.

[196] Ohno, P. E.; Wang, H.-f.; Geiger, F. M. *Nature Comm.* **2017,** *8,* 1032.

[197] Boamah, M. D.; Ohno, P. E.; Geiger, F. M.; Eisenthal, K. B. *J. Chem. Phys.* **2018,** *148,* 222808.

[198] Brady, P. V. *Geochim. Cosmochim. Acta* **1992,** *56,* 2941–2946.

[199] Darlington, A. M.; Gibbs-Davis, J. M. *J. Phys. Chem. C* **2015,** *119,* 16560–16567.

[200] Leung, K.; Nielsen, I. M. B.; Criscenti, L. J. *J. Am. Chem. Soc.* **2009,** *131,* 18358–18365.

[201] Light, T. S. *Anal. Chem.* **1984,** *56,* 1138–1142.

[202] Zhuravlev, L. T. *Coll. Surf. A: Phys. Eng. Asp.* **2000,** *173,* 1–38.

[203] Brown, M. A.; Goel, A.; Abbas, Z. *Angew. Chem. Int. Ed.* **55,** *2016,* 3790–3794.

[204] Nagata, Y.; Hasegawa, T.; Backus, E. H. G.; Usui, K.; Yoshimune, S.; Ohto, T.; Bonn, M. *Phys. Chem. Chem. Phys.* **2015,** *17,* 23559–23564.

[205] Paukshtis, E. A.; Yurchenko, E. N. *Russ. Chem. Rev.* **1983,** *52,* 242–258.

[206] Sauer, J.; Hill, J.-R. *Chem. Phys. Lett* **1994,** *218,* 333–337.

[207] Tossell, J. A.; Sahai, N. *Geochim. Cosmochim. Acta* **2000,** *64,* 4097–4113.

[208] Orazov, M.; Davis, M. E. *Chem. Sci.* **2016,** *7,* 2264–2274.

[209] Hensen, E. J. M.; Poduval, D. G.; Degirmenci, V.; Ligthart, D. A. J. M.; Chen, W.; Maugé, F.; Rigutto, M. S.; van Veen, J. A. R. *J. Phys. Chem. C* **2012,** *116,* 21416–21429.

[210] Ugazio, E.; Gastaldi, L.; Brunella, V.; Scalarone, D.; Jadhav, S. A.; Oliaro-Bosso, S.; Zonari, D.; Berlier, G.; Miletto, I.; Sapino, S. *Int. J. Pharm.* **2016,** *511,* 446–454.

[211] Brunella, V.; Jadhav, S. A.; Miletto, I.; Berlier, G.; Ugazio, E.; Sapino, S.; Scalarone, D. *React. Funct. Polym.* **2016,** *98,* 31–37.

[212] Wang, B.; Horton, J. H.; Oleschuk, R. D. *Can. J. Chem.* **2006,** *84,* 720–729.

[213] Sia, S. K.; Whitesides, G. M. *Electrophoresis* **2003,** *24,* 3563–3576.

[214] Patabadige, D. E.; Jia, S.; Sibbitts, J.; Sadeghi, J.; Sellens, K.; Culbertson, C. T. *Anal. Chem.* **2016,** *88,* 320–338.

[215] Sze, A.; Erickson, D.; Ren, L.; Li, D. *J. Colloid Interface Sci.* **2003,** *261,* 402–410.

[216] Ocvirk, G.; Munroe, M.; Tang, T.; Oleschuk, R.; Westra, K.; Harrison, D. J. *Electrophoresis* **2000,** *21,* 107–115.

[217] Bao, N.; Xu, J.-J.; Zhang, Q.; Hang, J.-L.; Chen, H.-Y. *J. Chromatogr. A* **2005,** *1099,* 203–206.

[218] Liu, Z.; Song, Y.; Li, D. *J. Colloid Interface Sci.* **2020,** *578,* 116–123.

[219] Efimenko, K.; Wallace, W. E.; Genzer, J. *J. Colloid Interface Sci.* **2002,** *254,* 306–315.

[220] Tandon, V.; Bhagavatula, S. K.; Nelson, W. C.; Kirby, B. J. *Electrophoresis* **2008,** *29,* 1092–1101.

[221] Ohno, P. E.; Chang, H.; Spencer, A. P.; Liu, Y.; Boamah, M. D.; Wang, H.-f.; Geiger, F. M. *J. Phys. Chem. Lett.* **2019,** *10,* 2328–2334.

[222] Dalstein, L.; Huang, J.-R.; Wen, Y.-C. *Opt. Lett.* **2020,** *45,* 3733-3736.

[223] Chang, H.; Ohno, P. E.; Liu, Y.; Lozier, E. H.; Dalchand, N.; Geiger, F. M. *J. Phys. Chem. B* **2020,** *124,* 641–649.

[224] Ren, X.; Bachman, M.; Sims, C.; Li, G.; Allbritton, N. *J. Chromatogr. B* **2001,** *762,* 117–125.

[225] Radüge, C.; Pflumio, V.; Shen, Y. *Chem. Phys. Lett.* **1997,** *274,* 140–144.

[226] Schultz, M. J.; Baldelli, S.; Schnitzer, C.; Simonelli, D. *J. Phys. Chem. B* **2002,** *106,* 5313–5324.

[227] Liu, D.; Ma, G.; Levering, L. M.; Allen, H. C. *J. Phys. Chem. B* **2004,** *108,* 2252–2260.

[228] Creux, P.; Lachaise, J.; Graciaa, A.; Beattie, J. K.; Djerdjev, A. M. *J. Phys. Chem. B* **2009,** *113,* 14146–14150.

[229] McCaffrey, D. L.; Nguyen, S. C.; Cox, S. J.; Weller, H.; Alivisatos, A. P.; Geissler, P. L.; Saykally, R. J. *PNAS* **2017,** *114,* 13369–13373.

[230] Vrbka, L.; Mucha, M.; Minofar, B.; Jungwirth, P.; Brown, E. C.; Tobias, D. J.

[231] Can, N.; Ömür, B. C.; Altındal, A. *Sens. Actuators, B* **2016,** *237,* 953–961.

[232] García-Zubiri, I. X.; González-Gaitano, G.; Isasi, J. R. *J. Colloid Interface Sci.* **2009,** *337,* 11–18.

[233] Apopei, D. F.; Dinu, M. V.; Trochimczuk, A. W.; Dragan, E. S. *Ind. Eng. Chem. Res.* **2012,** *51,* 10462–10471.

[234] Ma, E.; Ohno, P. E.; Kim, J.; Liu, Y.; Lozier, E. H.; Miller III, T. F.; Wang, H.-F.; Geiger, F. M. *J. Phys. Chem. Lett.* **2021,** *12,* 5649–5659.